From Knowledge to Wisdom

JEPE

ISSN 1934-8975 (Print)
ISSN 1934-8983 (Online)
DOI:10.17265/1934-8975

Journal of Energy and Power Engineering

Volume 9, Number 10, October 2015

David Publishing Company
www.davidpublisher.com

Journal of Energy and Power Engineering

Volume 9, Number 10, October 2015 (Serial Number 95)

David Publishing Company
www.davidpublisher.com

Publication Information:
Journal of Energy and Power Engineering is published monthly in hard copy (ISSN 1934-8975) and online (ISSN 1934-8983) by David Publishing Company located at 1840 Industrial Drive, Suite 160, Libertyville, IL 60048, USA.

Aims and Scope:
Journal of Energy and Power Engineering, a monthly professional academic journal, covers all sorts of researches on Thermal Science, Fluid Mechanics, Energy and Environment, Power System and Automation, Power Electronic, High Voltage and Pulse Power, Sustainable Energy as well as other energy issues.

Manuscripts and correspondence are invited for publication. You can submit your papers via Web Submission, or E-mail to energy@davidpublishing.com or info@davidpublishing.com. Submission guidelines and Web Submission system are available at www.davidpublisher.com.

Editorial Office:
1840 Industrial Drive, Suite 160, Libertyville, IL 60048, USA
E-mail: energy@davidpublishing.com; energy@davidpublishing.org; energy-power@hotmail.com; energy@davidpublishing.net.

Abstracted / Indexed in:
Database of EBSCO, Massachusetts, USA
Database of Cambridge Science Abstracts (CSA), USA
Chinese Database of CEPS, American Federal Computer Library Center (OCLC), USA
Ulrich's Periodicals Directory
Summon Serials Solutions
Chinese Scientific Journals Database, VIP Corporation, Chongqing, China
Chemical Abstracts Service (CAS)
ProQuest
CNKI
Google Scholar

Subscription Information:
Price:
Print $800 (per year)
Online $600 (per year)
Print and Online $880 (per year)

David Publishing Company
Tel: 1-323-984-7526, 001-323-410-1082; Fax: 1-323-984-7374; 323-908-0457
E-mail: order@davidpublishing.com
Digital Cooperative Company: www.bookan.com.cn

David Publishing Company
www.davidpublisher.com

Journal of Energy and Power Engineering

Volume 9, Number 10, October 2015 (Serial Number 95)

Contents

Journal of Energy and Power Engineering 9 (2015) 831-843
doi: 10.17265/1934-8975/2015.010.001

Combustion of Renewable Biogas Fuels

Chaouki Ghenai[1] and Isam Janajreh[2]

1. Sustainable and Renewable Energy Department, College of Engineering, University of Sharjah, Sharjah 27272, United Arab Emirates

2. Mechanical Engineering Program, MASDAR Institute of Science and Technology, Abu Dhabi 54224, United Arab Emirates

Received: July 07, 2015 / Accepted: August 05, 2015 / Published: October 31, 2015.

Abstract: Biogas fuel is a sustainable and renewable fuel produced from anaerobic digestion of organic matter. The biogas fuel is a flammable mixture of methane and carbon dioxide with low to medium calorific values. Biogas is an alternative to conventional fossil fuels and can be used for heating, transportation and power generation. CFD (computational fluid dynamic) analysis of the combustion performance and emissions of biogas fuel in gas turbine engines is presented in this study. The main objective of this study is to understand the impact of the variability in the biogas fuel compositions and lower heating values on the combustion process. Natural gas, biogas from anaerobic digester, landfill biogas, and natural gas/biogas mixture fuels combustion were investigated in this study. The CFD results show lower peak flame temperature and CO mole fractions inside the combustor and lower NO_x emissions at the combustor exit for the biogas compared to natural gas fuel. The peak flame temperature decreases by 37% for the biogas landfill (CO_2/CH_4 = 0.89) and by 22% for the biogas anaerobic digester (CO_2/CH_4 = 0.54) compared to natural gas fuel combustion. The peak CO mole fraction inside the combustor decreases from 9.8×10^{-2} for natural gas fuel to 2.22×10^{-4} for biogas anaerobic digester and 1.32×10^{-7} for biogas landfill. The average NO_x mole fraction at the combustor exit decreases from 1.13×10^{-5} for natural gas fuel to 0.40×10^{-6} for biogas anaerobic digester and 1.06×10^{-10} for biogas landfill. The presence of non-combustible constituents in the biogas reduces the temperature of the flame and consequently the NO_x emissions.

Key words: Anaerobic digestion, biogas, non-premixed combustion, NO_x emissions, CFD.

1. Introduction

Most of the present energy demands (80%-85%) are provided through the combustion of fossil fuels (natural gas, oil and coal). The reliance on fossil fuels will diminish in the coming decades due to the new emissions regulations (reduction of carbon dioxides CO_2, other greenhouses gases such as NO_x and SO_x and particulate matter), depletion of fossil fuels (reduction of oil, natural gas and coal reserves), and the need of more renewable and sustainable energy systems [1]. Renewable power systems using renewable resources such as solar, wind, hydro, ocean, geothermal and biomass natural resources are alternatives to conventional power generation using coal, natural gas and oil fossil fuels [1]. Sustainable and renewable biofuels such as syngas, biogas, biodiesel, bioethanol and bio-oil are alternatives to conventional fuels that can be used for transportation, heating and power generation. Biofuels produced from biomass (sustainable energy sources: wood, plants, vegetable oils, green waste, animal waste and sludge) through thermal and biochemical conversion processes are good fuel candidates for the replacement of fossil fuels usage. The biofuels are more sustainable fuels produced from local and renewable resources and offer lower emissions compared to fossil fuels combustion.

Natural gas is used as the primary fuel in gas turbine engine combustors for power generation. The development and use of new renewable and alternative gas fuels such as biogas derived from anaerobic digester and landfills and syngas derived from biomass, coal and solid waste gasification processes present certain challenges that must be addressed. The alternative fuels such as syngas and biogas have different chemical compositions and heating values

Corresponding author: Chaouki Ghenai, assistant professor, research fields: renewable energy, energy efficiency, alternative fuels, combustion and sustainability. E-mail: cghenai@sharjah.ac.ae.

compared to natural gas fuels. The lower heating values (MJ/kg) of alternatives fuels such as syngas and biogas are much lower than heating value of natural gas. For the same combustor power, the fuel mass flow for syngas and biogas should be much greater than for natural gas, due to the lower heating values. Lean turbulent premixed combustions are usually used for gas turbine engines to control the NO_x emissions [2]. The combustion systems using lean combustion technologies cannot be used for syngas fuels with high hydrogen (60%-70%) content due to the potential for flashback of the flame into the fuel injection systems. Non-premixed combustors are more appropriate for synags fuels with high hydrogen contents [2]. The flame temperature and NO_x emissions can be controlled by diluting the syngas fuels with inert gas. Natural gas is made mainly of methane (CH_4), syngas fuel contains methane (CH_4), carbon dioxide (CO_2), carbon monoxide (CO), hydrogen (H_2), nitrogen (N_2) and water (H_2O), and biogas contains mainly methane (CH_4) and carbon dioxide (CO_2). The changes in the fuel compositions and lower heating values for alternative gas fuels (syngas and biogas) affect the combustion process, the efficiency of the combustion system and the gas emissions at the exit from the combustor [3]. The new gas turbine combustors for renewable and biofuels should be able to burn a wide variety of gases (syngas, biogas and other alternative gas fuels) with low, medium and high heating values. The new combustors should be able to handle syngas fuels with high hydrogen content (high flame speed and flame stability problems). The new alternative fuels (biogas and syngas) must be burned efficiently in the combustors. The NO_x and CO_2 emissions from the combustion of syngas and biogas fuels should be comparable or better than those obtained with natural gas fuels. Better understanding of the physical and chemical processes of syngas and biogas combustion is needed in order to meet these challenges and help the development and use of biofuels in existing or new combustion systems. Information such as flame shape, flame speed, turbulent flow/flame interactions, gas temperatures and pollutant emissions (NO_x and CO_2) for a range of alternative fuels compositions and heating values is needed for the design of gas turbine combustors.

The syngas produced from renewable energy sources will help to reduce emissions from combustion systems and increase the energy security (offsets non-renewable resources—coal, oil, natural gas). Brdar and Jones [4] investigated the integration of heavy-duty gas turbine technology with synthetic fuel gas processes. They summarized in this study the experience gained from several syngas projects and lessons learned with respect to cost reductions and improving the operational reliability of gas turbine. They concluded that, further improvements are needed for syngas use in gas turbine engines especially with respect to system performance and plant design. The results of the combustion of low calorific syngas fuels derived from gasification of waste biomass were presented by Kwiatkowski, et al. [5]. Computational fluid dynamics of the combustion of two different gases derived from gasification of waste wood chips and turkeys feathers was presented in this paper. The result shows that, low calorific syngas from waste biomass including gas derived from the gasification of feathers can be valuable fuel for direct combustion on industrial scale. The impact of firing syngas in gas turbine engines was investigated experimentally by Oluyede [6]. The results of the experimental investigation show that, volume fraction of hydrogen content in syngas fuel results in higher flame temperature that significantly impacts the life of hot sections of the combustor. Giles, et al. [7], Ghenai [3] and Zbeeb and Ghenai [8] performed numerical investigations on the effects of syngas compositions and diluents on the flame structure and emissions for non-premixed combustion. For premixed combustion, lean premixed combustion of hydrogen-syngas/methane fuel mixtures was investigated experimentally by Alavandi and Agarwal [9]

and Schefer [10]. In their studies, they investigated the effect of hydrogen content in syngas fuels on the biofuels combustion process. Rahm, et al. [11] addressed the challenges of fuel diversity use and the corresponding environmental and engine performance impacts. They reviewed the combustion design flexibility for the use of a different gas and liquid fuels including emerging synthetic fuels. The synthetic gases included low heating value process gas, syngas, ultra-high hydrogen or higher heating values fuels.

In anaerobic digester process, micro-organisms break down biodegradable material in the absence of oxygen to produce biogas and digester by products as shown in Fig. 1. The biogas feed stocks or digester inputs include organic matter from plants and animals, waste water, and food processing waste. The biogas produced can be burned and used for different applications (Fig. 1). Biogas can be used to offset non-renewable resources; biogas is produced using renewable energy resources; and offer environmental benefits by reducing the emissions by preventing CH_4 release to the atmosphere and reducing landfill wastes and odors. Razbani, et al. [12] performed a literature review on biogas use in internal combustion engines. He reviewed the challenges such as lower flame speed compared to natural gas, biogas impurities, and combustion characteristics of biogas fuel in reciprocating engines. Solutions such as advanced spark timing, increasing compression ratio, changing bearing and piston materials were presented. Laminar burning velocities of biogas-air mixtures in premixed combustion have been studied to elucidate the fundamental flame propagation characteristic of biogas as a new alternative and renewable fuel [13] in spark ignition engine. The results show that, the laminar burning velocities of biogas-air mixtures were lower than those in methane-air mixtures at the same equivalence ratio because biogas contains carbon dioxide and nitrogen which are flame inhibitors. Barik, et al. [14] reviewed the current status and perspectives of biogas production, including the storage methods and its engine application. The study concluded the potential of biogas production from various organic biomass wastes. Attention was also focused for making biogas as a transport vehicle and stationary engine fuel by storing it in cylinders and reinforced plastic bags. Colorado, et al. [15] investigated the performance of flameless combustion using biogas and natural gas fuels. The results show minor reduction of the efficiency of the furnace and lower temperatures for the biogas fuels.

This study focuses on the combustion performance and emissions of biogas fuels. The design of new combustion systems using sustainable and alternative fuels such as biogas fuel can take advantage of computational fluid dynamics analysis to optimize the efficiency of the combustion process and to reduce the pollutants emission. The principal objective of this study is to analyze the fundamental impacts of firing biogas in gas turbine combustor and predict the changes in the firing temperature and emissions with respect to natural gas combustion.

2. Governing Equations—Natural Gas and Biogas Combustion Modeling

The equations used for natural gas, biogas, and natural gas/biogas mixture fuels combustion modeling [3] are based on the equations of conservation of mass, momentum and energy, the equations of the turbulent kinetic energy k and the dissipation rate of the turbulent kinetic energy the ε standard k-ε turbulence model), the mixture fraction equation (mixture fraction/PDF (probability density function)) model for non-premixed combustion modeling), and the equation to simulate the radiation from the flame (P-1 radiation model). For steady turbulent non premixed combustion [3], the time averaged gas phase equations are summarized in Table 1. It is noted that, ρ is the density, u is the velocity, P is the pressure, τ is the shear stress, k is the turbulent kinetic energy, ε is the dissipation of the turbulent kinetic energy and μ is the dynamic viscosity. For the turbulent kinetic energy

and dissipation of the kinetic energy equations, σ_k = 1, G_k is the production of the turbulent kinetic energy and $C_{\varepsilon 1}$ = 1.44, $C_{\varepsilon 2}$ = 1.92 and σ_ε = 1.3. For the mixture fraction equation and non-premixed (diffusion flame) combustion, the PDF/mixture fraction model is used in this study. First, the equation for the mixture fraction f is solved, and individual component concentrations are derived from the predicted mixture

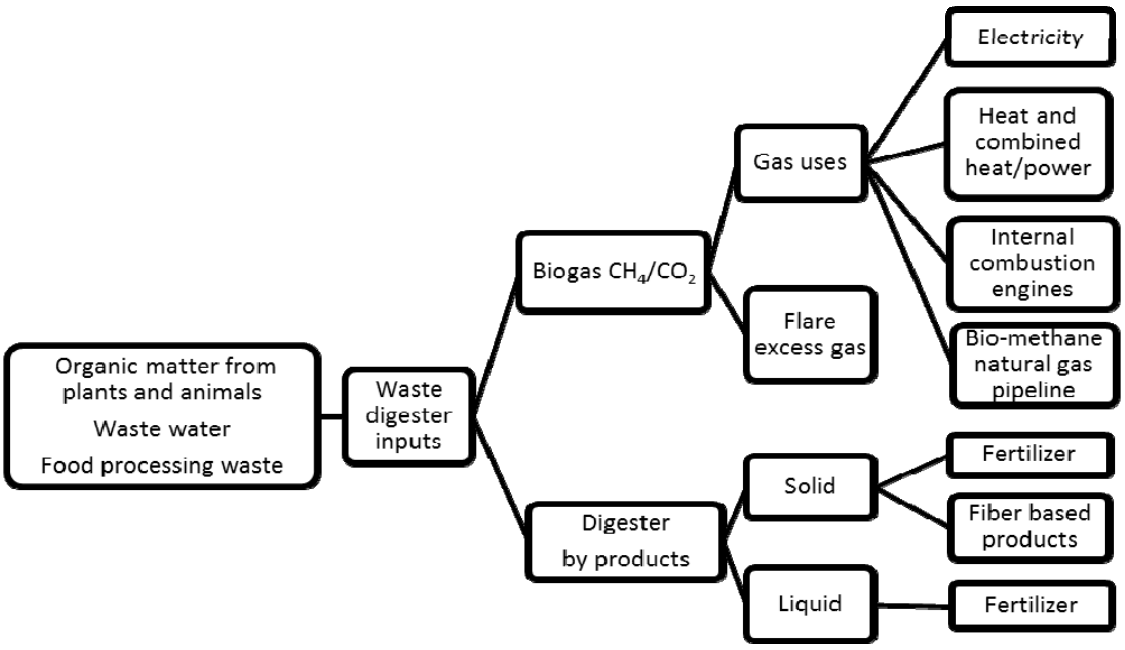

Fig. 1 Biogas production and utilization.

Table 1 Governing equations.

	Equations
Continuity	$\frac{\partial \overline{\rho u_i}}{\partial x_i} = 0$
Momentum	$\frac{\partial \left(\overline{\rho u_i u_j}\right)}{\partial x_j} = -\frac{\partial \overline{P}}{\partial x_i} + \frac{\partial \left(\overline{t_{ij}} + \overline{\tau_{ij}}\right)}{\partial x_j}$
Turbulent kinetic energy	$\frac{\partial \left(\overline{\rho k u_j}\right)}{\partial x_j} = \frac{\partial \left[\left(\mu + \frac{\mu_t}{\sigma_k}\right)\frac{\partial \overline{k}}{\partial x_j}\right]}{\partial x_j} + G_k - \overline{\rho \varepsilon}$
Dissipation of the kinetic energy	$\frac{\partial \left(\overline{\rho \varepsilon u_j}\right)}{\partial x_j} = C_{\varepsilon 1}\frac{\overline{\varepsilon}}{k}G_k + \frac{\partial \left[\left(\mu + \frac{\mu_t}{\sigma_\varepsilon}\right)\frac{\partial \overline{\varepsilon}}{\partial x_j}\right]}{\partial x_j} - C_{\varepsilon 2}\overline{\rho}\frac{\overline{\varepsilon^2}}{k}$
Mixture fraction f	$\frac{\partial \left(\overline{\rho f u_j}\right)}{\partial x_j} = \frac{\partial \left[\left(\frac{\mu_t}{\sigma_t}\right)\frac{\partial \overline{f}}{\partial x_j}\right]}{\partial x_j} + S_m$
Energy	$\frac{\partial \left(\overline{(\rho E + p)uj}\right)}{\partial x_j} = \frac{\partial \left[\left(k_{eff}\right)\frac{\partial \overline{T}}{\partial x_j} - \sum_j h_j J_j + \left(\overline{\tau}_{eff} u_j\right)\right]}{\partial x_j} + S_h$
Radiation	$q_r = -\frac{1}{3(a+\sigma_S) - C\sigma_S}\nabla G$

fraction distribution [3]. The mixture fraction f is given by $f = (Z_k - Z_{k,O})/(Z_{k,F} - Z_{k,O})$, where Z_k is the element mass fraction of element k. Subscripts F and O denote fuel and oxidizer inlet stream values, respectively. The chemistry is assumed to be fast enough to achieve equilibrium. The equilibrium chemistry PDF model was used and 13 species (C, CH_4, CO, CO_2, H, H_2, H_2O, N_2, NO, O, O_2, OH, HO_2) were selected for the combustion modeling. In the energy equation (Table 1), E is the total energy ($E = h - p/\rho + v^2/2$, where h is the sensible enthalpy), k_{eff} is the effective conductivity ($k + k_t$: laminar and turbulent thermal conductivity), J_j is the diffusion flux of species j, and S_h is the term source that includes the heat of chemical reaction, radiation and any other volumetric heat sources. The P-1 radiation model was used in this study to simulate the radiation from the flame [3]. This model is based on the expansion of the radiation intensity into an orthogonal series of spherical harmonics (Cheng [16] and Siegel and Howell [17]). The P-1 radiation model is the simplest case of the P-N model [3]. If only four terms in the series are used, the equation q_r for the radiation flux is obtained (Table 1), where, a is the absorption coefficient, σ_S is the scattering coefficient, G is the incident radiation and C is the linear-anisotropic phase function coefficient (Cheng [16] and Siegel and Howell [17]).

For NO_x modeling, the nitrogen oxides concentrations emitted from combustion systems are generally low, the NO_x chemistry has negligible influence on the predicted temperature, velocity field, and species concentrations. First, the main combustion calculations were performed then the NO_x emissions were calculated using the NO_x model (post-processing calculations). The reacting flows are simulated without NO_x emissions first until the convergence of the main combustion calculation was obtained, then the desired NO_x models (thermal and prompt NO_x) were enabled to predict the NO_x emissions.

For the numerical method, the finite volume and the first order upwind methods are used in this study to solve the governing equations. The solution procedure for mixture-fraction system is to complete first the calculation of the PDF look-up tables, start the reacting flow simulation to determine the flow files and predict the spatial distribution of the mixture fraction, continue the reacting flow simulation until a convergence solution was achieved, and determine the corresponding values of the temperature and individual chemical species mass fractions from the look-up tables. The convergence criteria for the continuity, momentum, turbulent kinetic energy, dissipation rate of the turbulent kinetic energy, and the mixture fraction were set to 10^{-3}. For the energy and the radiation equations, the convergence criteria were set to 10^{-6}.

3. Combustor Geometry Model and Composition and Lower Heating Values of Fuels

Fig. 2 shows the gas turbine can combustor geometry model used for this study. The combustor is similar to the one used by Ghenai [3] for the simulation of syngas fuels. The dimension of the can combustor is 590 mm in the z direction (longitudinal direction), 250 mm in the y direction and 230 mm in the x direction [3]. The primary air injected inside the can combustor is guided by air vanes to give swirling (Fig. 2). The primary air is injected from a an injection diameter of 85 mm with a velocity of 10 m/s, a temperature of 300 K (or 27 °C), turbulence intensity of 10%, and with zero mixture fraction (f = 0). The natural gas and biogas fuels are injected through six fuel injectors in the swirling primary air flow as shown in Fig. 2. It is noted that, the fuel mass flow rate (Table 2) was varied to keep the same power or rate of heat flow (watts or J/s) for the five fuels tested in this study. The fuel is injected through an injection diameter of 4.2 mm with a temperature of 300 K, a turbulence intensity of 10%, and a mixture fraction

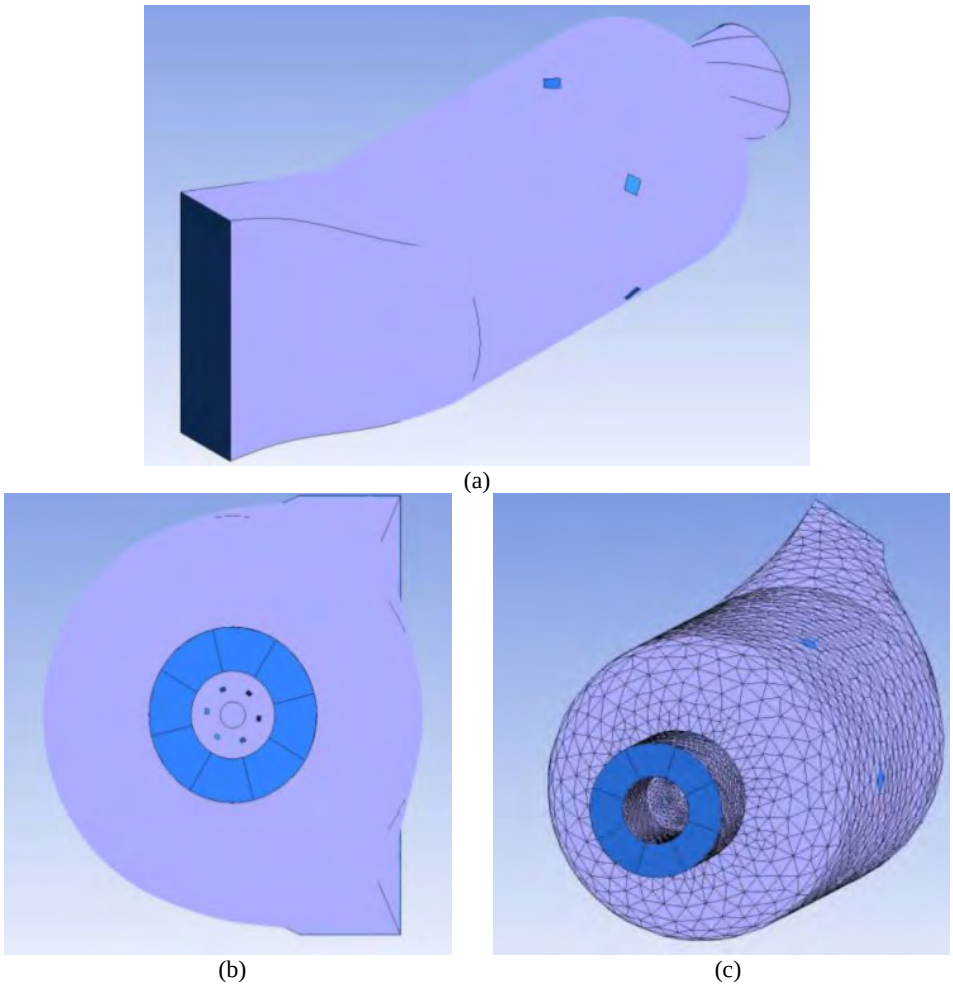

(a) (b) (c)

Fig. 2 Swirl can combustor geometry and mesh.

Table 2 Fuel composition—natural gas and low and high grade biogas.

	NG	Mixture 50% NG 50% BGAD	Mixture 50% NG 50% BGLF	Biogas anaerobic digester BGAD	Biogas landfill BGLF
CH_4 (%)	95	80	70	65	45
CO_2 (%)	0	17.5	20	35	40
N_2 (%)	2	1	8.5	0	15
C_2H_6 (%)	3	1.5	1.5	0	0
LHV (MJ/kg)	50	35	31	20	12.3
Fuel mass flow rate (kg/s)	1.0×10^{-3}	1.4×10^{-3}	1.6×10^{-3}	2.5×10^{-3}	4.06×10^{-3}
Power (kW)	50	50	50	50	50

NG: natural gas; BGAD: biogas anaerobic digester; BGAD: biogas landfill; LHV: lower heating values.

f = 1. To control the flame temperature and NO_x emissions, a secondary air or dilution air is injected at 0.1 m from the fuel injector. The secondary air is injected in the combustion chamber though six side air inlets each with a diameter of 16 mm (Fig. 2) with an injection velocity of 6 m/s, a temperature of 300 K, a turbulence intensity of 10%, and a mixture fraction f = 0. The can combustor outlet has a rectangular shape (Fig. 2) with an area of 0.0150 m^2 [3]. The mesh generated for the can combustor (Fig. 2) consists of 106,651 cells or elements (74,189 tetrahedra, 30,489 wedges and 1,989 pyramids).

Table 2 shows the composition and lower heating values of the five fuels selected in this study for the CFD analysis. The range of the constituents volume fractions for the selected fuels are: methane (CH_4) = 45%-95%, carbon dioxide (CO_2) = 0-40%, and nitrogen (N_2) = 0-15%. The carbon dioxide to methane ratio for the five gases is between 0 and 0.89 (zero for the natural gas and 0.89 for the landfill biogas). Table 2 shows also that, the lower heating values for the biogas fuels are smaller compared to the lower heating value of natural gas. The biogas landfill is the low grade bio gas fuel with only 12.3 MJ/kg heating value compared to 50 MJ/kg for natural gas.

4. Results and Discussion

The results of the combustion performance and emissions of conventional fuel (natural gas) and alternative fuel (biogas) in gas turbine can combustor are presented in this paper.

Figs. 3 and 4 show the contours of the predicted gas temperature in the x-y and z-x planes for the steady state combustion of natural gas, biogas, and natural gas/biogas mixtures in gas turbine can combustor. The results show a maximum gas temperature for methane fuel combustion of 2,110 K. The maximum predicted temperature for the methane fuel combustion compares well with the theoretical adiabatic flame temperature (2,200 K). The static temperature contours show a peak gas temperature in the primary reaction zone. The fuel injected from the six injectors is mixed first with the swirling air before burning in the primary reaction zone. The gas temperature decreases after the primary reaction zone due to the dilution of the flame with secondary air flow. The flame structure and the temperature in the reaction zone are affected by the turbulent air flow (flame/flow interaction). Highly turbulent air flow and the air flow turbulent characteristics (characteristic length and time scales, velocity fluctuations, and re-circulations zones) will affect the turbulent burning velocity of the flame, the flame structure, and the burning rates (rate of conversion of reactants to products in kg/s). The velocity vectors in the z-x plane and the recirculation zones in the primary reaction zone are shown in Fig. 5. The primary air is accelerated in the z direction from an initial velocity of 10-20 m/s at the entrance of the combustors due to the presence of swirls vanes [3]. The re-circulation regions produced near the fuel injection region help to mix the fuel and air. In the primary reaction zone, a good air fuel mixing is obtained (Fig. 5). The gas fuel is burned efficiently and the gas emissions at the exit from the can combustor are reduced. The contours (in the x-y plane) of the velocity swirling strength are shown in Fig. 6. The contours in Fig. 6 show recirculation zones near the fuel injection regions (near the primary reaction zone) with strong swirling strength. Higher combustion efficiency is obtained in the regions with strong swirling strength. The velocity swirling strength decreases downstream with the increase of the axial distance *Z*.

The effects of fuel compositions and lower heating values on static temperatures contours and the static temperature profiles inside the can combustors are shown in Figs. 3, 4 and 7. The results show that, the gas temperature inside the can combustor decreases by reducing the amount of methane and increasing the concentrations of carbon dioxide. The dilution of hydrocarbon fuel (CH_4) with carbon dioxide (CO_2) and nitrogen (N_2) reduce the flame temperature. It is noted that, the nitrogen and carbon dioxide ($N_2 + CO_2$) in the fuel is 2% for natural gas, 35% for biogas produced from anaerobic digester and 55% for biogas from landfill). The inert gas such as CO_2 and nitrogen absorb the heat from the combustion process and act as flame inhibitors. The presence of carbon dioxide and nitrogen reduces the burning velocity [12] of the flame and the burning rate (rate of conversion of reactants to combustion products).

Biogas air mixtures combustion produced lower gas temperature inside the combustor compared to natural gas fuel. The gas temperature for biogas fuel

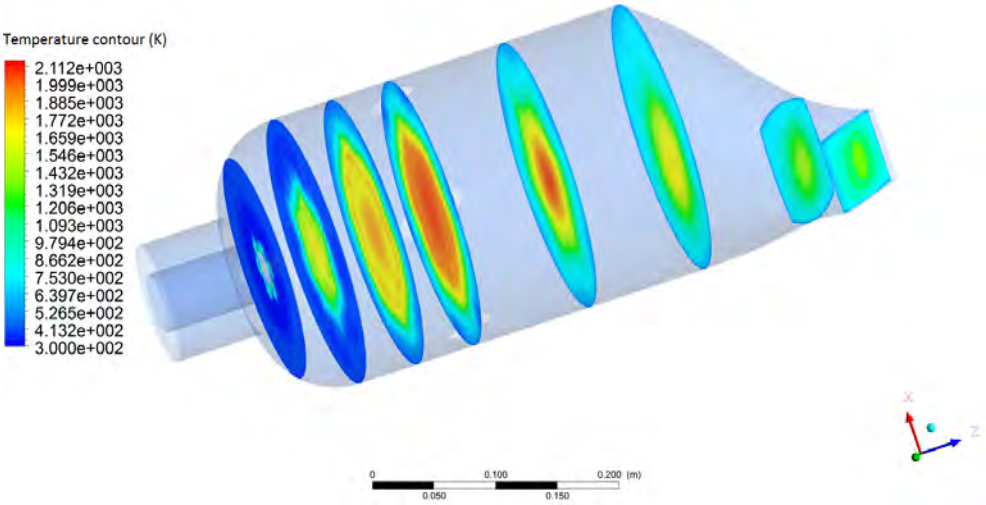

(a) NG

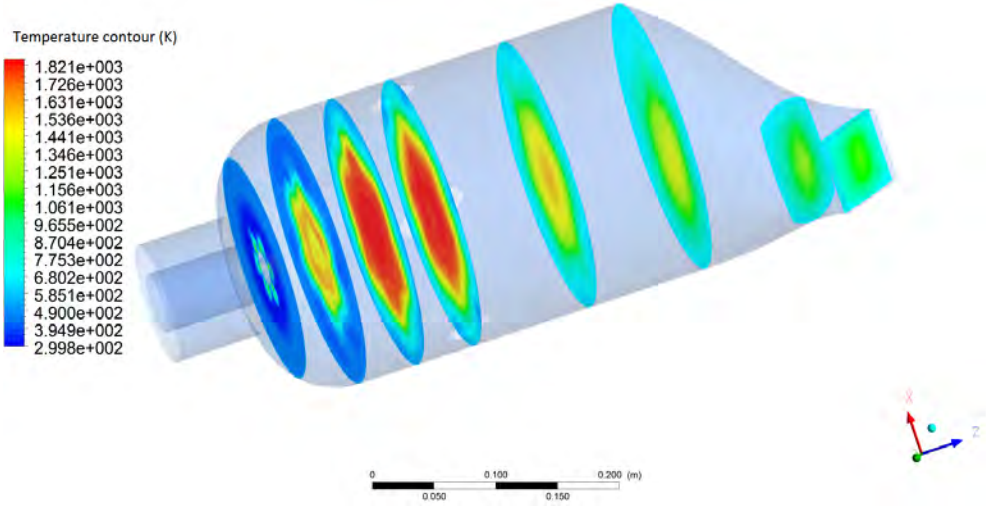

(b) BGAD

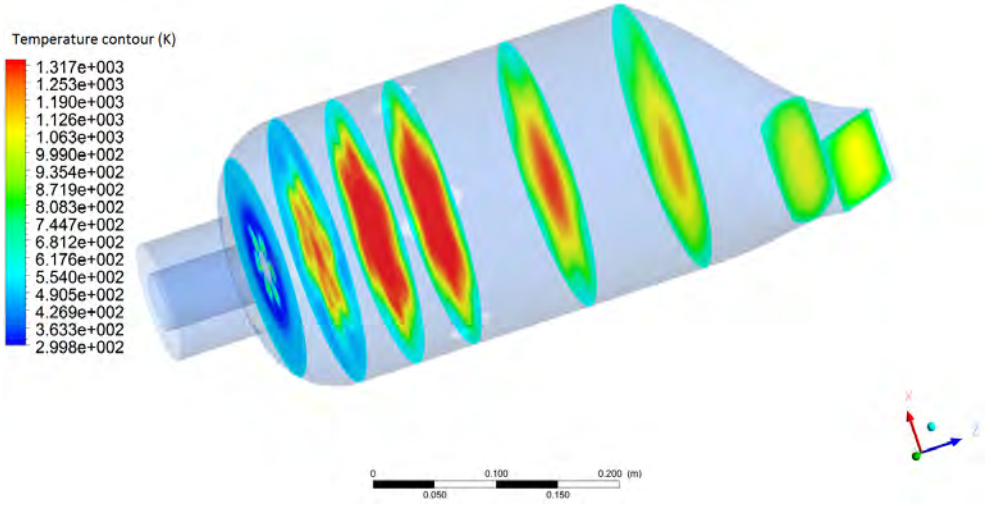

(c) BGLF

Fig. 3 Static temperature contours in the x-y plane: (a) NG, (b) BGAD and (c) BGLF.

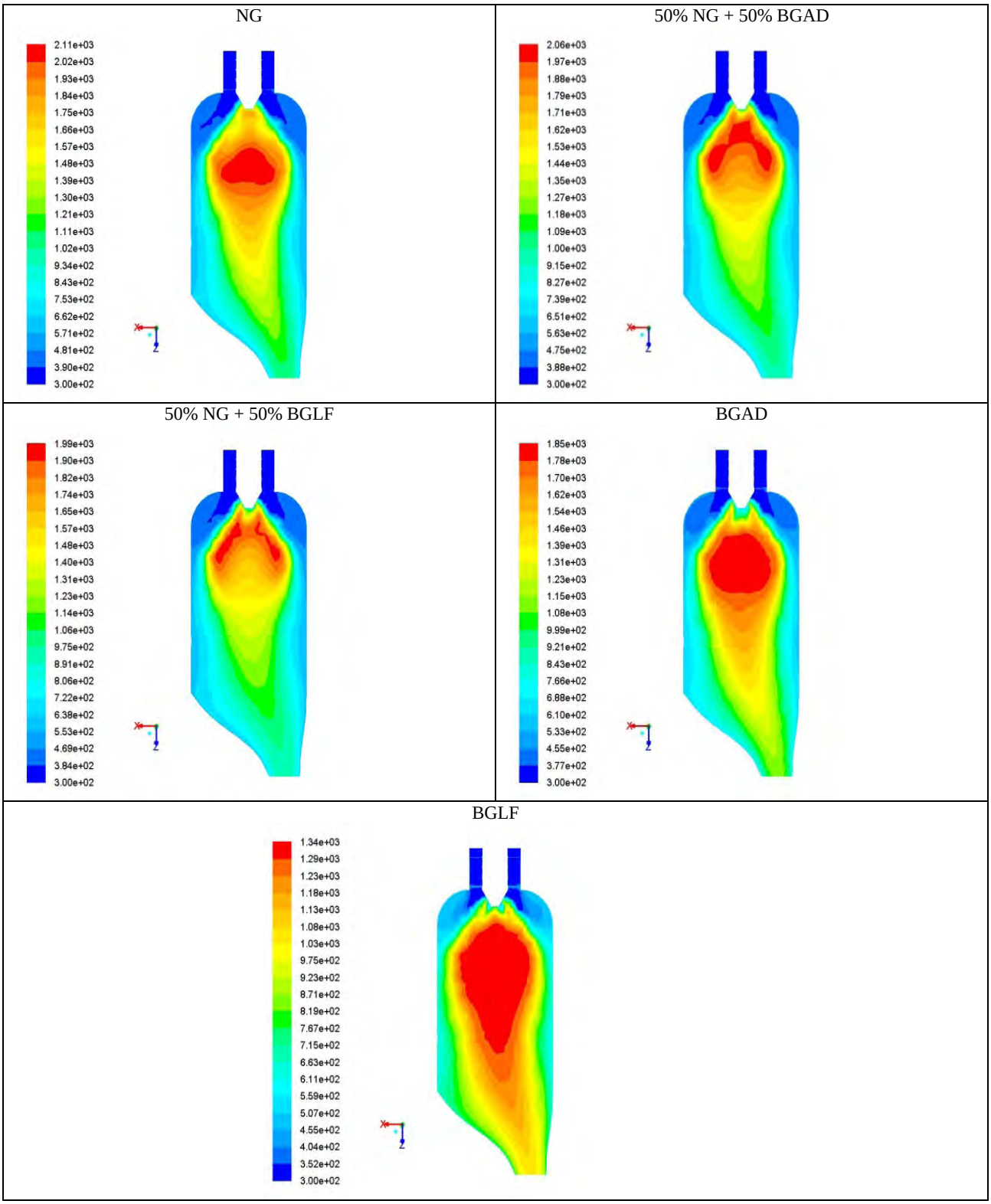

Fig. 4 Contours of static temperature (K) in the z-x plane.

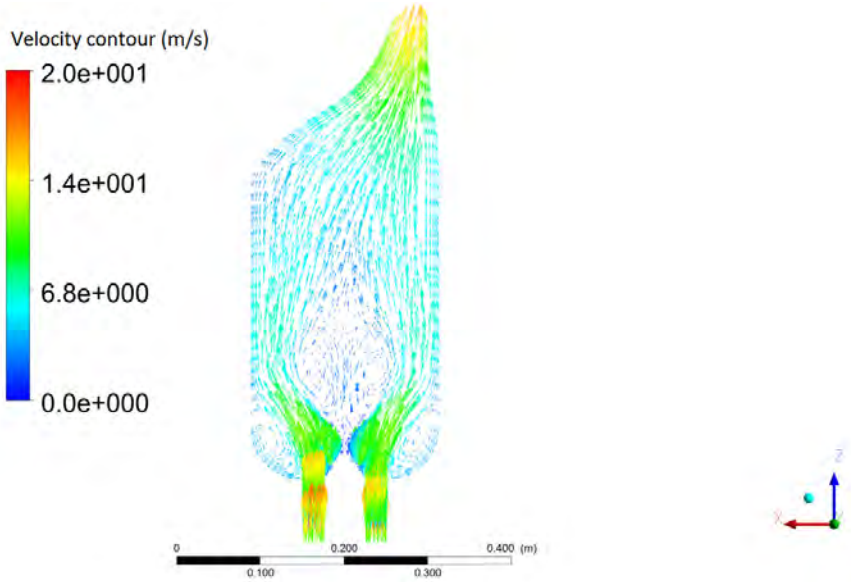

Fig. 5 Velocity vectors in the z-x plane.

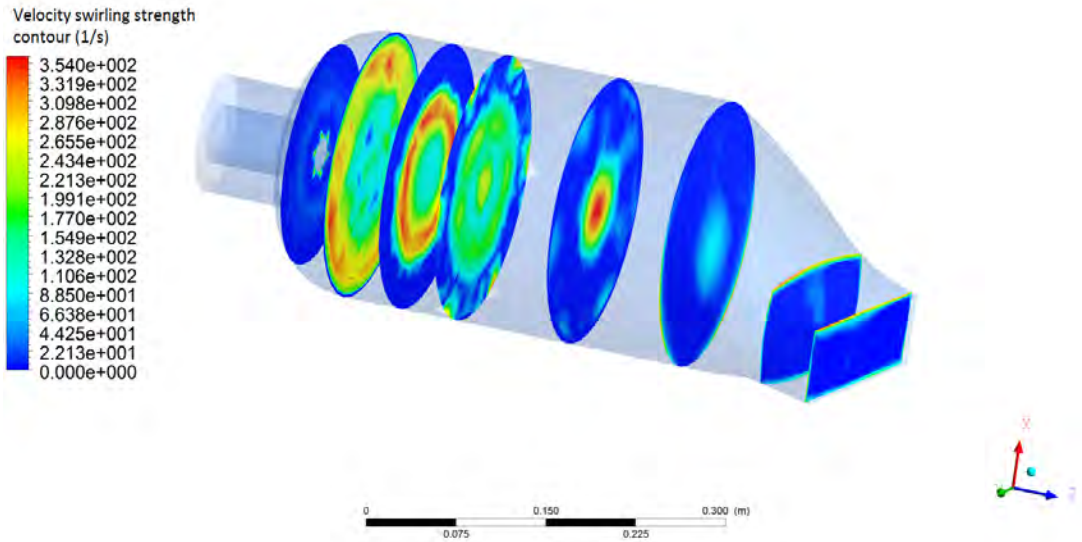

Fig. 6 Velocity swirling strength in the x-y plane.

combustion depends on the carbon dioxide to methane ratio (CO_2/CH_4) as shown in Table 3. The peak gas temperature decreases as the CO_2/CH_4 ratio increases. The peak gas temperature decreases by 37% and 22%, respectively for the biogas-landfill (CO_2/CH_4 = 0.89) and biogas anaerobic digester (CO_2/CH_4 = 0.54) compared to natural gas fuel.

The NO_x emissions from natural and biogas fuels combustion were also calculated in this study. The centerline NO_x (ppm) emissions inside the can combustor are shown in Fig. 8. The results show that, the NO_x emissions inside the combustor decreases when the baseline fuel (natural gas) is replaced with biogas fuel with lower heating value. The thermal NO_x emission is function of the gas temperature. High gas temperature inside the can combustor will produce high NO_x (mainly NO) emissions. The presence of non-combustible constituents in the biogas such as carbon dioxides and nitrogen reduces the temperature of the flame and consequently the NO mass fractions. This reduction is proportional to the amount of inert constituents in biogas fuel.

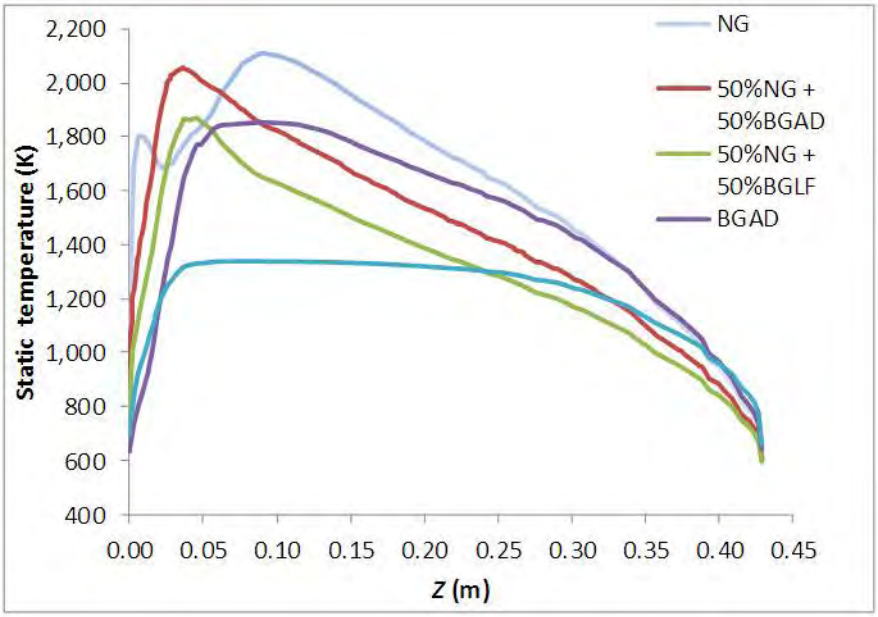

Fig. 7 Centerline (x = 0, y = 0) static temperature profiles.

Table 3 Effect of carbon dioxide to methane ratio on static temperature, CO and CO_2 mole fractions inside the combustor.

	NG	Mixture 50% NG 50% BGAD	Mixture 50% NG 50% BGLF	BGAD	BGLF
CO_2/CH_4	0	0.22	0.29	0.54	0.89
Peak flame temperature (K)	2,109	2,054	1,866	1,852	1,337
Peak CO mole fractions	9.85×10^{-2}	3.92×10^{-2}	4.38×10^{-3}	2.22×10^{-4}	1.32×10^{-7}
Peak CO_2 mole fractions	9.38×10^{-2}	17.5×10^{-2}	20×10^{-2}	35×10^{-2}	40×10^{-2}

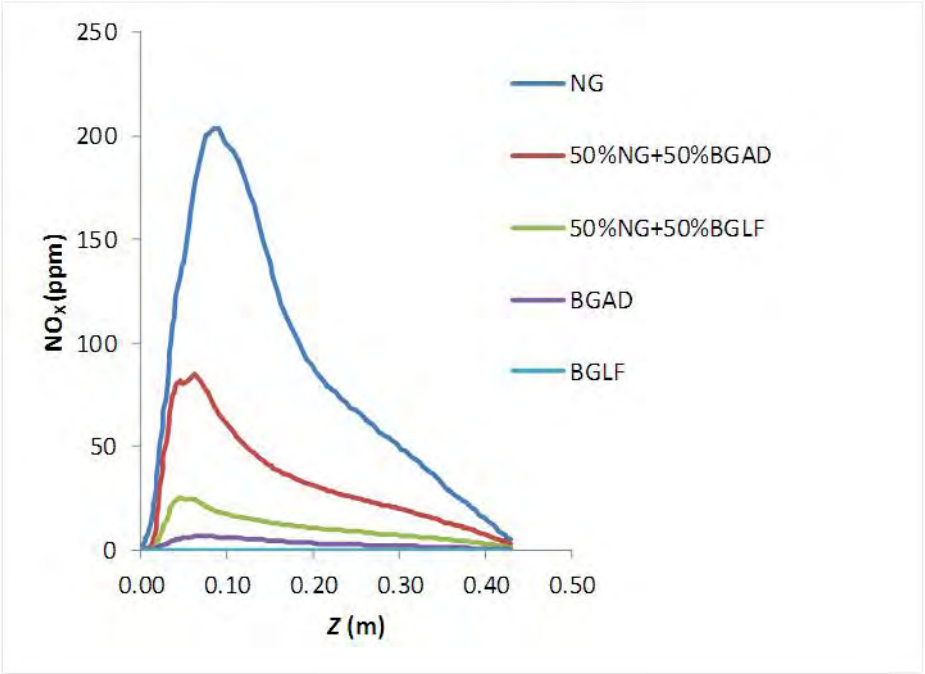

Fig. 8 Centerline NO_x emissions profiles.

Table 4 Effect of carbon dioxide to methane ratio on the temperature and species mole fractions at the exit of the combustor.

	NG	Mixture 50% NG 50% BGAD	Mixture 50% NG 50% BGLF	BGAD	BGLF
CO_2/CH_4	0	0.22	0.29	0.54	0.89
Exit average gas Temperature (K)	869	818	786	889	879
Exit average CO_2 mole fractions	2.2×10^{-2}	2.41×10^{-2}	2.37×10^{-2}	3.51×10^{-2}	4.2×10^{-2}
Exit average NO_x mole fractions	1.13×10^{-5}	5.68×10^{-6}	2.33×10^{-6}	0.40×10^{-6}	1.06×10^{-10}

The effect of biogas CO_2/CH_4 ratio on the peak flame temperature, CO and CO_2 emissions inside the can combustor (3D geometry) is summarized in Table 3. An increase of the CO_2/CH_4 ratio for the biogas fuel result in a decrease of the peak flame temperature and CO mole fractions and an increase of the CO_2 mole fractions inside the can combustor. The effect of the biogas CO_2/CH_4 ratio on the combustion and emissions characteristics at the exit of the can combustor was also determined in this study. The average flame temperature, CO_2 mole fractions and NO_x mole fractions at the exit of the combustor are presented in Table 4. The NO_x emissions at the exit of the combustor decrease with the increase of the biogas CO_2/CH_4 ratio but the emissions of CO_2 at the exit of the combustor increase with an increase of CO_2 fractions in the biogas fuels (higher CO_2 input).

5. Conclusions

Three dimensional CFD analyses of natural gas, biogas anaerobic digester, biogas landfill and natural gas/biogas fuels combustion in gas turbine can combustor are presented in this study. The effect of the biogas fuel composition, and fuel heating values on flame shape, flame temperature, carbon dioxide (CO_2), carbon monoxide (CO) and nitrogen oxides (NO_x) emissions was determined in this study. The results show lower flame temperatures for the biogas and biogas/natural gas mixtures compared to the adiabatic flame temperature of natural gas. The flame temperature for biogas fuel combustion depends on the carbon dioxide to methane ratio (CO_2/CH_4). The peak flame temperature decreases by 37% and 22%, respectively for the biogas-landfill (CO_2/CH_4 = 0.89) and biogas anaerobic digester (CO_2/CH_4 = 0.54) compared to natural gas fuel. The presence of inert gas (CO_2) with methane cools down the reaction by absorbing energy from the combustion and modifies the reaction zone by reducing the burning velocity of the flame and the burning rate. The reaction zone is elongated when large amount of CO_2 is added to methane. The emissions from biogas combustion vary with the composition of biogas. The higher CO_2 percentage in the biogas fuel, the lower is the NO_x emissions and the higher is the CO_2 emissions at the exit of the combustor. The CO emissions also decrease by increasing the CO_2/CH_4 ratio of the biogas fuel.

References

[1] Ghenai, C. 2014. “Energy-Water-Carbon Interconnection: Challenges and Sustainable Solution Methods and Strategies.” *International Journal of Thermal & Environmental Engineering* 7 (2): 57-64.

[2] Lieuwen, T., McDonell, V., Santavicca, D., and Sattelmayer, T. 2008. “Burner Development and Operability Issues Associated with Steady Flowing Syngas Fired Combustors.” *Combustion Science and Technology* 180 (6): 1167-90.

[3] Ghenai, C. 2010. “Combustion of Syngas Fuel in Gas Turbine Can Combustor.” *Advances in Mechanical Engineering* 2 (January): 13.

[4] Brdar, R. D., and Jones, R. M. 2000. “GE IGCC Technology and Experience with Advanced Gas Turbines.” GE Power Systems, GER-4207.

[5] Kwiatkowki, K., Dudynski, M., and Bajer, K. 2013. “Combustion of Low Waste Biomass Syngas.” *Flow Turbulence Combust* 91 (4): 749-72.

[6] Oluyede, E. O. 2006. *Fundamental Impact of Firing Syngas in Gas Turbines, Gas Turbine Industrial*

Fellowship Program. Project report.

[7] Giles, D. E., Som, S., and Aggarwal, S. K. 2006. "NO_x Emission Characteristics of Counterflow Syngas Diffusion Flames with Airstream Dilution." *Fuel* 85 (12-13): 1729-42.

[8] Zbeeb, K., and Ghenai, C. 2013. "Syngas Fuel Combustion in Re-circulating Vortex Combustor." *Journal of Energy and Power Engineering* 7 (10): 1852-64.

[9] Alavandi, S. K., and Agarwal, A. K. 2008. "Experimental Study of Combustion of Hydrogen-Syngas/Methane Fuel Mixtures in a Porous Burner." *International Journal of Hydrogen Energy* 33 (4): 1407-15.

[10] Schefer, R. W. 2001. "Combustion of Hydrogen Enriched Methane in a Lean Premixed Swirl Burner." Presented at the 2001 DOE (Department of Energy) Hydrogen Program Review, Baltimore, Maryland.

[11] Rahm, S., Goldmeer, J., Moilere, M., and Eranki, A. 2009. "Addressing Gas Turbine Fuel Flexibility." Presented at the Power-Gen Middle East Conference, Manama, Bahrain.

[12] Razbani, O., Mirzamohammad, N., and Assadi, M. 2011. "Literature Review and Road Map for Using Biogas in Internal Combustion Engines." Presented at the 3rd Internal Conference on Applied Energy, Perugia, Italy.

[13] Anggono, W., Wardana, I., Lawes, K., Hughes, K. J., Wahyudi, S., and Hamidi, N. 2012. "Laminar Burning Characteristics of Biogas-Air Mixtures in Spark Ignited Premix Combustion." *Journal of Applied Sciences Research* 8 (8): 4126-32.

[14] Barik, D., Sah, S., and Murugan, S. 2013. "Biogas Production and Storage for Fueling Internal Combustion Engines." *International Journal of Emerging Technology and Advanced Engineering* 3 (3): 193-202.

[15] Colorado, A. F., Herrera, B. F, and Amell, A. A. 2010. "Performance of Flameless Combustion Furnace Using Biogas and Natural Gas." *Bioresource Technology* 101 (7): 2443-9.

[16] Cheng, P. 1964. "Two-Dimensional Radiating Gas Flow by a Moment Method." *AIAA Journal* 2 (9):1662-4.

[17] Siegel, R., and Howell, J. R. 1992. *Thermal Radiation Heat Transfer*. Washington, DC: Hemisphere Publishing Corporation.

Journal of Energy and Power Engineering 9 (2015) 844-851
doi: 10.17265/1934-8975/2015.010.002

Improvement of Critical Heat Flux Performance by Wire Spacer

Dan Tri Le[1] and Minoru Takahashi[2]

1. Department of Nuclear Engineering, Tokyo Institute of Technology, Tokyo N1-18, 2-12-1, Japan

2. Research Laboratory for Nuclear Engineering, Tokyo Institute of Technology, Tokyo N1-18, 2-12-1, Japan

Received: July 27, 2015 / Accepted: September 07, 2015 / Published: October 31, 2015.

Abstract: In order to investigate the coolability of a tight lattice core in BWR (boiling water reactors), an experiment of CHF (critical heat flux) was conducted using a single heater pin flow channel with and without a wire spacer with the mass flux ranged from 200 kg/(m^2·s) to 600 kg/(m^2·s), the inlet temperature from 50 °C to 90 °C at the pressure of 0.1 MPa. The results of CHF values were compared between two different types of heater pin with and without the wire spacer. The heat removability of flow channel was improved by the wire spacer in comparison with the heater pin flow channel without the wire spacer. The CHF value was higher in the heater pin channel with the wire spacer than in that without the wire spacer.

Key words: Critical heat flux, tight lattice core, boiling two-phase flow, wire spacer.

Nomenclature

d	outer diameter of heater pin (m)
D	inner diameter of glass tube (m)
D_{he}	heated equivalent diameter (m)
D_{hy}	hydraulic diameter (m)
d_{wire}	wire diameter (m)
G	mass flux (kg/(m^2·s))
H	axial pitch of wire spacer (m)
L	heated length (m)
p	pressure (MPa)
q_{CHF}	critical heat flux (kW/m^2)
W	mass flow rate (kg/s)
x	thermal equilibrium steam quality
Z	distance from the upstream end of the heater pin to CHF position (m)

Greek letters

δ	gap size (m)

Abbreviations

BWR	boiling water reactor
CHF	critical heat flux
LWR	light water reactor

Corresponding author: Dan Tri Le, professor, research field: thermal hydraulic in nuclear reactor. E-mail: letridan.aa@m.titech.ac.jp.

1. Introduction

LWR (light water reactors), particularly BWR (boiling water reactors) core could have a higher conversion ratio nearly equal to unity by reducing moderator-fuel ratio [1]. In order to reduce the moderator to fuel ratio, tight lattice core with smaller coolant volume ratio compared with a normal core is one of the solutions. To be able to have a harder neutron spectrum event in the LWR, it is well known that, the tight lattice core with the pitch to diameter ratio, P/d, of nearly 1.09 [2] and 1.06 [3], which has the gap size distance of 1.3 mm and 0.9 mm, respectively, can be used. These values were much smaller than those of conventional LWR [4].

The use of wire spacers is more suitable for the tight lattice core than the use of grid spacers. However, from thermal-hydraulic point of view, coolability or heat removability is one of key issues for the feasibility of the tight lattice core with the wire spacer because of the small flow area which is related with the small value of rod-to-rod gap. Besides, the most important feature of coolability of tight lattice core is

the CHF (critical heat flux).

The study on the effect of gap size on CHF was well investigated by means of experiment in tight rod bundle with grid spacer [5]. From the results, the CHF values become lower with smaller gap size at the same mass flux.

In the previous study [6], the results of experiment performed using Freon-12 indicated the CHF in the hexagonal rod bundle with wire spacers was higher than that with grid spacers at low quality conditions. Then, CHF in water flow was evaluated by means of the fluid-to-fluid scaling law [7].

The effect of wire spacer on the promotion of CHF has been investigated for conventional fuel rod arrangement and for the round tube channel [8, 9]. The beneficial effect of circular shape wire on thermal hydraulic performance was made clear in the previous study [10].

There have been some studies on CHF in tight lattice core so far. Nevertheless, experimental data on the CHF for the tight lattice core with wire spacers are still limited. Thus, the critical heat flux or burnout phenomenon in tight lattice core with wire spacers is one of the most important studies for such kind of fuel assembly.

Therefore, in the present study, effect of circular shape wire spacer on the enhancement of CHF for the case of tight lattice arrangement was investigated by means of CHF experiment for single pin test section with a wire spacer with three difference values of gap size were chosen: 1.1, 1.5, 2.0 mm to cover the range at which the conversion ration could be nearly equal unity.

2. Experimental Apparatus and Procedure

2.1 Experimental Apparatus

Fig. 1 shows the experimental apparatus of a water circulation loop. It consists of the water tank, the circulation pump, the pre-heater, the orifice flow meter and the CHF test section. The inlet of the test section was 4,200 mm far from the outlet of the pre-heater so the water temperature is constant prior to get into the test section. The water flowed from the water tank through the circulation pump and the pre-heater and entered the test section. The valve which is located at the top of the apparatus was kept open to the air to be able to keep the system pressure equal to the atmospheric pressure.

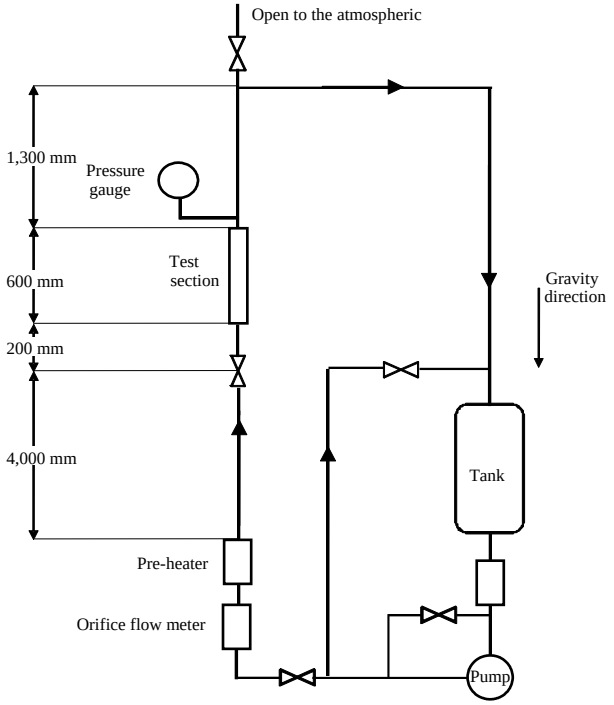

Fig. 1 Experimental apparatus.

2.2 Test Section

Fig. 2a shows the CHF test section oriented vertically. The main parts of the test section are the heater pin, the upper and bottom copper electrodes, the glass tube, the thermocouples and the wire spacer in case of experiment for a heater pin with a wire spacer. The heater pin was directly Joule-heated by a direct current electrically. The materials of the glass tube used were Pyrex glass and crystal glass.

The heater pin was made of a thin stainless steel tube with an outer diameter, *d*, of 8 mm and a length of 420 mm. It was connected to the copper electrodes at both ends by silver soldering. In the connection, the electrodes were inserted into the inside of the stainless steel tube in the depth of 10 mm before the soldering. Therefore, the heated length of the heater pin tube with a thin wall,

L, was 400 mm. On the other hand, the length to diameter ratio, *L*/*d*, of around 50 was large enough to suppress the effect of heated length on CHF [8]. The axial coil pitch of the wire, *H*, is the axial distance over which the wire completely wraps around the heater pin as shown in Fig. 2a. The axial pitch of the wire spacer, *H*, was set with two different values 100 mm and 200 mm. For this two different values of the axial pitch, the value of *H*/*d* less than 50 was the upper limit of the wire correlation for both CHF and pressure drop [8].

The cross section of the flow channel is shown in Fig. 2b. The spacer was electrically insulated from the heater pin. Fig. 2c shows the wire spacer made of a Teflon tube in which a stainless steel wire was inserted. Gap size, δ, is the distance from the outer surface of heater pin to the inner surface of the glass tube as shown in Fig. 2b. For the rod diameter of 8 mm, three different values of gap size were chosen: 1.1, 1.5 and 2.0 mm. By changing the rod diameter, wire diameter and glass inner diameter, we could change the size of the gap.

The direct Joule-heating of the heater pin provided an uniform heat flux on the heater pin surface. The maximum power and current of the power in this experiment were 15 kW and 500 A, respectively.

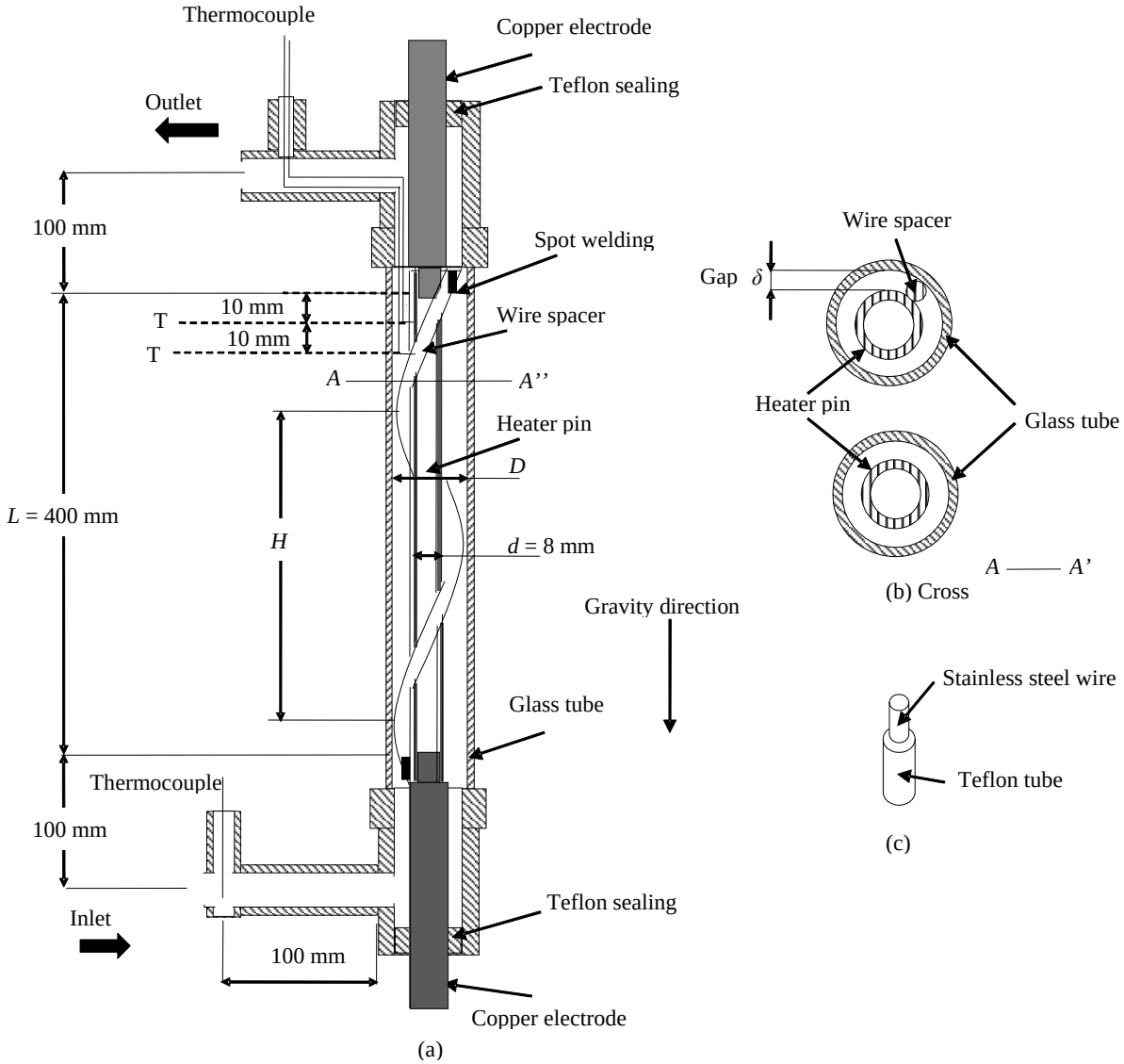

Fig. 2 Test section: (a) test section; (b) cross section of flow channel with wire and without wire spacer; (c) wire structure.

To detect a sudden temperature rise on the heater pin surface at the CHF condition and quickly shutdown the heating power, type K thermocouple elements with diameter of 100 μm were used for the surface heater pin temperature measurement. Fig. 2a shows that, the ends of the thermocouple elements were spot-welded to the surface to be hot junction at positions of 20 mm and 10 mm upstream from the downstream end of the heated length, being marked as T1 and T2, respectively. The effect of thermocouples on the CHF behavior can be neglected because its diameter is very small compared with the flow area.

Since the heater pin was directly heated by the current, the three points junction technique of thermocouple was used for compensation of voltage induced by the current between two point junctions.

In order to recognize the location of the reaching to the CHF, the position indications were written on the outside surface of the glass tube. By using thermocouples, the length indications and the camera, the positions of burnout or the arrival to the CHF were recognized.

2.3 Experimental Conditions

The experimental parameters and conditions are given in Table 1. Parameters in the experiment were the existence of the wire spacer, the gap size and the axial coil pitch of the wire, and the mass flux.

In order to investigate the effect of a wire spacer on CHF, the CHF experiments for both case of heater pin with and without a wire spacer were performed under the same mass flux condition. On the other hand, to be able to consider the effect of gap size on CHF, the experiments at the same mass flow rate were chosen.

2.4 Experimental Procedure and Measurement Items

The water from the water tank was circulated in the loop by using the circulation pump. Water was heated up by the pre-heater before starting the experiment. The water in the water circulation loop was degassed initially by boiling the water in the test section for a

Table 1 Experimental condition.

Parameter	Run No.1 with wire	Run No.2 without wire	Run No.3 with wire	Run No.4 with wire	Run No.5 with wire	Run No.6 with wire	Run No.7 with wire
Inner diameter of glass tube, D (mm)	12	12	11	12	11	10.2	11
Gap size, δ (mm)	2.0	2.0	1.5	2.0	1.5	1.1	1.5
Wire diameter, d_w (mm)	1.79	-	1.4	1.79	1.4	1.06	1.4
Wire axial pitch, H (mm)	200	-	200	200	200	200	100
Mass flux, G (kg/(m^2·s))	400	400	658	-	-	-	-
Mass flow rate, W (kg/s)	-	-	-	0.018	0.018	0.018	0.018
Hydraulic diameter of flow channel, D_{hy} (m)	0.0035	0.004	0.0027	0.0035	0.0027	0.002	0.0027
Pressure, p (MPa)	0.1	0.1	0.1	0.1	0.1	0.1	0.1
Inlet temperature (K)	335.3	334.5	336.9	338	331	337.5	330.5
	336.5	339.7	342.1	343	331.5	338	340.4
	343.4	345.2	346	348.6	337	341.4	350
	344.9	347.8	349.2	348.8	342	355.3	350.5
	347.2	353.3	351.5	354.7	349.5	366	356
	349.6	361.5	357.5	-	353	-	-
	355	362.3	359.6	-	357	-	-
	357.8	-	-	-	367.6	-	-
	361.5	-	-	-	-	-	-
	365.9	-	-	-	-	-	-

while until air dissolved in the water was removed sufficiently.

During the experiment, the water flow rate was kept constant. The flow resistance at the inlet valve of the test section was kept high enough to suppress the instability of flow rate due to the instability of pressure drop of two-phase flow in the test section. When the water temperature was kept constant at the inlet of the test section reached the desired value by controlling the pre-heater, the electric power to the heater pin in the test section was increased gradually by remote controlling.

Surface temperature of the heat pin was measured and recorded by using the thermocouples with the sampling frequency of 100 Hz. The power of the heater pin was increased step by step until the surface temperature of the heater pin rapidly and suddenly increased because of reaching the CHF condition. Immediately after reaching the CHF condition, the power source was automatically shut down by the signal of sudden rise of surface temperature.

Fig. 3 shows the behaviors of the measured surface and inlet temperatures, voltage and current during the operation. It can be seen that, the inlet temperature was kept constant. The surface temperatures T1 and T2 increased slightly due to the increase of the electric power to the heater pin, and then suddenly the surface temperatures of the heater pin T1 and T2 rapidly increased. It was judged that, at this time, the burn-out took place or the heat flux reached the CHF.

The experimental data of the CHF were obtained in the range of mass flux and inlet temperature mentioned above with three different values of δ and two different values of wire pitch, H. The measurements were made under the boiling two-phase flow condition. The measurement accuracy of the heat flux value was high enough since it was determined from measured voltage and current. In order to keep the uncertainty of the results small, only the experimental data obtained under the condition which met the following requirements were chosen:

- The flow rate was stable during the experiment;
- The inlet temperature fluctuated within 1 K.

3. Results and Discussion

3.1 Comparison with Look up Table Data

Following Fig. 4 [11, 12], the calculated values were obtained by using the CHF correlation with the rod-centered approach [11] and the 2006 CHF [12] look up table data. The results were close to the experimental results of heater pin without a wire spacer.

3.2 Effect of Wire Spacer

Fig. 5 shows the comparison of the CHF values of

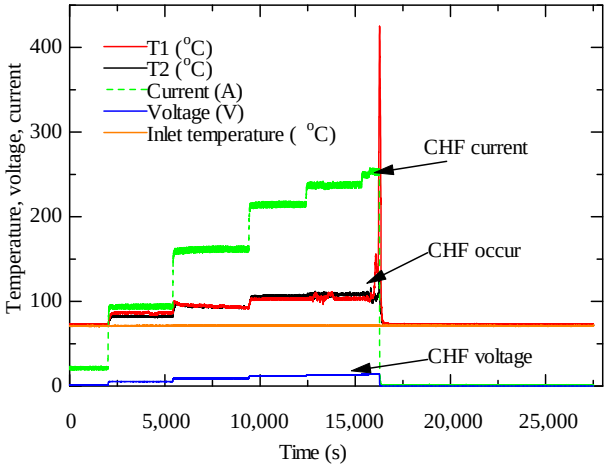

Fig. 3 Temperature behavior during the experiment.

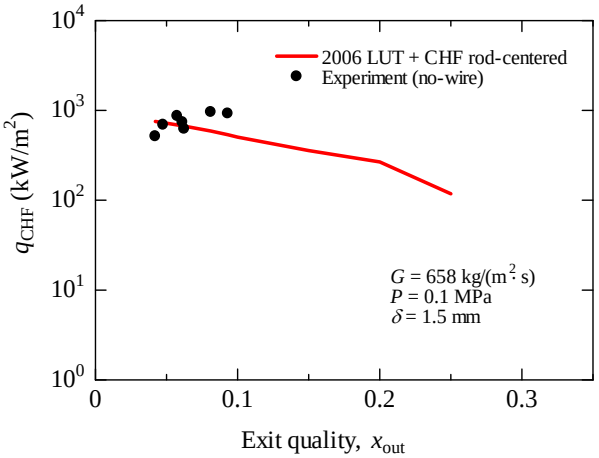

Fig. 4 Comparison of experimental results with the calculated results using CHF correlation for the rod-centered approach for the CHF look-up table.

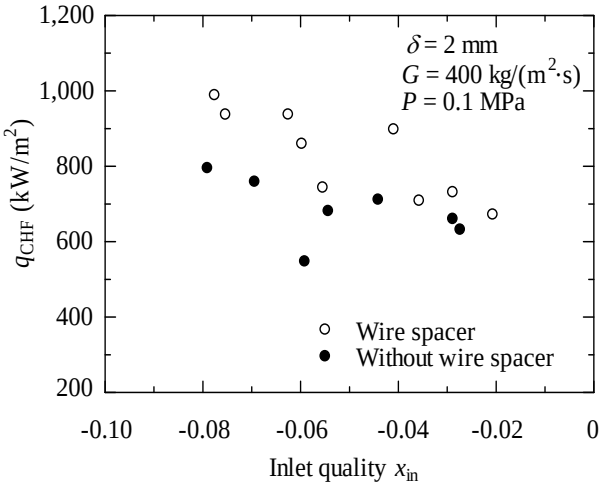

Fig. 5 Critical heat flux base on inlet condition.

single pin channels between with the wire spacer and without the wire spacer. It was found that, the CHF values in both types of heater pin decreased with the decrease of the inlet equilibrium steam quality, x_{in}. However, the CHF values were higher in case of heater pin with the wire spacer than that in case of heater pin without the wire spacer. It could be explained by the enhancement of bubble removal from the heated surface due to the effect of wire and spiral flow. Compared with the work of Cheng and Müller [6], the results of the present study were obtained in smaller range of the quality from -0.1 to 0. However, it can be seen that, the CHF values of wire type were still higher than those without wire type even if the inlet equilibrium steam quality was close to zero. Besides, the difference in the CHF values between heater pin with and without wire spacer was larger in lower qualities compared with the difference of CHF in higher qualities.

In furtherance of the investigation of CHF behavior under the effect of the wire spacer, the change in wire spacer size is needed. Therefore, the CHF experiment with different value of δ and H was performed to deal with such kind of study. These experiments were performed under the same flow rate condition of the practical reactor rather than the same mass flux. From reactor design point of view, the consideration of the same water flow rate rather than the same mass flux is needed to be able to keep the best coolability for difference core design. Fig. 6 shows the comparison of the CHF values between three different values of gap size at the same flow rate. It can be seen that, at the same local quality, x_z, the CHF values were enhanced with the decrease of gap size under the same flow rate condition. In more detail, the CHF values were higher in case of smaller gap size and it was the highest in case of the smallest gap size. That is because the channel which has the smallest flow area has the highest mass flux at the same water mass flow rate which leads to the enhancement of CHF values. Moreover, there is an effect of the water film along the inner surface of the channel (glass tube) on CHF values. At the low quality region and bigger channel, this effect does not have the big influence on CHF value. However, at the high quality region and smaller gap size, the cold wall effect became higher. In detail, the vapor velocity was high in case of high quality region due to the high evaporation rate. Therefore, it may disturb the water film which flow along the inner surface of the channel and bring the drop let to the heated surface, which cause of increasing of droplet deposition rate. This phenomena lead to the increase of CHF values at high quality region. On the other hand, with the smaller gap size, the droplet concentration in the vapor phase also higher compared with it in case of bigger gap size. This is another reason which contributed for the increase of CHF values.

On the other hand, according to Fig. 6, the experiment with smaller gap size could reach higher CHF values and also could go to the higher local quality, x_z. Moreover, in case of bigger gap size (δ = 2.0 mm), the CHF value tended to decrease with the increase of quality. However, in case of flow channel with small gap size, the CHF values were nearly constant value or slightly increase with the increasing of quality.

Fig. 7 illustrates the CHF results in two different values of wire pitch, H. It can be seen that, the CHF values were nearly the same between two different

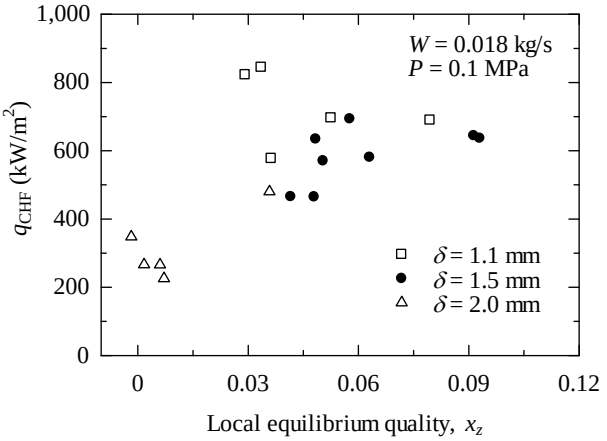

Fig. 6 Critical heat flux of three different values of gap size.

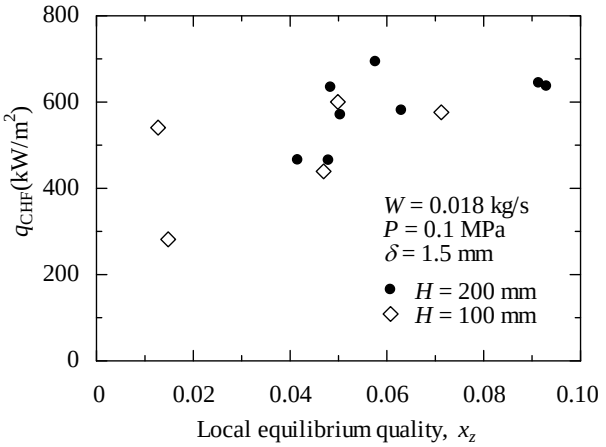

Fig. 7 Critical heat flux of two different values of wire pitch, *H*.

values of *H*. It can be explained that, there were two flow channels with two different values of wire pitch, velocity was the same. Since the velocity was the same, the mass flux was the same. Therefore, it is clear that, the axial pitch did not have a large influence on the CHF. However, it is necessary to consider about the pressure drop for the design purpose at the same time.

3.3 Axial Position of CHF

The relation between the CHF values and the heated length to the position of arriving at CHF is shown in Fig. 8.

It is found that, at the same mass flow rate, *W*, the CHF occurred mostly in the downstream of the flow channel. Fig. 8 also shows the comparison of CHF position among three different values of gap size. In

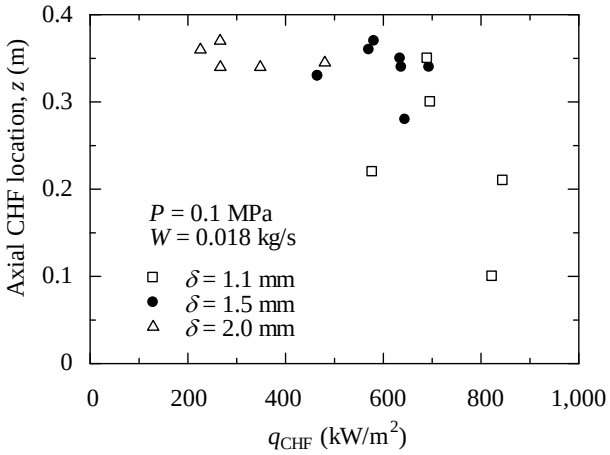

Fig. 8 Critical heat flux base on the heated length.

case of gap size of 1.5 mm and 2.0 mm, the CHF positions were mainly at the downstream of flow channel. Therefore, the CHF in this case was principally caused by liquid film dry-out. On the other hand, with the smallest flow area, gap size of 1.1 mm, there was the possibility of CHF occurring at the upstream of flow channel because of the high heat flux and high flow rate. According to the results, the CHF positions changed slightly with different values of the flow area or gap size. The CHF position tended to move from downstream to the upstream of the flow channel due to the decrease of gap size.

4. Conclusions

The CHF phenomena for the tight lattice fuel arrangement with the effect of wire spacer were investigated by mean of the experiment for single fuel pin with and without wire spacer and three difference values of gap size of 1.1, 1.5, 2.0 mm. Besides, the effect of wire pitch was made clear by the experiment with two dissimilar wire pitch value of 100 mm and 200 mm. The conclusions are as follows:

- The CHF in case of heater pin with circular shape wire was enhanced up to 25% compared with it in case of without wire space under the same flow condition. Therefore, the coolability or heat removability was enhanced by the existence of the wire spacer and spiral flow;
- With the same flow rate condition, the CHF

values can be increased up to 100% with the decrease of gap size. Therefore, the flow channel with smaller gap size a higher coolability compared with the flow channel with larger gap size;

• The change in a pitch of wire, *H*, with two difference values of 100 mm and 200 mm, did not have a large influence on the CHF if the mass flux was kept constant. The experiment data were nearly the same value even with two different cases of wire pitch.

Acknowledgments

The study was supported by Hitachi Nuclear Scholarship project. The authors would like to give the thank to Dr. Noriaki Inaba and Dr. Masatoshi Kondo for their discussion and Mr. Shoji Matsui for his assistance in the technical work.

References

[1] Sidik, P., Takaki, N., and Sekimoto, H. 2006. "Impact of Different Moderator Ratios with Light and Heavy Water Cooled Reactor in Equilibrium States." *Annals of Nuclear Energy* 33 (7): 561.

[2] Uchikawa, S., Okubo, T., Kugo, T., Akie, H., Takeda, R., Nakano, Y., Ohnuki, A., and Iwamura, T. 2006. "Conceptual Design of Innovative Water Reactor for Flexible Fuel Cycle (FLWR) and Its Recycle Characteristics." *Journal of Nuclear Science and Technology* 44 (3): 277-84.

[3] Sidik, P., Takaki, N., and Sekimoto, H. 2008. "Preliminary Study on Feasibility of Large and Small Water Cooled Thorium Breeder Reactor in Equilibrium Sates." *Progress in Nuclear Energy* 50 (2-6): 320-4.

[4] Syeilendra, P. 2013. "Study on Hydrodynamic Model of Fuel Subassembly with Wire-Wrapped Rods for Nuclear Reactors." Doctoral dissertation, Tokyo Institute of Technology.

[5] Tamai, H., Kureta, M., Liu, W., Sato, T., Ohnuki, A., and Akimoto, H. 2007. "Gap Width Effect on Critical Power Based on Tight-Lattice 37-Rod Bundle Experiments." *Journal of Nuclear Science and Technology* 44 (1): 54-63.

[6] Cheng, X., and Müller, U. 1998. "Critical Heat Flux and Turbulent Mixing in Hexagonal Tight Rod Bundles." *International Journal of Multiphase Flow* 24 (8): 1245-63.

[7] Courtaud, M., Deruaz, R., and D'Aillon, L. G. 1988. "The French Thermal-hydraulic Program Addressing the Requirements of the Future Pressurized Water Reactors." *Nucl. Technol.* 80 (1): 73-82.

[8] Diller, P., Todreas, N., and Hejzlar, P. 2009. "Thermal-Hydraulic Analysis for Wire-Wrapped PWR Cores." *Nuclear Engineering and Design* 239 (8): 1461-70.

[9] Celata, G. P., Cumo, M., and Mariani, A. 1994. "Echancement of CHF Water Subcooled Flow Boiling Tubes Using Helically Coiled Wires." *International Journal of Heat and Mass Transfer* 37 (1): 52-67.

[10] Wasim, R, and Kwang, Y. K. 2008. "Effects of Wire-Spacer Shape in LMR on Thermal-Hydraulic Performance." *Nuclear Engineering and Design* 238 (10): 2678-83.

[11] Doerffer, S., Groeneveld, D. C., Cheng, S. C., and Rudzinski, K. F. 1994. "A Comparison of Critical Heat Flux in Tubes and Annuli." *Nuclear Engineering and Design* 149 (1-3): 167-75.

[12] Groeneveld, D. C., Shan, J. Q., Vasić, A. Z., Leung, L. K. H., Durmayaz, A., Yang. J., Cheng, S. C., and Tanase, A. 2007. "The 2006 CHF Look-up Table." *Nuclear Engineering and Design* 237 (15-17): 1909-22.

Journal of Energy and Power Engineering 9 (2015) 852-859
doi: 10.17265/1934-8975/2015.010.003

A Novel Technology for Generation of Electricity and Cold by Using Energy Potential of Transmission Line's High Pressure Gas

Zohrab Melikyan

HVAC Department, National University of Architecture and Construction of Armenia, Yerevan 0009, Armenia

Received: July 28, 2015 / Accepted: September 07, 2015 / Published: October 31, 2015.

Abstract: The main objective of this paper is to develop a novel technology for combined generation of electricity and cold by using energy potential of transmission line's high pressure gas. For this purpose, the reduction of high pressure of the gas in gas distribution station instead of useless expansion throttling process is suggested to realize by adiabatic expansion, which is executed in a gas expanding turbine. Herewith, the gas distribution station is turned into energy and cold generating plant. Simultaneous operation of energy and cold generating plant is described. A method and appropriate formulas for determination of design characteristics of considered plant are suggested. A new method for reveres order of calculation and design of the cold store based on the use of expanded cold gas as cooling agent is developed. Calculations and analysis prove high energy efficiency of suggested technology, the wide use of which will provide significant production of cheap electricity and cold and as well as reduction of fossil fuel consumption.

Key words: Natural gas, gas distribution station, throttling valve, turbo-expander, isenthalpic, adiabatic.

1. Introduction

At the end of main supply pipelines of gas transporting systems, the gas still possesses rather high pressure reaching up to 2,000 kPa. However, such a high pressure of the gas needs to be reduced to 300 kPa before gas distribution by low or medium pressure networks of towns. Usually in gas distribution stations, the gas pressure is reduced mainly by throttling processes in throttling valves. Nevertheless, the throttling of the gas eliminates its energy residual potential, while it could be converted into useful electricity or cold, the use of which will provide rather large public benefit, and as well as keeping the environment free of greenhouse gases emissions. To realize such a goal, an attempt has been done to develop a novel technology serving for generating energy and cold by using transportaion pipeline's gas.

Corresponding author: Zohrab Melikyan, Dr., professor, research fields: gas distribution engineering, refrigeration engineering and air conditioning. E-mail: zohrabmelikyan@yahoo.com.

2. Analysis of Energy Generating Gas Expansion Thermodynamic Processes

In gas distribution stations for reducing the pressure of the gas, traditionally isenthalpic thermodynamic process of throttling is being used. The state of natural gas in underground gas transporting pipeline, just before throttling, is characterized by pressure P_1 = 2,000 kPa and by temperature of the ground, assumed t_1 = 10 °C. The state of the gas with mentioned parameters is represented by the point "1" on enthalpy—pressure (i-log$P$) diagram of natural gas (methane) [1] which is given in Fig. 1.

In the diagram the isenthalpic throttling expansion process from initial pressure P_1 = 2,000 kPa to final low pressure $P_{1'tr}$ = 300 kPa is represented by the line "1-1'tr". In this process, the gas is cooled from t_1 = 10 °C to $t_{1'tr}$ = 0 °C. The power N (kW), in

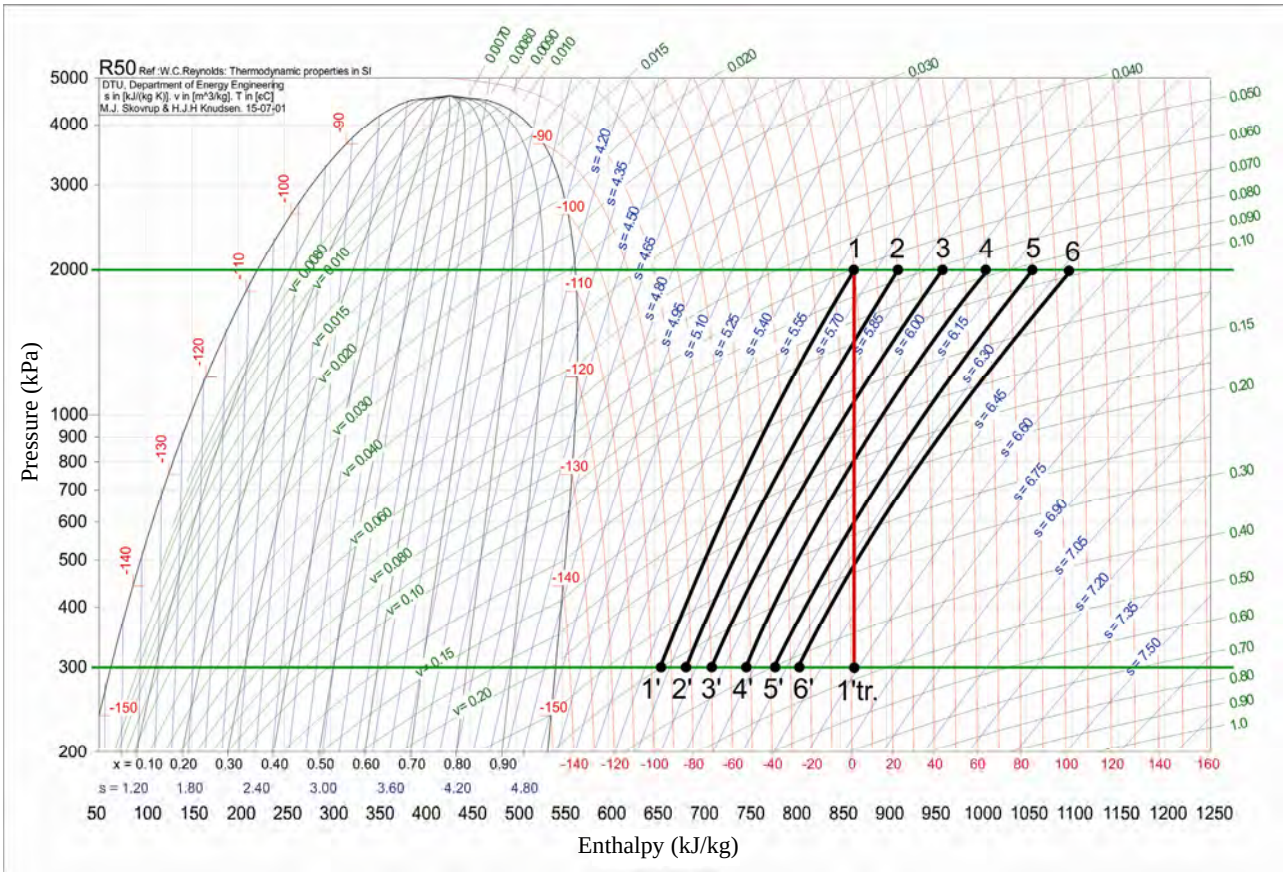

Fig. 1 Isentropic and adiabatic expansion processes of natural gas from 2,000 kPa to 300 kPa on (*i*-log*P*) diagram at different initial temperatures of the gas.

expansion processes is determined by Eq. (1) [2]:

$$N = G_{g.spp}\Delta i \quad (1)$$

where, $G_{g.spp}$—mass flow rate of gas in gas expanding equipment (kg/s); Δi—difference of initial and final specific enthalpies of gas (kJ/kg).

As isenthalpic throttling process takes place without change of enthalpy, no work is executed.

3. Developing of Gas Distribution Modified Station for Combined Generation of Electricity and Cooled Gas

Eq. (1) allows concluding that, gas distribution stations can perform as rather big sources of energy, if they are furnished with gas adiabatic expansion equipment. For this purpose, it is suggested to replace the throttling valve of conventional gas distribution station by turbo-expander. In this case, the high pressure transmission pipeline gas with initial enthalpy i_1 = 860 kJ/kg is expanded adiabatically from 2,000 kPa to 300 kPa and rotates the wheel of turbo-expander. On the driving shaft of turbo-expander, an electric generator is mounted which converts the energy of rotation into electricity. As can be seen from Fig. 1, due to adiabatic expansion, the gas at the outlet of turbo-expander gets temperature -110 °C and enthalpy $i_{1'}$ = 660 kJ/kg. Supplying of such a cold gas into distribution network is not allowed [3, 4]. For this reason, before expansion in turbo-expander, it is becoming necessary to heat the gas from +10 °C to an appropriate temperature. After expansion, the gas of lower pressure is supplied into gas distribution network or into heat exchanger of the cold store, where is used as cooling agent. The cold store is built in proximity of the gas distribution station, where cold gas is used for cooling the stored food, for instance

meat. In such cold store, the inside temperature should be kept at -18 °C to -20 °C [5]. However, the expanded gas at the outlet of turbo-expander gets much lower temperature, than -18 °C. For avoiding freezing of stored goods, the temperature of gas at the outlet of turbo-expander should be approximately -25 °C. From Fig. 1, it is clear that for obtaining -25 °C final temperature at the outlet of turbo-expander, the initial temperature of the gas at the inlet should be t_6 = 105 °C (see processes 6-6', Fig. 1). However, temperature of the high pressure gas in underground transmission main pipeline is +10 °C. Therefore, for providing -25 °C, final temperature the main pipeline gas, before entering into turbo-expander, should be preheated from 10 °C to 105 °C in a gas heater.

4. Structure of Gas Distribution Station of Energy and Cooled Gas Generation, Equipped with a Preheater

The scheme of gas distribution station with combined production of electricity and cooled gas, equipped with gas heater is given in Fig. 2.

Preheating of the gas can be accomplished in a simple apparatus, the sketch of which is given in Fig. 3.

In fact, the suggested gas heater is a sealed furnace with round masonry made of fire resistant brick. In the bottom of fire chamber, which is covered with steel sheet, the gas burner is adjusted. The burner of fuel gas is connected with fuel gas pipe. From gas transporting main pipeline, the gas with temperature 10 °C passes to the annulus gap between fire chamber and brick vertical cylinder where is heated up to 105 °C. The flue gases are extracted outside through the chimney. Heated gas enters into turbo-expander where is expanded adiabatically and is cooled. The quantity of fuel $B_{f.gas}$ (m^3/h), consumed for preheating of high pressure gas is determined by the following ratio:

$$B_{f.gas} = \frac{Q_{pr.heat}}{\eta_{gas.heat} Q_{gas}} \quad (2)$$

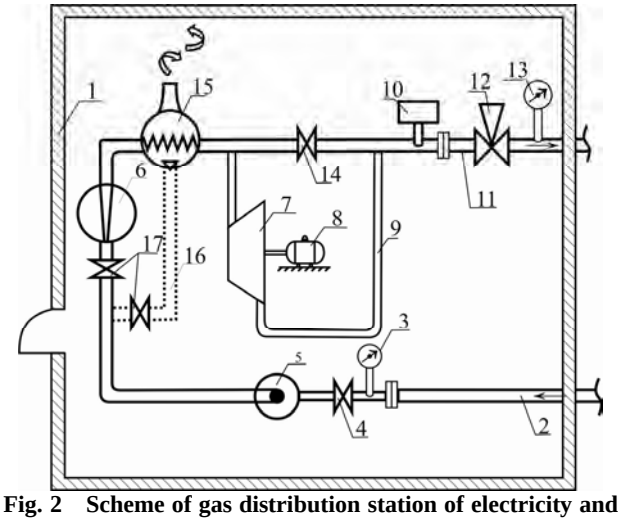

Fig. 2 Scheme of gas distribution station of electricity and cooled gas combined generation.

1—gas distribution station house, 2—gas transportation main pipeline, 3—manometer, 4—gas flow controlling valve, 5—oil strainer, 6—gas flow meter, 7—turbo-expander, 8—electric generator, 9—medium pressure gas pipeline, 10—gas odorizer, 11—odorized gas supply tube to gas distribution network, 12—gas pressure automatic controller, 13—manometer, 14—by-passing valve, 15—heater of high pressure gas, 16—fuel gas pipe, 17—valves.

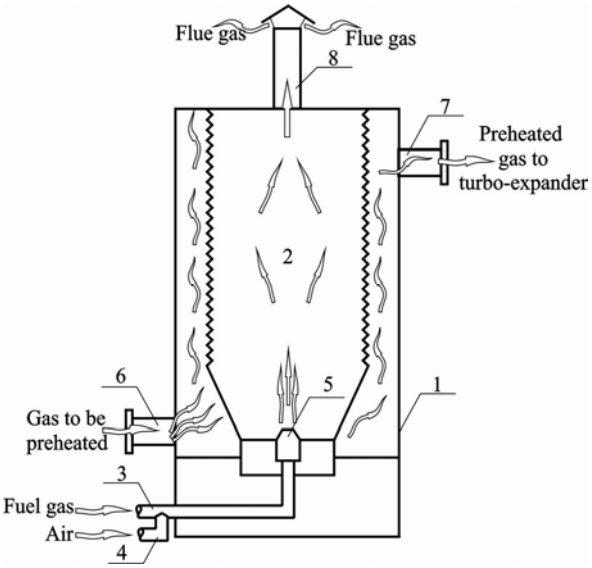

Fig. 3 Sketch of gas heater.

1—insulated cylinder made of fire-resistant brick, 2—fire chamber with heating steel surface, 3—fuel-gas pipe, 4—air pipe to gas burner, 5—fuel gas burner, 6—high pressure gas to be heated, 7—tube of preheated gas to turbo-expander, 8—chimney.

where, $Q_{pr.heat}$—required heat for gas preheating (kW), $\eta_{gas.heat}$—COP of gas heater, which can be assumed $\eta_{gas.heat}$ = 0.85, Q_{gas}—gas combustion specific heat,

assumed Q_{gas} = 9.3 kWh/m^3.

The required heat $Q_{pr.heat}$ (kW) needed for gas preheating, is determined by Eq. (3):

$$Q_{pr.heat} = G_{g.spp} c_{gas} \left(t_{g1} - t_g\right) \quad (3)$$

where, $G_{g.spp}$—mass flow rate of gas being preheated (kg/s), c_{gas}—specific heat of natural gas which equals to 2.22 kJ/(kg·°C) [6], t_{g1} = 105 °C—temperature of preheated gas at the inlet of turbo-expander (°C), t_g = 10 °C—temperature of the gas at the end of main gas transporting pipeline (°C).

Solving together Eqs. (3) and (2) and making some simplifications, the following formula for determining the quantity of fuel gas $B_{f.gas}$ (m^3/h) is obtained:

$$B_{f.gas} = \frac{G_{g.spp} c_{gas} (t_{g1} - t_g)}{\eta_{gas.heat} Q_{gas}} \quad (4)$$

The value of $G_{g.spp}$ (kg/s), can be determined by the formula as follows:

$$G_{g.spp} = \frac{v_{g.spp} \cdot n_{pers} \cdot \rho_{gas} \cdot \omega}{8,760 \times 3,600} \quad (5)$$

where, $v_{g.spp}$—annual gas consumption by one resident of urban district (m^3/person per year) [3], n_{pers}—number of gas consumers in urban district, ρ_{gas} = 0.7 kg/m^3—density of natural gas.

The capacity factor is determined by dividing the actual output with the maximum possible output. The capacity factor for gas supply distribution system, operating with base load regime is assumed ω = 0.9 [4].

Taking into account that, annual gas consumption by 1 resident makes $v_{g.spp}$ = 470 m^3/(person per year) [4], for a medium city with n_{pers} = 1,000,000 residents, the mass flow rate of gas $G_{g.spp}$ (kg/s), which passes through the turbo-expander and is totally supplied to the urban districts distribution network, calculated by Eq. (5) makes:

$$G_{g.spp} = \frac{470 \times 1,000,000 \times 0.7 \times 0.9}{8,760 \times 3,600} = 9.4 \text{ kg/s, or}$$

9.4 kg/s/(0.7 m^3/kg) = 13.4 m^3/s, or 48,288 m^3/h or 423,000,000 m^3/year.

Assuming as well that, specific heat of gas c_{gas} = 2.22 kJ/(kg·°C) [6], t_{g1} = 105 °C, t_g = 10 °C, $\eta_{gas.heat}$ = 0.85 and Q_{gas} = 9.3 kWh/m^3, by the help of Eq. (4), the following quantity of fuel gas consumption $B_{f.gas}$ (m^3/h) is obtained:

$$B_{f.gas} = \frac{9.4 \times 2.22 \times (105 - 10)}{0.85 \times 9.3} = 251 \text{ m}^3\text{/h}$$

So, the quantity of fuel gas $B_{f.gas}$ = 251 m^3/h, consumed for preheating of the gas with quantity $G_{g.spp}$ = 48,288 m^3/h, supplied to the district's gas distribution network or to the cold store, makes only 0.52% of the whole gas, supplied to the network.

5. Quantity of Electric Energy Generated by the Set of Turbo-Expander and Electric Generator

The specific quantity of energy L (J/kg), produced in turbo-expander in consequence of adiabatic process of gas expansion is determined by Eq. (6) [8]:

$$L = \frac{ZRT_1}{k-1}\left[1 - \left(\frac{P_2}{P_1}\right)^{\frac{k-1}{k}}\right] \quad (6)$$

where, Z = 1.04—compressibility factor of natural gas [8], R—gas constant of natural gas (methane) equal to 518.3 J/(kg·°C) [9], T_1 = (105 + 273) = 378 K—initial temperature of preheated gas at the inlet of turbo-expander, k = 1.31—adiabatic or isentropic exponent for methane equal to 1.31 [9], P_1 and P_2—pressures of the gas at the inlet and outlet of turbo-expander (kPa).

As can be seen from Eq. (6), the quantity of energy produced by turbo-expander depends mainly on expansion rate P_2/P_1. In developed gas distribution station, the expansion ratio of natural gas in turbo-expander makes: P_2/P_1 = 300/2,000 = 0.15. According to Eq. (6) and above given thermo-physical data of natural gas, the produced specific energy L

makes:

$$L = \frac{1.04 \times 518.3 \times (105 + 273)}{1.31 - 1}\left[1 - (0.15)^{\frac{1.31-1}{1.31}}\right] =$$
$$= 657,271\,(1 - 0.637) = 238,000 \text{ J / kg or } 238 \text{ kJ / kg}$$

Taking into account that, the whole $G_{g.spp}$ = 9.56 kg/s gas is expanded in turbo-expander, the absolute value of electric power will make N = 9.56 × 238 = 2,275.3 kW.

Summarizing the results of above investigation, it is becoming clear that, the modified gas distribution station turns to an electric power plant with N = 2,275.3 kW, or 2.275 MW electric power. The annual production of electricity of this power plant makes 2,275.3 kW × 8,760 h = 19,931,628 kWh, which can be sold to the city electricity network utility company for 19,931,628 kWh × 0.09 $/kWh = 1,793,847 $/year (0.09 $/kWh—tariff of electricity for instance in Armenia). Should be taken into account that, if turbo-expander is charged in 50% of its power, its energy efficiency decreases in 18%-20%.

6. Structure and Operation of Cold Store Functioning with Gas Cooling Agent

Besides electricity generation, the modified gas distribution station can operate as well as a cold store. To realize of this purpose the cooled gas at temperature $t_{c.g.1}$ = -25 °C is supplied from turbo-expander into air to gas heat exchanger installed inside the cold store [10]. Here, it takes heat from cold store air, which circulates through heat exchanger and is wormed from $t_{c.g.1}$ = -25 °C to temperature $t_{c.g.2}$ = -23 °C. At the same time, the cold store air at temperature $t_{c.st.1}$ = -18 °C enters into heat exchanger and is cooled to $t_{c.st.2}$ = -19 °C. The partially warmed gas moving from heat exchanger to low pressure distribution network at temperature $t_{c.g.2}$ = -23 °C still is too cold to be supplied into district distribution network. For avoiding damages of gas network, a necessity of secondary heating of the low pressure gas, before supplying to urban gas distribution low pressure network arises. The simplified scheme of modified gas distribution station, equipped with gas turbo-expander, electric generator, primary and secondary gas heaters and cold store is represented in Fig. 4.

The suggested cold store operates in the following way: the gas with temperature t_g = 10 °C from high pressure gas transmission main pipeline (1) enters into primary gas heater (2) where is heated to $t_{g.1}$ = 105 °C and by suction line is inhaled into turbo-expander (3) where is expanded adiabatically and is cooled to $t_{c.g.1}$ = -25 °C. By pipe (5), the cooled gas enters into heat exchanger (7), installed in the cold store (6) [5]. As a result of heat absorption from stored food (8), and all other heat gains the gas is warmed to $t_{c.g.2}$ = -23 °C and by pipe (9) is directed to secondary gas heater (10). In this heater, gas is secondary heated to admissible temperature t_g = +5 °C which allows to escape damaging of gas distribution network. Passing the pressure controller (11) the low pressure gas is supplied to the main pipeline (12) of low pressure gas supply urban network.

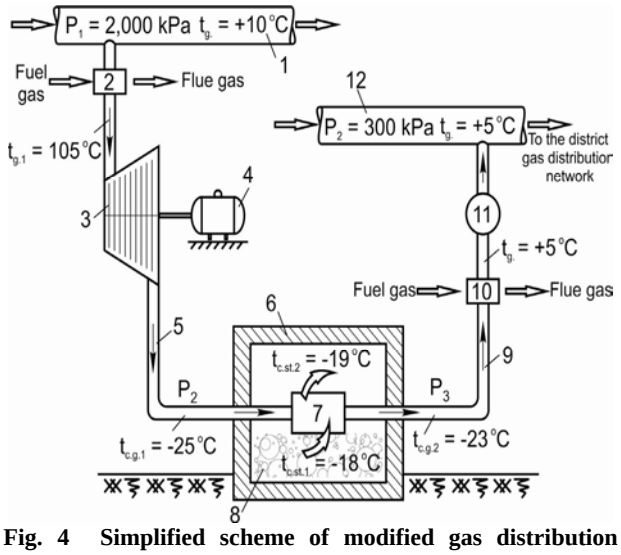

Fig. 4 Simplified scheme of modified gas distribution station equipped with gas turbo-expander, electric generator and cold store.

1—high pressure gas transmission main pipeline, 2—primary gas heater, 3—gas turbo-expander, 4—electric generator, 5—pipe of cooled gas, 6—thermoinsulated cold store, 7—air to gas heat exchanger, 8—stored food, 9—partially warmed gas pipeline, 10—gas secondary heater, 11—pressure controller, 12—main pipeline of low pressure gas distribution network.

7. Reversal Method for Calculation and Design of Suggested Cold Store

In contrast to ordinary cold stores, the calculation and design of the suggested one is executed in opposite way. That is to say, for ordinary cold stores, the tonnage: construction, sizes, kinds and quantity of stored food and other characteristics of the cold store are given. Based on listed data, the values of heat gains, cooling demand and all characteristics of refrigeration equipment are determined. For considered cold store, only the cooling capacity in form of quantity of cooled gas and its temperature are available. In such conditions tonnage, construction sizes of the cold store and other characteristics have to be determined. The cooling capacity of suggested cold store $Q_{c.st.}$ (kW) can be determined by the following balance of heat flows:

$$Q_{c.st.} = Q_{av.} - Q_{h.g.} - Q_{int.} - Q_{vent.} \quad (7)$$

where, $Q_{av.}$—available cooling capacity of natural gas, cooled in turbo-expander (kW), $Q_{h.g.}$—heat gains through external constructions of cold store (kW), $Q_{int.}$—internal heat rejections from personnel, and electric and lighting equipment (kW), $Q_{vent.}$—heat, transferred from ventilation air to cold store's internal air (kW).

The value of available cooling capacity of natural gas, cooled in turbo-expander, $Q_{av.}$ (kW), is determined by the expression as follows:

$$Q_{av.} = G_{g.spp} \cdot c_{gas} \cdot T_{c.g} \quad (8)$$

where, $T_{c.g}$ = -25 + 273 = 248 K—absolute temperature of cold gas at the outlet of turbo-expander.

Therefore:

$$Q_{av.} = 9.4\,\text{kg/s} \times 2.22\,\text{kJ/(kg} \cdot \text{K)} \times 248\,\text{K} = 5{,}175\,\text{kW}$$

which should compensate all mentioned heat flows, that is to say:

$$Q_{av.} = Q_{c.st.} + Q_{h.g.} + Q_{int.} + Q_{vent.} \quad (8')$$

The suggested reversal method recommends designing the cold store based on assumptions of values of heat flows as parts of available cooling capacity $Q_{av.}$ of natural gas. The further designing of constructions, sizes and equipment should be realized in a way to provide quoted heat flows. According to the following quotas, the heat flows are the followings:

(1) heat gains through external constructions of cold store $Q_{h.g.} = 0.35Q_{av.} = 0.35 \times 5{,}175$ kW = 1,811 kW;

(2) internal heat rejections from personnel and equipment $Q_{int.} = 0.2Q_{av.} = 0.2 \times 5{,}175$ kW = 1,035 kW;

(3) heat, transferred from ventilation air to cold store's air, $Q_{vent.} = 0.2Q_{av.} = 0.2 \times 5{,}263$ kW = 1,035 kW.

Total heat gains make:

$$Q_{tot.h.fl.} = 1{,}811 + 1{,}035 + 1{,}035 = 3{,}881 \text{ W}$$

Quantity of heat $Q_{c.st.}$ (kW) rejected from stored food will be the rest of available cooling capacity of the natural gas, i.e.,

$$Q_{c.st.} = Q_{av.} - Q_{tot.h.fl} = 5{,}175 - 3{,}881 = 1{,}294 \text{ kW} \quad (9)$$

So, quantity of heat $Q_{c.st.}$ (kW), rejected from stored food, which actually is the cooling capacity of cold store is calculated by Eq. (10):

$$Q_{c.st.} = G_{f.spp}\left(i_{f.1} - i_{f.2}\right) \quad (10)$$

where, $G_{f.spp}$—quantity of chilled fresh food supplied into cold store (kg/s), $i_{f.1}$ = 72 kJ/kg [11]—initial enthalpy of preliminary chilled fresh meat supplied with temperature $t_{f.1}$ = -10 °C, $i_{f.2}$ = 47 kJ/kg [11]—final enthalpy of stored meat at cold store's temperature $t_{f.2}$ = -18 °C.

From Eq. (10), follows the equation, allowing to determining quantity of chilled fresh food (meat) supplied into cold store, $G_{f.spp}$ (kg/s):

$$G_{f.spp} = \frac{Q_{c.st.}}{i_{f.1} - i_{f.2}} \quad (11)$$

Substitute above data for quantities in Eq. (11) and making calculations will obtain the following value of $G_{f.spp}$ (kg/s):

$$G_{f.spp} = \frac{1{,}294\,\text{kW}}{(72-47)\,\text{kJ/kg}} = \frac{1{,}294\,\text{kW}}{25\,\text{kJ/kg}} = 51.8\,\text{kg/s} \quad (11)$$

or 186,480 kg/h; or 4,475,520 kg/day; or 4,475.5 ton/day.

The tonnage M (kg) of cold store is determined by

the following Eq. (12) [12]:

$$M = \frac{G_{f.spp} \times 305}{B \cdot m} \quad (12)$$

where, 305—number of days of the year during of which the fresh food is supplied into cold store, B—rate of food's yearly turnover in cold store, assumed B = 5-6, 1/year [12], m—rate of irregularity of daily supply of food, assumed m = 1.5-2.5.

By the help of quantity of daily supplied food into cold store $G_{f.spp}$ = 4,475.5 ton, by Eq. (12), the tonnage M, ton of the cold store is calculated:

$$M = \frac{4,475.5 \text{ ton/day} \times 305 \text{ day}}{6 \times 2.5} = 91,000 \text{ ton}$$

8. Method for Determining of Cold Store's Constructive Characteristics

The value of heat gains $Q_{h.g.}$ (kW) through all external constructions of the cold store was quoted above $Q_{h.g.} = 0.35Q_{av.}$ = 0.35 × 5,175 kW = 1,811 kW, therefore, the external constructions of the cold store ought to be designed in such a way for not to exceed the quoted value $Q_{h.g.}$ = 1,811 kW.

For designing of cold store's building construction, materials and their thermo-physical properties should be chosen. For providing required limit of heat gains, the average heat transfer coefficient k_{const} (W/(m^2·°C)) of walls and ceiling of cold store should be calculated by using Eq. (13):

$$k_{const.} = \frac{0.3Q_{c.st}}{\left[\left(F_{s.w} + F_{ceil.}\right)\left(t_R - t_{c.st}\right) + \Sigma F_{oth.w}\left(t_{out} - t_{c.st}\right)\right]} \quad (13)$$

where, $F_{s.w}$—surface of south facing wall of cold store (m^2), $F_{ceil.}$—surface of ceiling of cold store (m^2), $\Sigma F_{oth.w}$—total surface of all other orientations facing walls (m^2), t_R—solar radiation conditional temperature of the boundary air layer on external surfaces of south facing wall and ceiling (°C), t_{out}—design temperature of outside air (°C), $t_{c.st}$—inside temperature of cold store (°C).

The value of solar radiation conditional temperature t_R is determined by Eq. (14) [13, 14]:

$$\mathrm{t_R} = t_{out} + \frac{I \cdot p}{\alpha_{\mathrm{out}}} \quad (14)$$

where, I—solar radiation intensity descending on surfaces of south facing wall and ceiling (W/m^2).

It is preferable to design single floor cold store. The constructive characteristics of the cold store can be determined based on its tonnage M. Thus, loaded volume V_{ld} (m^3) of cold store can be determined by the following ratio:

$$V_{ld} = M / m_{ld} \quad (15)$$

where, m_{ld} = 0.35 ton/m^3—norm of loading in 1 m^3 of cold store volume [12].

The loaded surface S_{ld} (m^2) of cold store is determined by the following ratio:

$$S_{ld} = V_{ld} / h_{ld} \quad (16)$$

where, h_{ld}—loaded height of single-storey cold storage which, according to Ref. [12], should be taken 4 m.

The cold store's real height $h_{const.}$ (m) is determined by the following sum:

$$h_{\mathrm{const.}} = h_{ld} + \left(0.3\text{-}0.5\right) \quad (17)$$

Real surface $S_{const.}$ (m^2) of cold store is to be determined by the following ratio:

$$S_{const.} = S_{ld} / \beta_S \quad (18)$$

where, β_S = 0.8—coefficient for increasing the surface for arranging of aisles in cold store.

The constructional sizes: length a (m) and width b (m) are determined, assuming square view in plan of the cold store (for reducing heat gains) in the following way:

$$a = b = \sqrt{S_{cold.st.}} \quad (19)$$

9. Conclusions

Replacement of throttling valve of conventional gas distribution station by adiabatic turbo-expander makes possible to generate large quantities of electric energy without consumption of fossil fuel.

As a result of adiabatic expansion, the gas is cooled up to -110 °C, which is not allowed to supplying into

gas distribution network. In order to escape this flaw, the gas of transportation main pipeline before expansion in turbo-expander should be primary preheated up to 105 °C, which, after expansion in turbo-expander, is cooled up to -25 °C.

A cold store in the proximity of gas distribution station has to be constructed for using the cooled gas as a cooling agent. For avoiding freezing of stored goods, the temperature of gas at the outlet of turbo-expander should not be lower than -25 °C.

Supply of used cold gas from cold store's heat exchanger into the urban gas distribution network, requires secondary heating of gas from -23 °C to +5 °C which helps preserving the gas network from damages.

The modification of widely applied gas distribution stations to electric power plant and cold store, allows producing large quantities of electricity and to set up an extremely large cold.

Because of very little quantity of fuel-gas consumed by gas heaters the annual operational cost of suggested technology is little too.

The suggested method for reversal design of the cold store can be applied in other heating and cooling technologies.

References

[1] Owen, S. M. 2013. "Thermophysical Properties of Refrigerants (Methane R-50)." In *ASHRAE Handbook Fundamentals.* Vol. 30. Atlanta, GA: ASHRAE, 45-7.

[2] Owen, S. M. 2013. "Thermodynamics and Refrigeration Cycles." In *ASHRAE Handbook Fundamentals.* Vol. 2. Atlanta, GA: ASHRAE, 22.

[3] Mokhatab, S., Poe, W. A., and Speight, J. G. 2006. *Natural Gas Transmission and Processing.* USA: ELSEVIER, 672.

[4] Kolpakowa, N. W. 2014. *Gas Distribution.* Ekaterinburg: Ural Universiteta, 200.

[5] Owen, S. M. 2006. "Forced Circulation Air Cooler." In *ASHRAE Handbook Refrigeration.* Vol. 42. Atlanta, GA: ASHRAE, 6.

[6] Poling, B. E., Prausnitz, J. M., and O'Connel, J. P. 2001. *The Properties of Gases and Liquids.* New-York, Chicago: The McGraw-Hill, 803.

[7] Jila, W. A., Ushakov, M. A., and Brukhanov, O. N. 2003. *Gas Supply Networks and Installations.* Moscow: Academia, 225.

[8] Tarik, A. S. 2010. *Engineering Thermodynamics.* UK: Ventus Publishing ApS, 107.

[9] Pavlov, K. F., Romankov, P. G., and Noskov A. A. 2007. *Examples and Problems on Course of Processes and Apparatus of Chemical Technology.* Saint Petersburg: Chemist, 624.

[10] Fraser, T. W., Skaja, R. A., and Wagner, J. N. 2008. *Mass and Heat Transfer.* New York: Cambridge University Press, 405.

[11] Owen, S. M. 2006. "Thermal Properties of Food." In *ASHRAE Handbook Refrigeration.* Vol. 9. Atlanta, GA: ASHRAE, 10.

[12] Kurilev, E. S., and Gerassimov, N. A. 1971. *Cold Stores.* Leningrad: Machinostroenie, 256.

[13] Melikyan, Z. 2014. "Heating and Cooling Hybrid System and Method for Its Calculation and Design." *International Journal of Energy and Power Engineering* 3 (6): 296-307.

[14] Melikyan, Z. 2015. "Energy Efficiency and Cost Effectiveness of Solar Water Heaters." *International Journal of Energy and Power Engineering* 4 (3): 184-8.

Journal of Energy and Power Engineering 9 (2015) 860-865
doi: 10.17265/1934-8975/2015.010.004

Innovative Approach to Increase Name Plate Capacity of Oil and Gas Gathering Centre

Chirag Parikh, Abdulaziz Al-Saeed, Bader Mahmoud and Rajiv Kukreja
Production Operations (North Kuwait) Team, Kuwait Oil Company, Ahmadi 61008, Kuwait

Received: June 08, 2015 / Accepted: August 03, 2015 / Published: October 31, 2015.

Abstract: Purpose: The oil and gas gathering and processing facility of Kuwait Oil Company is built with a nameplate capacity of X MBOPD (thousand barrels oil per day) with 50% water cut. However, the facility was operating with a water cut of 35%. This comprehensive technical study was conducted to evaluate possibility of increasing oil processing capacity of this facility in line with current lower water cut and other operational flexibilities available in the facility without utilizing its design margin. Topic: This paper shares an innovative approach to increase name plate capacity of oil and gas processing facility utilizing available operational flexibility and operational margins with minor modification. It shares a case study where facility capacity is increased by around 19% without utilizing design margins of equipment or pipeline. Method: The study includes theoretical verification and analysis of all major equipment and piping to identify available capacity and limitation, in order to utilize available additional margin and to propose debottleneck options to overcome limitations. Achievement: The study confirmed that, facility name plate capacity can be revised from X MBOPD (with 50% w.c (water cut)) to X + 32 MBOPD (with: 45% w.c) minor modification in separator and utilizing margin available in feed specification of desalter trains.

Key words: Debottlenecking, capacity enhancement, production.

1. Introduction

The design philosophy adopted for oil and gas facility is different than philosophy of a typical plant of refinery or a petrochemical complex. Unlike these units, oil and gas facility is always subjected to change in feed stream in terms of physical/chemical properties, water cut, GOR (gas oil ratio) etc. This unique characteristic of changing feed stream requires designer to ensure provision of adequate flexibility in design of oil and gas facility for forecasted changes of feed stream. However, it is observed that, such flexibilities are not utilized during initial years of operation of facility when the feed has not changed from its original specification especially in terms of water cut. The innovative approach adopted at Kuwait Oil Company to increase nameplate capacity of oil and gas gathering and processing center utilizes this available operational flexibility and additional margin of facility. However, it is ensured that, no design margin of equipment or piping is utilized in order to increase processing capacity of facility.

Corresponding author: Chirag Parikh, specialist, research field: process engineering. E-mail: CParikh@kockw.com, chirag.a.parikh@gmail.com.

2. Methodology

The methodology adopted for this systematic evaluation of facility to implement this innovative approach is listed below [1]:

(1) Review current oil and water potential of facility and compare it with forecasted figures;

(2) Review design capacity of each equipment of facility to identify its processing capacity and limitations;

(3) Identify equipment or piping with limitations for increase in processing capacity;

(4) Evaluate possible modifications to overcome limitations of these equipment or piping;

(5) Re-evaluate equipment for increase in processing capacity after possible modification;

(6) Establish a revised processing capacity of facility based on proposed process or operational modifications;

(7) Implement modifications once the viability is confirmed;

(8) Carry out separate performance testing of each equipment at higher established capacity;

(9) Carry out performance testing of complete gathering center and revise the name plate capacity.

2.1 Review Current Oil and Water Potential of Facility and Compare It with Forecasted Figures

The water cut of feed stream plays a vital role in this innovative approach. The water cut is the main parameter which changes significantly over years. Due to this, the facilities are always designed considering expected future water cut to be realized during life of facility or till new facility expansion is planned. This innovative approach makes use of the additional margin available to handle this water till actually realized.

In our case, the review of current and forecasted values of water cut revealed that, facility currently operates at much lower water cut than what is anticipated in future. Moreover, it was also noticed that, expected higher water cut will be realized after no. of years. This information played a vital role in deciding a way forward for utilization of available margin of water handling, for increasing crude oil processing.

2.2 Review Design Capacity of Each Equipment of Facility to Identify Its Processing Capacity and Limitations

The next step is to review design capacity of each equipment of facility, after establishing significant gap in current water cut and expected future water cut and the duration in realizing this water cut. The step is to evaluate processing capacity of each equipment for possible increase of oil processing, utilizing margin available due to lower water cut than design. All major equipment e.g., headers, separators, tanks, heaters, desalters, pumps, control valves, etc. are checked for possible increase in oil processing capacity utilizing available margin due to lower water cut. It required to review all relevant datasheets, P & IDs (process & instrument diagrams), current operating trends, design basis, etc. to identify design capacity of major equipment and pipelines. It may be required to carry out simulation of segments of facilities to get better understanding of capacity (e.g., common headers, piping etc.). Each equipment shall be evaluated for its processing or handling capacity of all the fluids, i.e., crude oil, water, gas and condensate as applicable and shall be tabulated for better analysis. Below is simplified table for LP (low pressure) separator developed during this analysis.

2.2.1 Separation Trains

The facility is equipped with three low pressure separation trains. The gas separated from separators is further handled in accumulator. Below Table 1 shows capacities of each main component of separation train.

It is required to develop similar tables for all equipment and piping of facility and carry out analysis for each of these equipment to understand the limitations and capabilities. Based on this, we need to identify most limiting units of facility which restricts the facility operation at higher capacity. During this evaluation, it was observed that, all equipments and piping have potential to increase oil processing capacity from current level of X MBOPD (thousand barrels oil per day) with 50% water cut to X + 32 MBOPD with 45% water cut or even more. However, the limitation was observed in oil and gas separator and desalter units which were limiting oil processing capacity to X MBOPD [2-8].

2.3 Identify Equipment or Piping with Limitations for Increase of Processing Capacity

Once design capacities for oil, water and gas are tabulated for all equipment and piping, it required to start evaluation in detail. All the equipments and

Table 1 Capacity of main components of oil and gas processing facility.

System	Equipment	Oil, MBOPD	Water, MBWPD	Gas, MMSCFD
Capacity for one separation train (three phase mode)				
Separator	LP separator	A	C	E
Control valves	Crude oil LCV	B	-	-
	Water LDVC	-	D	-
	Gas export PCV Flare PCV	-	-	F F
One separation train	Max. operating capacity of one separator train	A	C	F
Capacity of gas handling units D/S of separator				
LP gas accumulator	C-1202 A & B	-	-	G
Export pipeline	LP gas export pipeline	-	-	H
Three separation train	Max. operating capacity of three separator trains (in three phase mode)	A + A + A (limited by oil separation capacity of Sep.)	C + C + C (limited by water separation capacity of Sep.)	H (limited by LP gas export pipeline)

MBWPD—thousand barrels water per day, MMSCFD—million standard cubic feet per day.

piping which are designed to handle more oil, water and gas than overall capacity of facility shall be identified and extra margin available in each of these equipment, shall be tabulated separately. All the equipments which limit the processing or handling capacity of oil, water and gas with respect to current water cut or expected future water cut shall be identified and tabulated separately. During our study, we have identified that, LP separator and desalter are main equipments which restrict the overall processing capacity of facility. The observed limitation in these equipments is explained below.

2.3.1 Oil and Gas Separator

All LP separators in current configuration are designed for operation in three phase mode to process around X MBOPD with 50% water cut. However, these separators are currently operated in two-phase mode with water cut of around 35%. This has increased overall processing load on oil withdrawal piping and control valves of separators, as both oil and water are withdrawn from oil withdrawal piping in two phase mode of operation. Moreover, it was not possible to operate this separator in three-phase mode due to certain operational limitations. So, it was decided to identify a suitable modification to overcome this limitation [2-4, 7, 8].

2.3.2 Desalter

The desalter has design capacity to process oil X + 13 MBOPD with 10% water in feed stream. As our objective was to maximize processing capacity of desalter, which is most vital unit and controlling factor of facility for increasing processing capacity, so, it was decided to identify suitable option to further increase desalting capacity of this facility [5, 6, 8].

2.4 Evaluate Possible Modifications to Overcome These Bottlenecks of These Equipment or Piping

2.4.1 Oil and Gas Separator

It was decided to modify the control loop for liquid level and interface level of separator. The current configuration of interface level control by LDIT/LDCV (level differential indicator and transmitter/level differential control valve) (installed on water outlet line) and liquid level control by LIT/LCV (level indicator and transmitter/level control valve) (installed on oil outlet line) was modified. As per new modification, both LDCV and LCV were controlled by LIT (liquid level). This facilitated two-phase operation of separator with both oil and water outlet lines, in operation which subsequently increased liquid handling capacity of separator which was previously limited as all liquid, was withdrawn

only from oil outlet line. There was a design flexibility available in this separator to divert liquid withdrawn from water outlet line either to effluent water tank or to wet crude oil tank. This flexibility allowed two-phase operation of separator with liquid withdrawn from both oil and water outlet lines. Below is simplified Table 2 developed for design capacity of separator trains to evaluate possible increase in capacity after proposed modification [2, 7, 8].

2.4.2 Desalter

The operational and quality parameters were checked to identify scope of increasing processing capacity of desalter. It was observed that, feed stream of desalter was containing around 0.5% water cut due to significantly higher residence time in wet tanks. Whereas, the desalter was designed to handle 10% water cut in feed stream. It was decided to utilize this additional margin to increase oil processing capacity of desalter. Below is a simplified table showing analysis of desalter system based on operation with 0.5% water in feed stream instead of 10% [5, 6, 8].

2.5 Re-evaluate Equipment for Increase in Processing Capacity after Possible Modification

After completing above mentioned steps, we need to reevaluate the capacity of these equipments to finalize revised capacity w.r.t water cut as tabulated in Table 3. Any limitation in gas handling capacity shall also be considered, if applicable, to finalize overall crude oil handling capacity.

2.5.1 Oil and Gas Separator

The processing capacity of oil and gas separator was reevaluated with this proposed modification of utilization of both oil and water outlet lines for liquid withdrawn in two phase operation. It was evident that, processing capacity of X + 32 MBOPD with 45% water cut can be achieved by these separators after this modification. The water handling capacity is limited to 45% due to utilization of some of the water handling capacity by oil and further limitation from wet tank filling line.

2.5.2 Desalter

The re-evaluation of processing capacity of desalter has confirmed that, utilization of available margin in water cut of feed stream, which is designed for 10% but realized as 0.5%, will increase processing capacity of desalter to X + 32 MBOPD. This reevaluation shall be carried out after detailed technical verification of system followed by no. test runs. We generally depend upon the historical operating data and laboratory analysis data for such evaluation. We can conclude that, water cut will not increase more than 0.5% based on historic data but care shall be taken because any increase of water cut above 0.5% will directly affect the crude oil export quality as desalter

Table 2 Revised capacities for LP separator trains (for two phase operation post modification).

System	Equipment	Oil, MBOPD	Water, MBWPD	Gas, MMSCFD
Capacity for one separation train (two phase mode)				
Separator	LP separator	A	C	E
Control valves	Crude oil LCV	B	-	-
	Gas export PCV Flare PCV	-	-	F F
One separation train	Max. operating capacity of one separator train	A	C	F
Capacity of gas handling units D/S of separator				
LP gas accumulator	C-1202 A & B	-	-	G
Export pipeline	LP gas export pipeline	-	-	H
Three separation train	Max. operating capacity of three separator trains (in two phase mode)	A + A + A + 32 or X + 32 (limited by desalter capacity of Sep.)	C + C + C (limited by water separation capacity of Sep.)	H (limited by LP gas export pipeline)

Table 3 Review of current capacities.

System	Equipment	Normal flow, MBOPD	Remarks
Heater	Four no. of heaters	X + 37	
Desalter	Two no. of desalters	X + 15 (if feed water cut is 10%)	If the feed water cut to desalter is 10% then overall capacity of desalter will remain limited to X + 15 MBOPD
		X + 32 (if feed water cut is 0.5%)	However, as the current w.c. is around 0.5%, the effective desalter capacity will increase to X + 32 MBOPD utilizing extra margin available for water
Desalter back pressure control valve	Two no. of PCVs for two trains	X + 63	

shall be operating at its max. handling capacity utilizing extra margin available for water processing. It may be possible to take a conservative approach of considering 1% water cut in feed stream instead of 0.5% to give some margin for unexpected operational disturbances in the facility [1].

2.6 Establish a Revised Processing Capacity of Facility Based on Proposed Process or Operational Modifications

The whole facility was reevaluated for revised processing capacity based on proposed modifications. During this step, most limiting figures of oil, water and gas are considered for the equipment which will define the overall capacity of facility. It was established that, whole facility is capable to process X + 32 MBOPD oil with 45% water cut and with GOR of 600. All equipments are capable to process even more oil and water, but the limitation of X + 32 MBOPD is based on max. possible processing capacity of desalter and limitation 45% water cut is from separation capacity of oil and gas separator/wet tank. The limitation for gas handling capacity is based on limitation of gas export pipeline [1].

2.7 Implement Modifications Once the Viability Is Confirmed

The main modification of change in control loop of separator was implemented after complying company procedure of management of change. The formal study was conducted to evaluate any adverse impact on separation operation due to this modification. The study and review was jointly conducted by engineers from production operations team, technical services team, maintenance team and health, safety & environment team. The change was mainly related to logic configuration change on DCS (distributed control system) so there was no major cost or time impact due to this physical change.

There was no physical change in desalter unit, so it was decided to test desalter at higher capacity during performance test. The actual test was critical for desalter to ensure actual capability of these units to handle higher crude oil flow and also to ensure all quality parameters of salt in crude oil and BS & W (base sediments & water) are met.

2.8 Carry out Separate Performance Testing of Each Equipment at Higher Established Capacity

The next step is to verify findings of study by conducting actual field tests. It is recommended to carry out performance tests of each equipment in isolation to ensure each of these equipment is capable of processing higher flow of oil, water and gas. This will also eliminate the risk of any major problem in facility, if a limitation is faced during testing, as only one or two equipments will be processing higher flow rates of fluid. It is required to record all performance parameters while testing to ensure smooth operation of equipment within operating envelop meeting all quality requirements. It shall be ensured that, no design margin of any equipment or piping is utilized during performance testing. The testing shall be started only after proper planning is done and required coordination between all concerned teams is established.

2.9 Carry out Performance Testing of Complete Gathering Center and Revise the Name Plate Capacity

The complete testing of whole facility will start once individual testing of each equipment is successfully completed, and the results show no limitation in any of the equipment or piping. If the results show any limitation during testing of individual equipment, then the study report shall be revisited for necessary amendments based on actual observations made during testing. It will also require to identify the bottleneck area in the system which was not identified during study phase. A detailed analysis is required to be conducted to find any option to eliminate this bottleneck. The option shall be implemented and again performance testing shall be carried out. If we cannot find any option to eliminate bottleneck then the capacity of this equipment and whole facility shall be revised for new figures. In brief, all steps from step B to step H shall be carried out again.

In our case, the whole facility shall be tested at required production level (e.g., X + 32 MBOPD) to confirm capability of complete facility to process X + 32 MBOPD with 45% water cut. It is also required to record all performance parameters while testing to ensure smooth operation of facility within operating envelop meeting all quality requirements. The name plate capacity can be revised after successful completion of testing of whole facility.

3. Conclusions

It is concluded that, most of the oil and gas facilities have potential to increase its name plate capacity (without utilizing design margin) in the early years of facility operation, when the forecasted figures of higher water cut, etc. are not realized, by implementing minor modifications and utilizing operational flexibilities available in the facility. Such innovative approach will result in significant financial/production gains for any organization.

Acknowledgments

We are thankful to Mr. Emad Sultan—Dy. CEO (NK), Mr. Adnan-Al Adwani—Manager Operations Group (NK), Mr. Abdulla Al-Harbi—Manager Operations Support Group (NK) of Kuwait Oil Company for their continuous support and encouragement in carrying out this technical study.

References

[1] Bhatt, B. I., and Vora. S. M. 1984. *Stoichiometry.* New Delhi: TATA McGraw-Hill.

[2] GC-24 ERB (Engineering Record Book). 2011. “Data Sheet LP Wet Separator (Doc. No.32757-024-RA-E-1219).” Kuwait Oil Company.

[3] GC-24 ERB. 2011. “Data Sheet Dual Tank Storage Tank (Doc. No.32757-024-RA-E-1901).” Kuwait Oil Company.

[4] GC-24 ERB. 2011. “Data Sheet Wet Tank Storage Tank (Doc. No.32757-024-RA-E-1902).” Kuwait Oil Company.

[5] GC-24 ERB. 2011. “Data Sheet Heater (Doc. No.32757-024-PA-E-1401).” Kuwait Oil Company.

[6] GC-24 ERB. 2011. “Data Sheet Desalter (Doc. No.32757-024-RA-E-1223).” Kuwait Oil Company.

[7] GC-24 ERB. 2011. “Data Sheet for PCVs.” Kuwait Oil Company.

[8] GC-24 ERB. 2011. “Data Sheet for LCVs.” Kuwait Oil Company.

Journal of Energy and Power Engineering 9 (2015) 866-871
doi: 10.17265/1934-8975/2015.010.005

Effect of Additives on the Performance of Lead Acid Batteries

Lankipalli Rekha, Manne Venkateswarlu, Kurivella Suryanarayana Murthy and Mandava Jagadish
Research & Development, Technology, Amara Raja Batteries Ltd., Andhra Pradesh 517 520, India

Received: June 18, 2015 / Accepted: August 03, 2015 / Published: October 31, 2015.

Abstract: Effect of titanium dioxide (TiO_2) and carbon additives in the respective positive and negative material properties and the influence on the performance of the battery were investigated. The electrode samples were characterized by BET (Brunauer Emmett Teller), XRD (X-ray diffractometer), SEM (scanning electron microscopy) and EIS (electrochemical impedance spectroscopy) to understand the surface area, phase, structure, morphology and electrical conductivity of the respective electrode material. The surface area was obtained as 2.312 $m^2 \cdot g^{-1}$ and 0.892 $m^2 \cdot g^{-1}$, respectively for 12% of activated carbon in the expander of negative and 0.70% of TiO_2 (Titanium dioxide) in the PAM (positive active material). The structural analysis reveals an increase in the tetrabasic lead sulfate and also evidenced by well grown crystals in the PAM with the TiO_2, respectively obtained by XRD and SEM techniques. The impedance spectra analysis shows an increase of electrical conductivity of negative active mass with temperature. The battery results showing two fold enhancements in the charge acceptance were attributed to the high surface area activated carbon in the NAM (negative active material). The materials properties of electrodes and their influence on the battery performance were discussed.

Key words: Titanium dioxide, carbons, charge acceptance, lead acid battery.

1. Introduction

Lead acid batteries are the most versatile and reliable power source for cranking applications. These batteries are remaining as central electric power for starter and also ideal stop starts due to its safety and economy. For high voltage and power, assist functions of hybrid electric vehicle require high power storage systems to sustain repeated charge and discharge reactions even at high rate discharge or under the PSoC (partial state of charge) [1-3]. The present performances of lead acid batteries are not adequate for emerging applications. Therefore, research attention has been focused on to improve the specific energy, charge acceptance, rate capability and cycle life of the VRLA (valve regulated lead acid) battery.

The lower specific energy is one of the major limitations of lead acid battery mainly due to poor PAM (utilization of the positive active material) and also high atomic weight of the lead [4]. Several studies have been carried out on the positive active material by reducing the weight or improving the adhesive properties and or exploring intelligent additive, nanowires, etc., for better utilization of the positive active material [4-7]. Similarly, efforts were also made to improve charge acceptance and cycle life of battery by eliminating sulfation in the negative electrode. The progressive accumulations of sulfation with cycling may shorten the life or fail the battery. Nakamura, et al. [8] had successfully achieved in eliminating the sulfation in the negative by increasing the carbon content which further enhanced the life of the battery. The carbon of different grades is obviously an additive in the negative and was found to have beneficial effects on the material properties [9-18]. Some of these benefits are: improving conductivity of active mass, facilitating the formation of small isolated lead sulfate crystals, impeding the reaction of hydrogen evolution, and also acting as an electro-osmotic pump to diffuse acid into

Corresponding author: Manne Venkateswarlu, Ph.D., AGM (assistant general manager), research fields: electrodes and electrolytes materials, rechargeable batteries and nanomaterial. E-mail: mvu@amararaja.co.in.

the negative electrode.

In this paper, an attempt has been made to develop battery with enhanced capacity, charge acceptance and life of the battery for emerging automobile applications. The titanium dioxide (TiO_2) and the carbon materials are selected as additives in the respective positive and negative electrodes and characterized. The effects of additive on the material properties and performance of batteries were studied.

2. Experiments

2.1 Preparation of Positive and Negative Electrodes

The positive active material was prepared by mixing up of lead oxide with different loading of *x*% TiO_2 (*x* = 0.35, 0.70 and 1.40). The DM (demineralized water) water and sulfuric acid were added to the dry mixture of active material under controlled temperature. Standard procedure was followed to obtain homogeneous paste of positive oxide. Similarly, the negative active material was prepared by mixing up of lead oxide with different grades of carbons (carbon black, black pearl and activated carbon). The loading of the carbon was 12% in the expander of negative electrode. The DM water and sulfuric acid content was added appropriately to the mixture and the standard procedure was followed to obtain homogeneous paste recipe of negative. The positive and negative oxide paste were applied on grids separately and then allowed to cure & dry under controlled temperature and humidity. The resultant electrodes were characterized and also used for assembling VRLA battery.

2.2 Characterization of Electrode Materials

The cured electrode materials were analyzed by chemical method to estimate the free lead, lead oxide and lead sulfate content. The surface area of the different grades of carbon powders and modified electrodes was estimated by the BET (brunauer emmett teller) method (Coulter SA3100). The structural studies were carried out by XRD (X-ray diffractometer) (PANalytical). The XRD spectra were recorded with CuKα radiation (1.5418 Å) in the 2θ range from 10° to 80° and analyzed by X'pert software.

The morphology of the electrodes was mapped by SEM-EDS (scanning electron microscopy coupled with energy dispersive spectroscopy) (HitachiS-3400N). SEM images and SEM-EDS spectra were recorded and mapped to understand the morphology of the crystals and elemental distribution in the respective electrodes. The EIS (electrochemical impedance spectroscopy) (novo-control) was used to evaluate the electrical conductivity of the electrode and data were analyzed by WinFIT software.

2.3 Design and Testing of Batteries

The VRLA battery configuration with rating of 5 Ah was selected for testing. The VRLA battery made up of modified positive and modified negative electrodes were coupled with regular negative and regular positive electrodes, respectively. The AGM (adsorbed glass mat) was used as separator to complete the VRLA design. The aqueous sulfuric acid with standard specific gravity was used as electrolyte. The electrical tests were carried out using LCN (life cycle network) circuits (Bitrode) and multi-functional electrochemical analyzer (Wonatech). The batteries were tested as per applicable JIS (Japanese Industrial Standard).

3. Results and Discussion

3.1 Chemical Analysis and Surface Area Studies

The cured electrode materials consist of several lead compounds such as free lead, oxides, sulfates, etc. The PAM (positive active material) that consists of *x*% of TiO_2 was analyzed by chemical method to ensure that, the free lead, sulfate and density contents were within the specification. The surface area of PAM with *x* = 0.70% of TiO_2 was 0.892 $m^2 \cdot g^{-1}$ [16].

The chemical analysis was also carried on the NAM (negative active material) samples consisting different grades of carbon. The lab results were found to be within the specification. The surface area analysis was

carried out on the carbon materials as well as NAM with different carbons. The surface area of carbon black, black pearls and activated carbon was found, respectively 82 $m^2 \cdot g^{-1}$, 1,450 $m^2 \cdot g^{-1}$ and 1,950 $m^2 \cdot g^{-1}$. The highest surface area of the NAM with activated carbon was found as 2.138 $m^2 \cdot g^{-1}$.

3.2 Structural and Morphology Studies

During curing, electrodes undergo chemical reactions to convert the free lead into the basics sulfates of different forms such as mono, tri and tetra basic. The formations of tri and tetra basic sulfate in the positive electrode would be beneficial effect on the capacity and life of the battery, respectively. The XRD spectra were recorded for all cured positive electrodes consisting of *x*% of the TiO_2 (x = 0.35, 0.70 and 1.40) and observed XRD profiles are shown in Fig. 1.

The lead, lead oxide, lead dioxide and tribasic lead sulfates (3BS) and tetrabasic lead sulfate (4BS) were calculated quantitatively by matching the observed spectral data with selected JCPDS (joint committee on powder diffraction standard) data. The selected JCPDS data are: 01-087-0663 (Pb), 01-078-1666 (PbO), 01-072-2102 (PbO_2), 01-088-0552 (3BS) and 00-023-0333 (4BS). The concentration of 4BS was 34%, 51% and 49%, respectively obtained in the positive electrode consisting 0.35%, 0.70% and 1.40% of TiO_2. The 4BS was found appreciably higher which was obtained at higher temperature and humidity [11, 12]. The presence of 4BS in the positive electrode enhances the strength of electrode by interconnected structure and also porosity in the positive electrode [12]. The presence of 4BS in the PAM which enhance the cycle life of the battery may be due to improved structure stability and also better access of the acid throughout the electrode. Further, the crystallite size was calculated using Scherer's formula and was found as 25.70, 40.53 and 33.47 nm, respectively for 0.35%, 0.70% and 1.40% of TiO_2 in the PAM. The larger crystals have smaller surface area and vice versa. The crystals are larger for the x = 0.70% of TiO_2 in PAM due to high concentration 4BS which is expected to be lower surface area, as evidenced by surface area analysis. The surface area of PAM was found to be relatively lower as compared to NAM. The present XRD and BET results are complementary to each other. The structure of the electrode plays a significant role in enhancing the cycle life of the battery for repeated cycling.

The electrode structure build with well-defined crystals, optima size and shape and uniform distribution of elements are desired ways to improve the material properties of battery. The SEM images for different *x*% of TiO_2 in the PAM were recorded and the typical SEM image of the positive electrode with 0.70% of TiO_2 in PAM was shown as inset in Fig. 2.

The SEM images were found larger crystals and results are consistent with structural analysis by XRD where the structure consists of predominately 4BS. Further, SEM-EDS mapping was carried out to understand the distribution of the elements in the respective electrodes. The SEM-EDS mapping for PAM with 0.70% of TiO_2 is shown in Fig. 2. It clearly shows the presence of titanium and its distribution throughout the electrode.

The SEM images on the NAM were also analyzed and typical SEM image of activated carbon in the

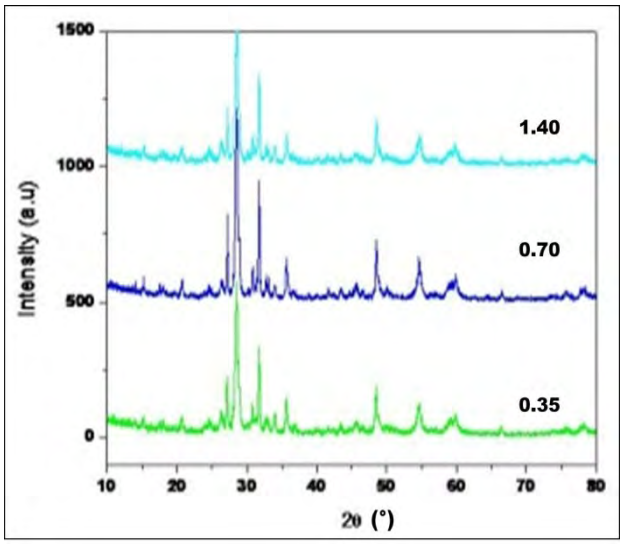

Fig. 1 The XRD spectra of the positive electrode with *x*% of TiO_2.

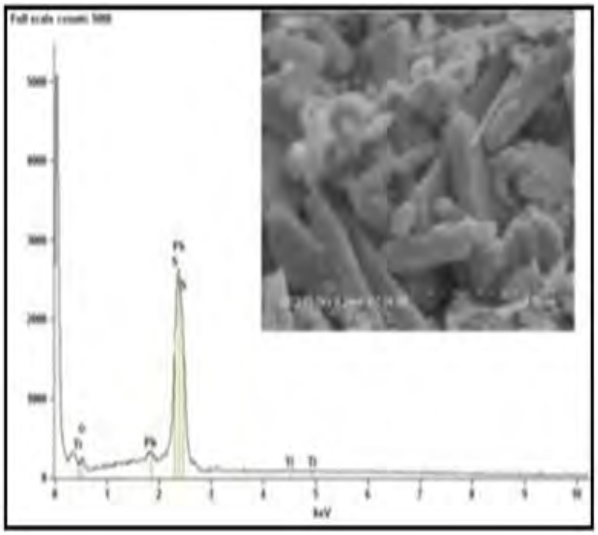

Fig. 2 The SEM-EDS spectral mapping of the PAM with 0.70% of TiO_2 (inset figure is the SEM image).

expander of negative is shown as inset in Fig. 3. The SEM image shows the well-defined crystals with much smaller in size and shape. The smaller crystals have larger surface area and vice versa. The improved material properties were attributed to the presence of high surface area (1,950 $m^2 \cdot g^{-1}$) activated carbon in NAM which controls the sulfate crystals. The SEM-EDS spectral mapping of the NAM with activated carbon is shown in Fig. 3. The SEM-EDS spectral analysis confirms the presence of the carbon in the NAM and also uniform distribution throughout the NAM electrode [15, 16].

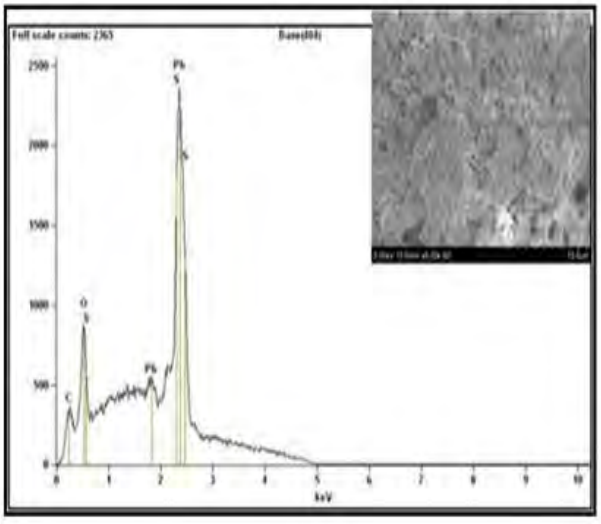

Fig. 3 The SEM-EDS spectral mapping of the NAM with activated carbon (inset figure is the SEM image).

3.3 Impedance Spectroscopy Studies

The EIS is very informative tool to understand the physical parameters of the materials. The EIS studies have been carried out on the NAM with activated carbon at ambient and also at different temperatures. The impedance spectra of NAM consisting activated carbon at different temperatures are shown in Fig. 4.

Fig. 4 clearly shows the formation of semi-circle on the NAM within the temperature range. It is worth to mention that, the semi-circle of active mass changes with temperature indicates decreasing the bulk resistance (R_b) of the NAM with temperature. In other words, the electrical conductivity of the active mass increases with temperature and was attributed to the presence of activated carbon in the NAM.

3.3 Battery Studies

The influence of the positive active material properties on the battery was studied on VRLA battery with modified positive (with TiO_2) electrode and regular negative electrode. The AGM separator was used to separate the electrodes and also avoid internal shorting. The aqueous sulfuric acid with standard specific gravity was used as electrolyte. The battery parameters such as capacity, HRD (high rate discharge) and CA (charge acceptance) were evaluated as per JIS standard [16]. The electrical performance of the batteries

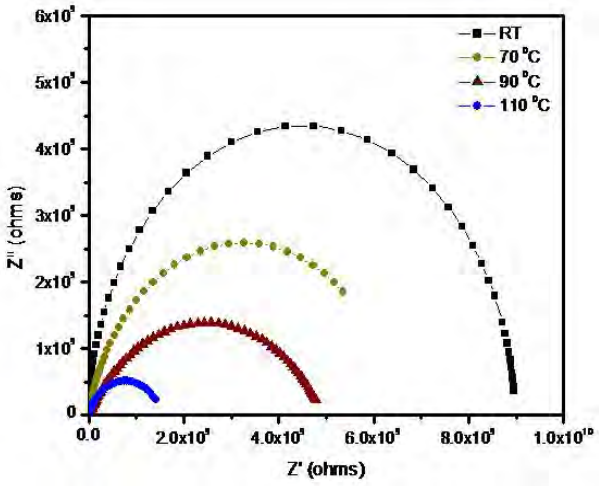

Fig. 4 Impedance spectra of the NAM with activated carbon.

consisting *x*% of TiO_2 in PAM is shown in Fig. 5.

Fig. 5 shows the significant improvement in the charge acceptance of the battery of the PAM with *x*% of TiO_2. Further, the capacity of the battery meets the standard but was found lower values in case of HRD may be due to surface area and electrical properties of the positive active materials.

In order to understand the role of different grade carbon in the expander of negative electrode, the VRLA battery with modified negative (carbon) and regular positive and electrodes were wrapped with AGM separator and aqueous sulfuric acid was used as electrolyte. The battery parameters such as capacity, HRD and CA of the battery were evaluated as per the JIS standard. The electrical performance of the battery with different grades of carbons in NAM is shown in Fig. 6.

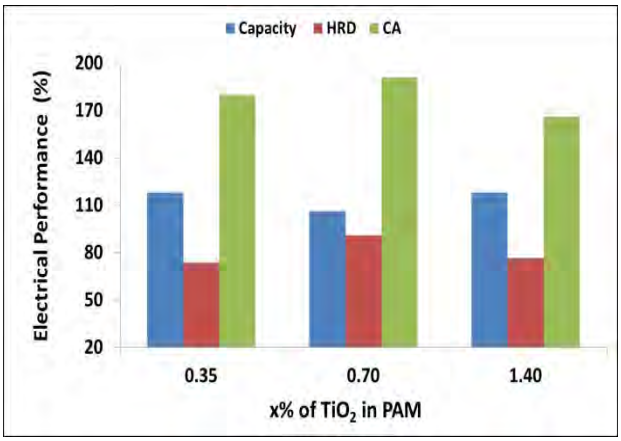

Fig. 5 The electrical performance of battery consisting *x*% of TiO_2 in PAM.

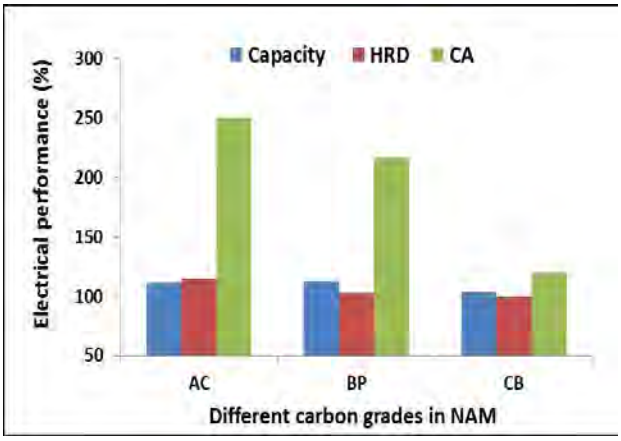

Fig. 6 The electrical performance of battery with different grades of carbon in NAM.

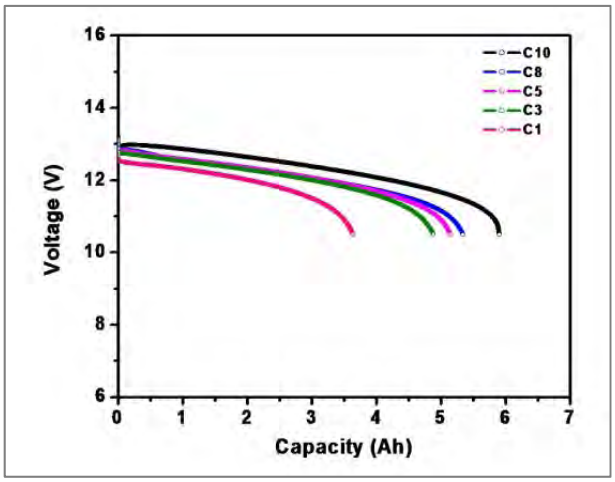

Fig. 7 Discharge profile of the battery at different C-rates.

From Fig. 6, it is confirmed that, the capacity and HRD results were found to be marginal whereas significant improvement, by two fold, of charging acceptance of the negative. The two fold enhancement was attributed to the presence of high surface area (1,950 $m^2 \cdot g^{-1}$) activated carbon improves the material properties of the active mass and also alleviate the sulfation. Therefore, the battery consists of negative active material blended with activated carbon can deliver high energy and power and expected to meet the electric power requirement for emerging automobiles.

Further, these batteries were evaluated at different loads at lab scale to understand the rate capability of batteries. The rate capability of the batteries could be achieved either by reducing the thickness of the electrodes or conductive additives in the electrodes. These batteries with negative consists of activated carbon were tested at different C-rates. The typical discharge profiles of the batteries are shown in Fig. 7. The discharge capacities were obtained at 0.10 C and 1.0 C are 5.8 Ah and 3.5 Ah, respectively [16].

4. Conclusions

The presence of the titanium dioxide in the positive active material was found to be beneficial in enhancing the tetra basic lead sulfate which in turn enhances the life of the battery. The high surface area activated carbon in the negative electrode improves the capacity

and HRD marginal. Apart from enhanced electrical conductivity of the active mass, a profound impact was observed on the charge acceptance of the battery and was attributed to carbon in the negative electrode. It was concluded that, the selective grade of carbon in the negative electrode pronounced a beneficial effect on the performance of the lead acid batteries for emerging automobile applications.

Acknowledgments

Authors are grateful to the Management of Amara Raja Batteries Ltd., for their constant encouragement. Authors are grateful to Dr. Nallani Satyanarayana, Pondicherry University for extending the experimental support and data analysis.

References

[1] Mosley, P. T., Rand, D., and Monahov, B. 2012. "Designing Lead Acid Batteries to Meet Energy and Power Requirement of Future Automobiles." *J. Power Sources* 219 (December): 75.

[2] Karden, E., Shinn, P., Bostock, P., Cunningham, J., Schoultz, E., and Daniel, K. 2005. "Requirements for Future Automotive Batteries—A Snapshot." *J. Power Source* 144 (2): 505.

[3] Ebner, E., Burow, D., Panke, J., Borger, A., Feldhoff, A., Atanassova, P., Valenciano, J., Wark, M., and Ruhl, E. 2013. "Carbon Blacks for Lead Acid Batteries in Micro-Hybrid Applications—Studied by Transmission Electron Microscopy and Raman Spectroscopy." *J. Power Source* 222 (January): 554.

[4] Moncada, A., Mistretta, M. C., Randazzo, S., Piazza, S., Sunseri, C., and Inguanta, R. 2014. "High Performance of PbO_2 Nanowires Electrodes for Lead Acid Battery." *J. Power Sources* 256 (June): 72.

[5] Mcallister, S. D., Patankar, S. N., Cheng, I. F., and Edwards, D. B. 2009. "Lead Dioxide Coated Hollow Glass Microscopeheres as Conductive Additives for Lead Acid Batteries." *Scripta Materialia* 61 (4): 375.

[6] Ponraj, R., McAllister, S. D., Cheng, F., and Edwards, D. B. 2009. "Investigation on Electronically Conductive Additives to Improve Positive Active Materials Utilization in Lead Acid Batteries." *J. Power Sources* 189 (2): 1199.

[7] Moncada, A., Mistretta, M. C., Ranadzzo, S., Piazza, S., Sunsuri, C., and Ingnanta, R. 2014. "High-Performance of PbO_2 Nanowire Electrodes for Lead-Acid Battery." *J. Power Source* 256 (June): 71.

[8] Nakamura, K., Shiomi, M., Takahashi, K., and Tsubota, M. 1996. "Failure Modes of Valve-Regulated Lead/Acid Batteries." *J. Power Sources* 59 (1-2): 153.

[9] Shiomi, M., Funato, T., Nakamura, K., Takahashi, K., and Tsubota, M. 1997. "Effects of Carbon in Negative Plates on Cycle-Life Performance of Valve-Regulated Lead Acid Batteries." *J. Power Sources* 64 (1-2): 147.

[10] Kazawa, A., Kawamura, T., Sato, A., Sano, M., and Brold, D. 1998. "New Colloidal and Organic Carbon Additives for Lead Acid Batteries." In *Proceedings of the 13th Annual Battery Conference on the Applications & Advances (January)*, 353.

[11] Boden, D. P., Loosemore, D. V., Spence, M. A., and Wojcinski, T. D. 2010. "Optimization Studies of Carbon Additives to Negative Active Material for the Purpose of Extending the Life of VRLA Batteries in High Rate Partial State of Charge Operation." *J. Power Source* 195 (14): 4470.

[12] Krivik, P., Mica, K., Baca, P., Tonar, K., and Poser, P. 2012. "Effect of Additives on the Performance of Negative Lead Acid Battery Electrodes during Formation and Partial State of Charge Operation." *J. Power Sources* 209 (July): 15.

[13] Pavlov, D. P., and Niklov, P. N. 2002. "Lead Carbon Electrode with Inhibitor of Sulfation for Lead Acid Batteries Operation in HRPSoC Duty." *J. Electrochem. Soc.* 159 (8): A1215.

[14] Mosely, P. T., Nelson, P. F., and Hollenkamp, A. F. 2006. "The Role of Carbon in Value Regulated Battery Technology." *J. Power Sources* 157 (1): 3.

[15] Venkateswarlu, M. 2011. "Improvement of Lead Acid Battery Performance by Nano Carbon Materials." In *Proceedings of the 14th Asian Battery Conference (September)*, 24.

[16] Rekha, L., Venkateswarlu, M., Murthy, K. S. N., and Jagadish, M. 2014. "Influence of Carbon and TiO_2 Additives on the Performance of the Lead Acid Batteries." In *Proceedings of the 9th International Conference on Lead-Acid Batteries (June)*, 55.

[17] Sugumaran, N., Everill, P., Swogger, S. W., and Dubey, D. P. 2015. "Lead Acid Battery Performance and Cycle Life Increased through Addition of Discrete Carbon Nanotubes to Both Electrodes." *J. Power Sources* 279 (April): 281.

[18] Sarvanan, M., Ganesan, M., and Ambalvanan, S. 2014. "An in situ Generated Carbon as Integrated Conductive Additive for Hierarchical Negative Plate of Lead Acid Battery." *J. Power Source* 251 (April): 20.

Journal of Energy and Power Engineering 9 (2015) 872-885
doi: 10.17265/1934-8975/2015.010.006

Electric Energy Management Modeling for Kingdom of Bahrain

Isa Salman Qamber[1], Mohammed Yusuf Al-Hamad[2] and Abdul Majeed Habib Abdul Karim[3]

1. Department of Electrical & Electronics Engineering, University of Bahrain, Isa Town 33831, Kingdom of Bahrain

2. Client Interface Executive, Operations Directorate-Trade Section,GCC Interconnection Authority, Dammam 31481, Kingdom of Saudi Arabia

3. Office of Minister of Energy, Electricity & Water Authority, Manama 2, Kingdom of Bahrain

Received: July 20, 2015 / Accepted: September 01, 2015 / Published: October 31, 2015.

Abstract: In the deregulated economy, the maximum load forecasting is important for the electric industry. Many applications are included such as the energy generation and purchasing. The aim of the present study is to find the most suitable models for the peak load of the Kingdom of Bahrain. Many mathematical methods have been developing for maximum load forecasting. In the present paper, the modeling of the maximum load, population and GDP (gross domestic product) versus years obtained. The curve fitting technique used to find that models, where Graph 4.4.2 as a tool used to find the models. As well, Neuro-Fuzzy used to find the three models. Therefore, three techniques are used. These three are exponential, linear modeling and Neuro-Fuzzy. It is found that, the Neuro-Fuzzy is the most suitable and realistic one. Then, the linear modeling is the next suitable one.

Key words: Neuro-Fuzzy, peak loads, population, GDP, Graph 4.4.2, curve fitting.

1. Introduction

As it is well known, the load forecasts divided into three categories. These types are the short-term forecasts are for a period of one hour to one week, medium forecasts for period of a week to a year, and the third type is the long-term forecasts, which are longer than a year. Most load forecast methods use statistical techniques or artificial intelligence algorithms such as neural networks, fuzzy logic and expert systems.

Load forecasting helps an electric utility in making important decisions including as mentioned earlier such as decisions on purchasing and generating electric power. Also, more decisions are load switching, area planning and development. Demand for electric power typically depends on several conditions such as GDP (gross domestic product) and the population. These factors are taken into consideration to estimate the maximum load for Kingdom of Bahrain on the long term.

In the present paper, the maximum annual loads for Kingdom of Bahrain for the years 2003-2014 which means twelve years are considered. Based on these annual loads, the model is made using the curve fitting technique through using the package Graph 4.4.2. Using this package, a number of models are made. Graph 4.4.2 is a program designed to draw graphs of mathematical functions in a coordinate system and similar things. It is a standard Windows program with menus and dialogs. At the same time, it is capable of drawing standard functions, parametric functions, polar functions, tangents, point series, shadings and relations. It is also possible to evaluate a function for a given point, trace a graph. Graph 4.4.2 is an open source application used to draw mathematical graphs in a coordinate system.

Qader, et al. [1] in their paper, present study

Corresponding author: Isa Salman Qamber, Ph.D., professor, research field: electric power systems reliability. E-mail: iqamber@uob.edu.bh.

considering maximum electric load of Kingdom of Bahrain over a period of five years. Monte Carlo method used, where its basic variables are presented and discussed from the standard deviation and reserve point of view. The results compared on a weekly and yearly basis. Almeshaiei, et al. [2] in their study, a pragmatic methodology was used as a guide to construct electric power load forecasting models. The methodology they used based on decomposition and segmentation of the load time series. In their study, real data for Kuwait were used. Finally, they obtained the results, which helped in getting the forecast load for future. Qamber [3] in his study, derived a number of models to estimate the electrical demand for future load in Kingdom of Bahrain. The models derived in away describing the electric power demand during summer period. Tawalbeh, et al. [4] in their study, presented a nonlinear method to estimate the consumed energy in distribution feeders. The proposed procedure uses the statistical solution algorithm to analyze the active energy monthly consumption, which enables one to estimate the energy consumption during any period of the year. The effective of the proposed method is demonstrated by comparing the simulated results with that of real measured data. Qamber [5] in his study, proposes the impact of the air temperature on electricity demand as expected. The study concentrated on the period through the years 2009 until 2012. The results obtained using the curve fitting technique. In the study, it is concentrated on the lower, average and maximum loads. Three scenarios carried out and their models obtained. Ryu, et al. [6] in their study, which carried out on the base of Super Grade Hotels that have high-energy consumption per unit area cause a massive amount of load. The study is concentrated on analyzing the energy consumption by using electricity load data. The study carried out to reduce the amount of electricity and peak load through the management and energy efficiency improvement of the large hotels. Koo, et al. [7] in their study performed short-term electric load forecasting using three methods and compared each result. The authors used K-means and k-NN (k-nearest neighbors algorithm) to eliminate error from calendar based classification before making a forecasting model. The authors compared three methods such as artificial neural networks, SES (simple exponential smoothing) and GMDH (group method of data handling). Upshaw, et al. [8] in their article discuss the development of a model for evaluating peak load reduction and change in overall energy consumption for a residential air conditioning compressor with and without condenser-side thermal storage. The model used simulated cooling load data for a typical home in Austin (Texas) based on summer 2011. System performance varied depending on weather data. Kot, et al. in their paper [9] review maximum power point tracking algorithms dedicated for small wind turbines. Three algorithms used are discussed. Two of them are based on turbine static parameters, where the third one iteratively searches for optimum operating point and it does not require prior knowledge of the turbine. Barzin, et al. [10] in their article, present an analysis of a price-based control system in conjunction with energy storage using phase change materials for two applications. Their results showed the importance of selecting a suitable price constraint to examine the benefits.

2. Annual Peak Load Demand

The available historical data for the period 2003 until the year 2014 helped the present study to carried out for estimated values. The factors mentioned in the previous section used to form the models, which help to estimate the annual maximum load for Kingdom of Bahrain. These factors summarized as follows:

- the population;
- the GDP;
- the years (time).

The first two factors depend on the behavior of the human. These factors vary from country to country. Back again to the third factor, this factor depends on

the load itself. The last factor depends on the power system of the Kingdom of Bahrain.

By collecting and analyzing more electric load demand information, this will help the improvement the knowledge of loads in electric power systems.

The load modeling and forecasting based on several factors influencing the load demand. Some factors are:

- time factors: time of the day, day of the week and time of the year;
- climate factors: temperature, humidity, etc.;
- previous load values;
- load curve patters.

The power trading and the EEM (electrical energy management) topics introduced in Kingdom of Bahrain, because it reached a specific concern due to its contribution to economic development and environmental advancement. The power trading and EEM have a logical outcome and the planning of varieties of initiatives that deployed to reduce energy and fuel consumptions. Power trading can be used to reduce the cost of the unit energy which used by the consumer and run the system base on the economic reason.

The EEM is used when there is a growing demand where the demand load expected to be more than the generation, also it is used when there is a shortage in resources “fuel, finance, or energy”. EEM can be used on the demand side to reduce the cost of purchasing electric energy.

There are several types of load management techniques [11]. The EEM will be used in the planning and implementing of the power trading activities to supply peak load demand. The objective of EEM is to influence Bahrain to pre-plan their electricity generation in consideration to achieve peak demand in most economical basis. A typical load curve for typical electricity grid is shown in Fig. 1.

3. Annual Peak Load Modeling

While it is important to determine the estimated peak load based on the actual values for Kingdom of

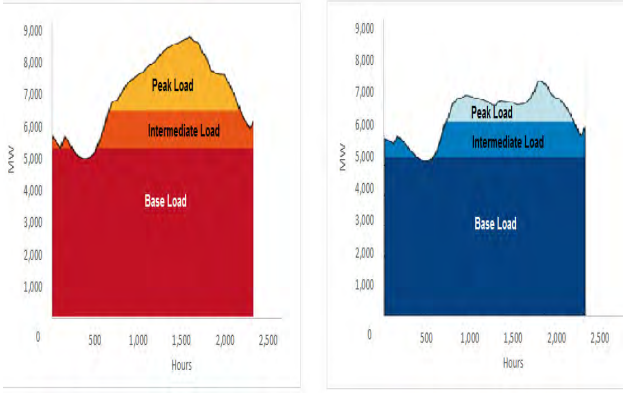

High summer demand day High winter demand day

Fig. 1 Load curves for typical electricity grid.

Bahrain through the years 2003 till 2014, it is necessarily to find the suitable technique for that purpose which is Graph 4.4.2. The technique helps to find the most suitable model for the available peak load data. The obtained estimated values through the period 2003 till 2025.

Eq. (1) illustrates the variation of maximum load demand model (exponential model) for Kingdom of Bahrain through the years (2003-2014). The results coming out of the derived estimated peak load values equation for the period 2003-2025 are shown in the present article. The results are illustrated in Fig. 2 and listed in Table 1. The same data modeled as a linear model, where Eq. (2) represents the growth variation of maximum load and estimated that load for the period 2003-2025 using the linear model. These results are illustrated in Fig. 3 and listed in Table 2.

$$\text{maximum estimated load } (x) = (5.7382629 \times 10^{-57}) \times (1.0707155)^{x} \quad (1)$$

$$\text{maximum estimated load } (x) = (154.2028x) - 307{,}365.15 \quad (2)$$

where:

maximum estimated load (x): the maximum estimated load as a function of year (x):

x: the year.

In the present paper, the model created tested for with actual data available to examine the model and find wither its forecasted values are acceptable or not. After that, the model will be used to forecast the

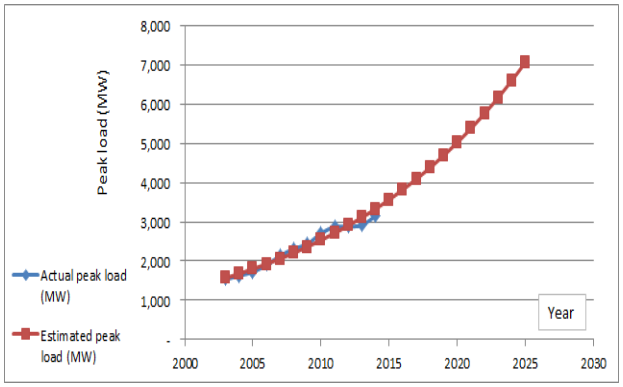

Fig. 2 Actual and estimated maximum load for Kingdom of Bahrain using exponential model.

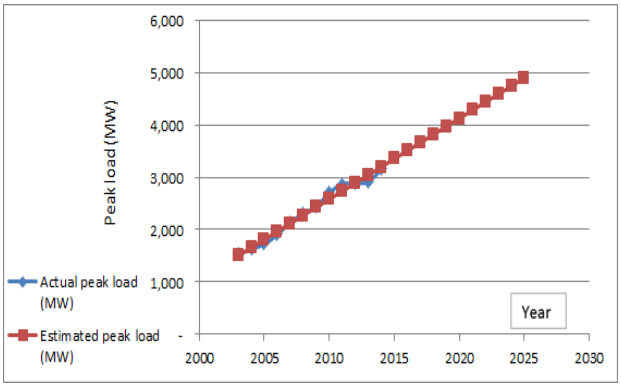

Fig. 3 Actual and estimated maximum load for Kingdom of Bahrain using linear model.

Table 1 Actual and estimated peal load using exponential modeling.

Year	Actual peak load (MW)	Estimated peak load (MW)
2003	1,535	1,570
2004	1,632	1,681
2005	1,725	1,800
2006	1,906	1,928
2007	2,136	2,064
2008	2,314	2,210
2009	2,438	2,366
2010	2,708	2,533
2011	2,871	2,713
2012	2,880	2,904
2013	2,917	3,110
2014	3,152	3,330
2015		3,565
2016		3,817
2017		4,087
2018		4,376
2019		4,686
2020		5,017
2021		5,372
2022		5,752
2023		6,158
2024		6,594
2025		7,060

Table 2 Actual and estimated peak load using linear modeling.

Year	Actual peak load (MW)	Estimated peak load (MW)
2003	1,535	1,503
2004	1,632	1,657
2005	1,725	1,811
2006	1,906	1,966
2007	2,136	2,120
2008	2,314	2,274
2009	2,438	2,428
2010	2,708	2,582
2011	2,871	2,737
2012	2,880	2,891
2013	2,917	3,045
2014	3,152	3,199
2015		3,353
2016		3,508
2017		3,662
2018		3,816
2019		3,970
2020		4,125
2021		4,279
2022		4,433
2023		4,587
2024		4,741
2025		4,896

maximum power for the next ten years. Expected error for the forecasted period is the same error percentage found for the previous period. This paper presents acceptable predicators result values. It is clear that, the model in the present paper was used to predict the peak load for two periods. The first period is the actual peak load period (2003-2014), while the second period is the estimated peak load period (2015-2025).

Table 3 illustrates the actual values of the maximum loads and the date of occurrence through the years 2009 till 2014. The prediction of the peak load is helping to measure progress in planning and management activities for future. The data used in this study were for several years of the demand loads in the Kingdom of Bahrain. The models obtained are simple in term of equation used to calculate the estimated peak loads.

Table 3 Actual peak load values and date of occurrence.

Year	Date	Load (MW)
2009	24-Aug.-09	2,438
2010	25-Aug.-10	2,708
2011	7-Aug.-11	2,812
2012	23-Jul.-12	2,880
2013	4-Sep.-13	2,917
2014	21-Aug.-14	3,077

4. Annual Number of Population Modeling

It is important to obtain the population of Kingdom of Bahrain based on the actual values for the period 2003-2014. For this purpose, it is necessarily to find the suitable package for that aim which is Graph 4.4.2. The package helps to find the most suitable model for the available population data. The obtained model helps to find the estimated values of the population through the period 2003 till 2025.

Eq. (3) shows the variation of population model (exponential model) for Kingdom of Bahrain through the years (2003-2014). The results coming out of the derived estimated population values equation for the period 2003-2025 are shown in the present article. These results are shown in Fig. 4 and listed in Table 4. The same data modeled as a linear model, where Eq. (4) represents the growth variation of population and estimated that, number of population for the period 2003-2025 using the linear model. These results are illustrated in Fig. 5 and listed in Table 5.

$$\text{population}(x) = (5.2979177 \times 10^{-37}) \times 1.0496942^{x} \quad (3)$$

$$\text{population}(x) = (50{,}242.864x) - 99{,}828{,}751 \quad (4)$$

where:

population (x): the estimated population as a function of year (x):

x: the year.

In the present article, it is presented the results which appear to be strong predicators of implementation progress. It is clear that, the model is used to in the present paper to predict the future population for two periods. The first period is the actual population statistics period (2003-2014), while the second period is the estimated population of Kingdom of Bahrain period (2015-2025).

The prediction of the population is helping to measure progress in planning and management activities for future.

5. Annual GDP Values Modeling

The GDP is the primary indicator factor to measure the health of a country's economy. This indictor represents the total BD (Bahraini Dinars) value of

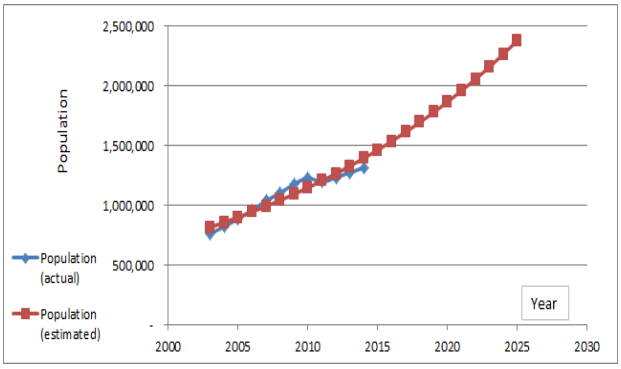

Fig. 4 Actual and estimated number of population for Kingdom of Bahrain using exponential model.

Table 4 Actual and estimated number of population using exponential modeling.

Year	Population (actual)	Population (estimated)
2003	764,519	818,255
2004	823,744	858,918
2005	888,824	901,601
2006	960,425	946,405
2007	1,039,297	993,436
2008	1,103,496	1,042,804
2009	1,178,415	1,094,625
2010	1,228,543	1,149,022
2011	1,195,020	1,206,122
2012	1,234,900	1,266,059
2013	1,274,800	1,328,975
2014	1,316,500	1,395,017
2015		1,464,341
2016		1,537,110
2017		1,613,496
2018		1,693,677
2019		1,777,843
2020		1,866,192
2021		1,958,931
2022		2,056,278
2023		2,158,463
2024		2,265,726
2025		2,378,320

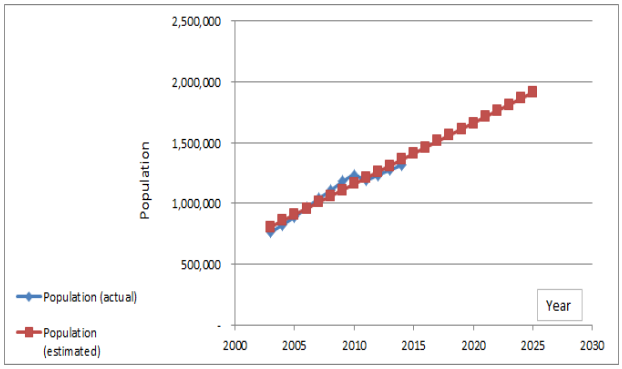

Fig. 5 Actual and estimated number of population for Kingdom of Bahrain using linear model.

Table 5 Actual and estimated number of population using linear modeling.

Year	Population (actual)	Population (estimated)
2003	764,519	807,706
2004	823,744	857,948
2005	888,824	908,191
2006	960,425	958,434
2007	1,039,297	1,008,677
2008	1,103,496	1,058,920
2009	1,178,415	1,109,163
2010	1,228,543	1,159,406
2011	1,195,020	1,209,649
2012	1,234,900	1,259,891
2013	1,274,800	1,310,134
2014	1,316,500	1,360,377
2015		1,410,620
2016		1,460,863
2017		1,511,106
2018		1,561,349
2019		1,611,591
2020		1,661,834
2021		1,712,077
2022		1,762,320
2023		1,812,563
2024		1,862,806
2025		1,913,049

consumed electric power produced plus all goods and services over a specific period of time. This means this will measure the size of the economy of the country. The GDP expressed as a comparison to the previous quarter or year. Therefore, it is important to obtain the GDP of Kingdom of Bahrain based on the actual values for the period 2003-2014. For this purpose, a suitable technique for this aim needed is Graph 4.4.2. The technique helps to find the most suitable model for the available GDP data. The obtained model helps to find the estimated values of the GDP through the period 2003 till 2025.

Eq. (5) shows the variation of GDP model (exponential model) for Kingdom of Bahrain through the years (2003-2014). The results coming out of the derived estimated GDP values equation for the period 2003-2025 are shown in the present study. The results are shown in Fig. 6 and listed in Table 6. The same

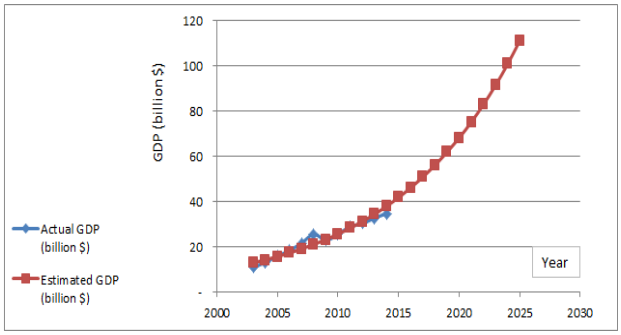

Fig. 6 Actual and estimated GDP values for Kingdom of Bahrain using exponential model.

Table 6 Actual and estimated GDP values using exponential modeling.

Year	Actual GDP (billion $)	Estimated GDP (billion $)
2003	11.08	12.97
2004	13.15	14.30
2005	15.97	15.77
2006	18.51	17.38
2007	21.73	19.17
2008	25.71	21.14
2009	22.94	23.30
2010	25.71	25.70
2011	29.04	28.33
2012	30.36	31.24
2013	32.79	34.45
2014	34.78	37.99
2015		41.88
2016		46.18
2017		50.92
2018		56.15
2019		61.92
2020		68.27
2021		75.28
2022		83.01
2023		91.53
2024		100.92
2025		111.28

data modeled as a linear model, where Eq. (6) represents the growth variation of GDP and estimated that GDP values for the period 2003-2025 using the linear model. These results are illustrated in Fig. 7 and listed in Table 7.

$$\text{GDP}(x) = (1.3011731 \times 10^{-84}) \times (1.1026447^{x}) \quad (5)$$

$$\text{GDP}(x) = (2.0979371x) - 4{,}190.2258 \quad (6)$$

where:

GDP (x): the estimated GDP value as a function of year (x):

x: the year.

In the present paper, it presents the results, which appear to be strong predicators of implementation progress. It is clear that, the model used in the present paper is to predict the future estimated GDP values for two periods. The first period is the actual GDP statistics period (2003-2014), while the second period is the estimated GDP of Kingdom of Bahrain period (2015-2025).

The prediction of the GDP is helping to measure progress in planning and management activities for future. The GDP represents the economic production and growth, which has a large impact on nearly everyone within that economy. A significant change in GDP usually has a significant effect on the stock market whether up or down.

6. Minimum, Average and Maximum Percentages

Earlier, the modeling of the annual maximum load, population and GDP carried out and obtained using the Graph 4.4.2. Both the exponential and linear models had obtained. As a summary of the results which shown earlier can be summarized in Tables 8 and 9. Table 8 shows the results for the exponential modeling and Table 9 illustrates the results of the linear modeling. By comparing the results obtained and listed in both Tables 8 and 9, it is clear that, the percentage error for the three variables (population, peak load and GDP), is less in linear modeling than that of the exponential modeling, which means it was

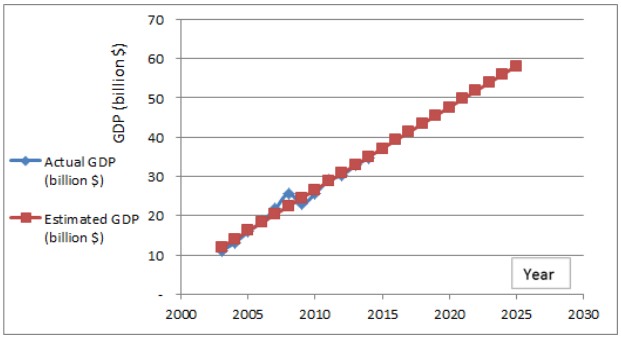

Fig. 7 Actual and estimated GDP values for Kingdom of Bahrain using linear model.

Table 7 Actual and estimated GDP values using linear modeling.

Year	Actual GDP (billion $)	Estimated GDP (billion $)
2003	11.08	11.94
2004	13.15	14.04
2005	15.97	16.14
2006	18.51	18.24
2007	21.73	20.33
2008	25.71	22.43
2009	22.94	24.53
2010	25.71	26.63
2011	29.04	28.73
2012	30.36	30.82
2013	32.79	32.92
2014	34.78	35.02
2015		37.12
2016		39.22
2017		41.31
2018		43.41
2019		45.51
2020		47.61
2021		49.71
2022		51.80
2023		53.90
2024		56.00
2025		58.10

Table 8 Minimum, average and maximum percentages using exponential modeling.

Population (%)	Minimum	0.9
	Average	4.3
	Maximum	7.1
Peak load (%)	Minimum	0.8
	Average	3.9
	Maximum	6.6
GDP (%)	Minimum	1.3
	Average	7.0
	Maximum	17.8

Table 9 Minimum, average and maximum percentages using linear modeling.

Population (%)	Minimum	0.2
	Average	3.3
	Maximum	5.9
Peak Load (%)	Minimum	0.4
	Average	2.5
	Maximum	4.7
GDP (%)	Minimum	0.4
	Average	4.2
	Maximum	12.8

more realistic. Therefore, it recommended following and using the linear modeling.

7. Neuro-Fuzzy Technique

The Neuro-Fuzzy systems are combination of advantages of the neural networks and fuzzy logic. It was noted that, neural networks have two main benefits. First, they are capable of learning non-linear mappings of numerical data. Second, they perform parallel computation. However, the operation of neural networks has also many weaknesses. Therefore, it is very hard to understand the meaning of weights, and the incorporation of prior knowledge into the system which is usually impossible. Fuzzy logic uses human understandable linguistic terms to express the knowledge of the system. This makes a possible close interaction between the system and human operator, which is a very desirable property.

Therefore, the aim of Neuro-Fuzzy systems is to combine collectively the benefits of both approaches. Simply, the operation of the system is expressed as linguistic fuzzy expressions and learning schemes of neural networks that used to learn the system. In addition, Neuro-Fuzzy systems allow incorporation of both numerical and linguistic data into the system. The Neuro-Fuzzy system is also capable of extracting fuzzy knowledge from numerical data.

The general model for the Neuro-Fuzzy system is shown in Fig. 8 which illustrates the five-layer connection for two inputs and one output. These five layers represent the Neuro-Fuzzy model, which is used to represent the population, GDP and years models are used to generate Bahrain peak load demand [12].

The operation of this system can be described layer by layer as follows:

- Layer 1: fuzzification

This layer consists of linguistic variables. Using membership functions of the linguistic variables Ai fuzzifies the crisp input $P_{\max}$.

Usually, triangular, trapezoid, or bell-shaped membership functions are used. For example, the bell-shaped membership functions are defined as follows:

$$\mu_c(x) = \exp\left(\frac{\|x - c_c\|^2}{\sigma_c^2}\right) \tag{7}$$

where, x is a fuzzy set, c_c is its center and σ_c is its width.

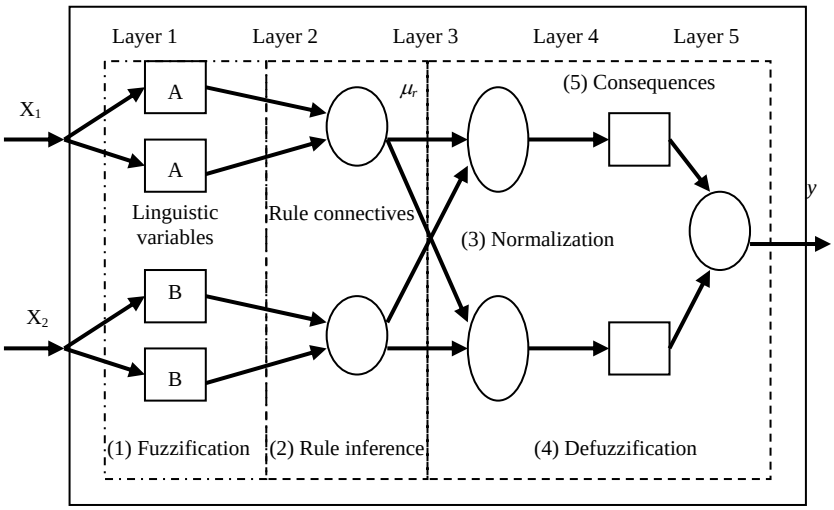

Fig. 8 A neural fuzzy inference system.

- Layer 2: rule nodes

The second layer contains one node per each fuzzy if-then rule. Each rule node performs connective operation between rule antecedents (if-part). Usually, the minimum or the dot product is used as intersection AND. The union OR is usually done using maximum operation. In our example case the firing strengths α_i of the fuzzy rules are computed according to:

$$\alpha_i = \min\{\mu_A(x_1), \mu_B(x_2)\} \quad (8)$$

where, $\mu_A(x_1)$ and $\mu_B(x_2)$ are membership of input variables.

- Layer 3: normalization

In this layer, the firing strengths of the fuzzy rules are normalized according to:

$$\alpha^x = \frac{\alpha_r}{\sum_{i=0}^{m} \alpha_i} \quad (9)$$

- Layer 4: consequence layer

This layer is related to consequent fuzzy label z_i. The values of the singletons are multiplied by normalized firing strengths according to:

$$f_r = \sum_{i=0}^{m} z_i \alpha^x \quad (10)$$

- Layer 5: summation

This layer computes the overall output as the summation of the incoming signals:

$$f_s = \sum_{i=0}^{m} f_r \quad (11)$$

Newton algorithm is the popular truncated approach to find a step size and direction in weight space that drives a cost function towards its minimum. Using Taylor's expansion the cost function J_N (w) can be locally approximated by the quadratic function Jang, et al. [12]:

$$J_N(w+\Delta w) = J_N(w) + \Delta w \frac{\mathrm{d}J_N(w)}{\mathrm{d}w} + \frac{1}{2}\Delta w^T \frac{\mathrm{d}^2 J_N(w)}{\mathrm{d}w^2}\Delta w \quad (12)$$

where, Δw is the weight vector update.

The new Neuro-Fuzzy weight update vector can be found by minimization of Eq. (13). Differentiating that function with respect to w, and setting the result to zero will minimize Eq. (13):

$$\frac{\mathrm{d}J_N(w)}{\mathrm{d}w} = \frac{\mathrm{d}^2 J_N(w)}{\mathrm{d}w^2}\Delta w \quad (13)$$

$$g = -H\Delta w \quad (14)$$

where, g and H represent the gradient and Hessian of J_N (w_k), respectively.

The fuzzy reasoning rules can be divided into four main types. For simplicity, only the two-input single-output model of the Neuro-Fuzzy system is now presented. Four types of the fuzzy rules can be described as follows:

IF x_1 is A_1 AND x_2 is A_2 THEN y is B (15)

IF x_1 is A_1 AND x_2 is A_2 THEN y is z (16)

IF x_1 is A_1 AND x_2 is A_2 THEN y is $f(x_1, x_2)$ (17)

IF x_1 is $a_{j,1}$ AND x_2 is $a_{j,2}$ THEN y is z (18)

where, x_i is the i-th input variable, and A_i is the one of the linguistic variables defined for it.

The fuzzy output variable y defined separately for each rule. In the first rule, the consequence of the rule is fuzzy set B, while the second rule uses a singleton. The consequence of third rule is a function of the input variable. The antecedent part of the fourth rule uses the reference values $a_{j,i}$, when the firing strength of the rule is computed by measuring the distance between the inputs and the references.

However, the operation of neural networks has also many weaknesses. For instance, in the popular multi-layer perception network the knowledge of the system distributed into the whole network as synaptic weights. Therefore, it is very hard to understand the meaning of weights, and the incorporation of prior knowledge into the system is usually impossible.

Fuzzy logic uses human understandable linguistic terms to express the knowledge of the system. This makes possible a close interaction between the system and human operator, which is very desirable property. Therefore, the aim of Neuro-Fuzzy systems is to combine collectively the benefits of both approaches. Simply, the operation of the system expressed as linguistic fuzzy expressions and learning schemes of neural networks used to learn the system.

In addition, Neuro-Fuzzy systems allow

incorporation of both numerical and linguistic data into the system. The Neuro-Fuzzy system is also capable of extracting fuzzy knowledge from numerical data. The Neuro-Fuzzy systems divided into two main groups, the neural fuzzy inference systems and fuzzy neural networks. Learning the mapping of maximum power point data to inverter frequency leads to the formulation of an approximation problem.

Various neural networks, e.g., MLP (multi-layer perceptions) or radial-basis function networks are capable of learning nonlinear mappings and generalizing over a set of methods very accurately. Rule-based neural networks implement a fuzzy logic system.

The results coming out of the Neuro-Fuzzy are shown in Figs. 8-12. The obtained results have lowest percentage errors compared with previous two models (linear and exponential).

(a) Neuro-Fuzzy model using one input and one output

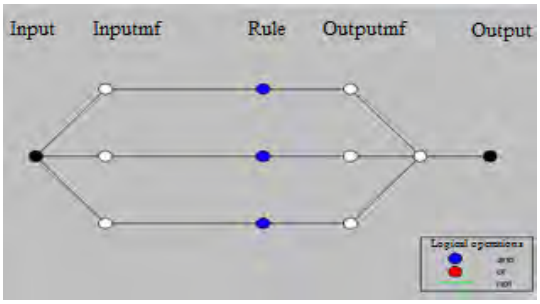

(b) The five stages in the Neuro-Fuzzy model

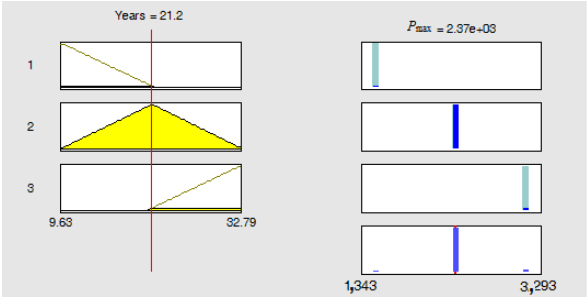

(c) Neuro-Fuzzy method to generate maximum peak load using membership function

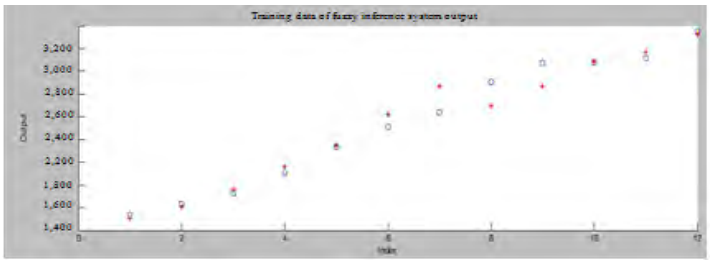

(d) Results of forecasted maximum peak load using Neuro-Fuzzy model vs. actual data where inputs is population and output is P_{max}

Fig. 9 Neuro-Fuzzy maximum peak load model, stages, output calculation and results.

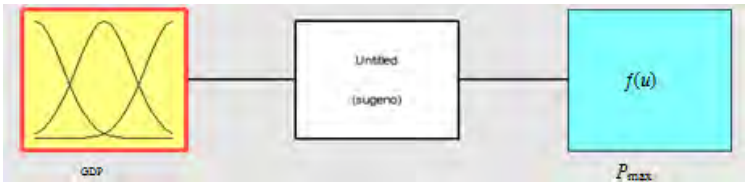

(a) GDP Neuro-Fuzzy model using one input and one output

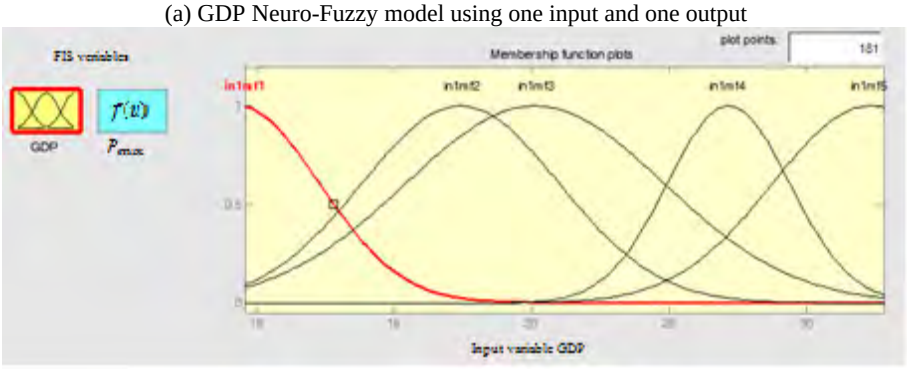

(b) GDP Neuro-Fuzzy membership used in the model

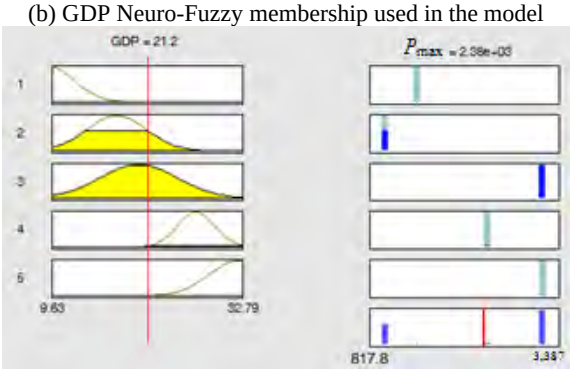

(c) Neuro-Fuzzy method to generate output value using membership function

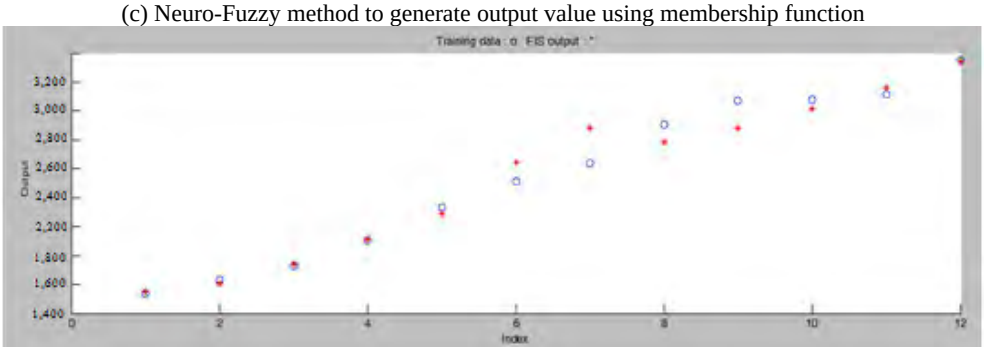

(d) Results of forecasted peak load using Neuro-Fuzzy model Vs actual data where inputs is GDP and output is P_{max}

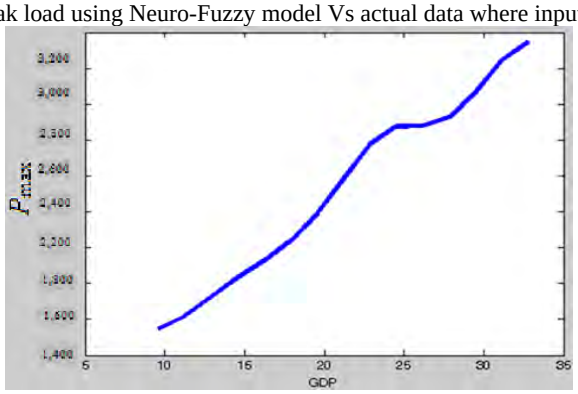

(e) Surface representation for the knowledged learned using adaptive neuro fuzzy inference system to represent the relation between GDP and P_{max}

Fig. 10 GDP Neuro-Fuzzy model, stages, output calculation and results.

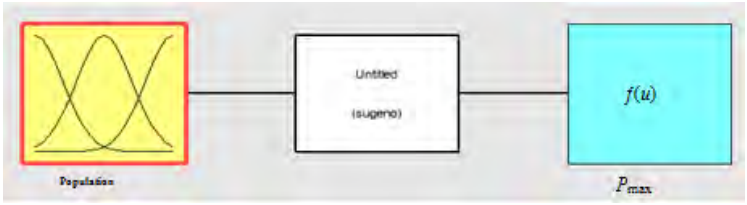

(a) Population Neuro-Fuzzy model to find P_{max} using one input and one output

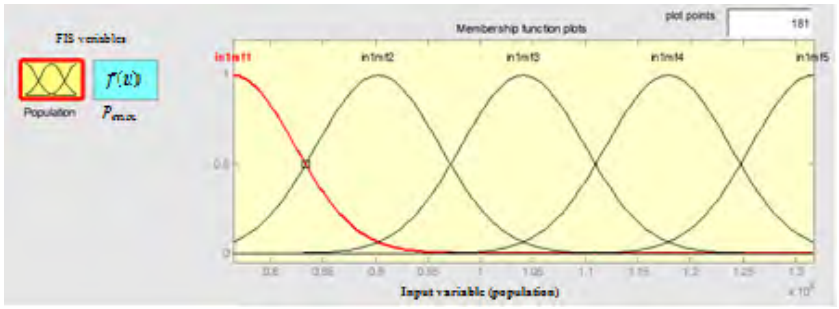

(b) Population Neuro-Fuzzy membership used in the model

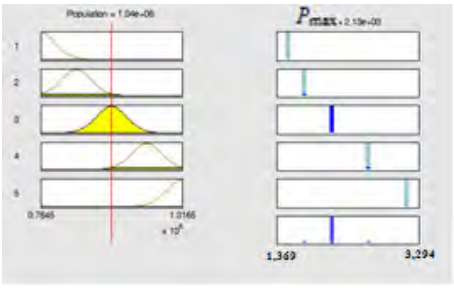

(c) Population Neuro-Fuzzy method to generate output value using membership function

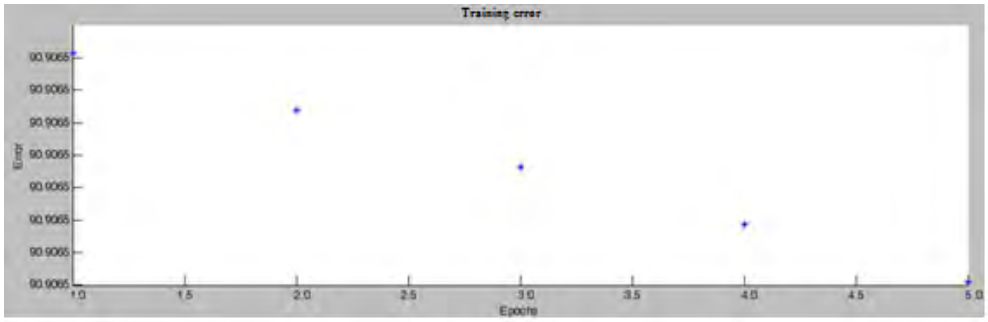

(d) Error (%) for maximum peak load generated from the Population model using Neuro-Fuzzy model

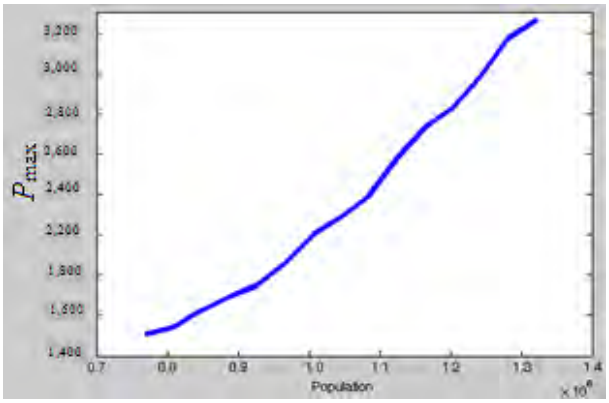

(e) Surface representation for the knowledged learned using ANFIS to represent the relation between Population and P_{max}

Fig. 11 Neuro-Fuzzy model, stages, output calculation and result errors.

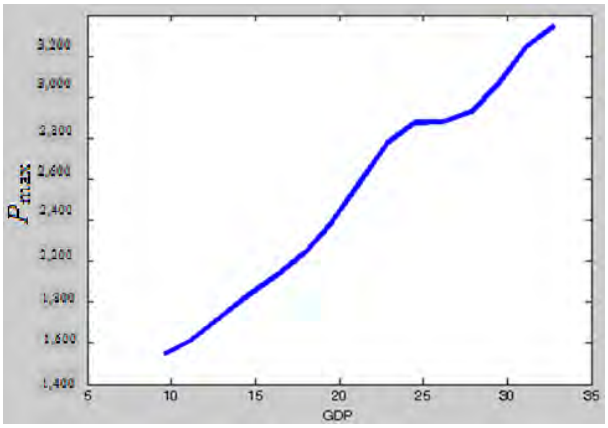

Fig. 12 Surface representation for the knowledged learned using adaptive Neuro Fuzzy inference system to represent the relation between GDP and P_{max}.

8. Discussion

It is necessary to investigate the properties of electricity maximum loads for the Kingdom of Bahrain. The yearly energy consumption at Bahrain during summer is increasing in the rate of 6% averagely, where it increases in certain years due to development in the country. The electricity demands increased instantaneously with time. Electricity is used for various purposes. It consumed at residential, industrial, agricultural and commercial sectors. Limited research studies on maximum load estimation of Bahrain reveal more exploration and investigation regarding theoretical and experimental framework. The historical data of the maximum loads of the Kingdom of Bahrain are illustrated in the previous sections. Bahrain network is connected to the GCC (Gulf Cooperation Council) countries (regional electric grid). Rising electricity demand indicates from the available data. The derived models can estimate the peak loads for the coming years. The models are used by anyone with a basic understanding of electric sector or even with no basic understanding. The moderate growth in the peak load is attributed to moderate economic growth over the time period of study which impacted both energy and peak load demand.

9. Conclusions

Two techniques are used in the present study to estimate the maximum loads, population and GDP for Kingdom of Bahrain. These techniques are the exponential and linear modeling using Graph 4.4.2 as a curve fitting technique. The most suitable one and more realistic in modeling for the study is the linear modeling, where the minimum percentage error between the estimated and actual values is obtained. For the Population the maximum percentage error is 5.9% using the linear modeling, which shows for the exponential as 7.1%. For the peak load, the maximum percentage error is 4.7% using the linear modeling, which shows for the exponential as 6.6%. For the GDP, the maximum percentage error is 12.8% using the linear modeling, which shows for the exponential as 17.8%. The Neuro-Fuzzy results are obtained having 1.15% error for the peal load versus years, 1.07% error for the GDP versus peak load and 0.91% error for population versus peak load. The present paper discusses simple models for estimated peak loads and an efficient algorithm to calculate the model parameters of each case. It is clear that, the input parameters of each model are historical loads, GDP and population data on the Kingdom of Bahrain. Finally, using most suitable modeling for the three estimated models, which are the annual peak load, population and GDP are found. These models are so close to the real values.

Acknowledgments

We would like to express our thanks to H. E. Dr.

Abdul-Husain Bin Ali Mirza the Minister of Energy (Kingdom of Bahrain) for his encouragement and supporting the development of energy research.

References

[1] Qader, M. M., and Qamber, I. 2010. "Long-Term Load Forecasting for the Kingdom of Bahrain Using Monte Carlo Method." *JAAUBAS* 9 (1): 21-31.

[2] Almeshaiei, E., and Soltan, H. 2011. "A Methodology for Electric Power Load Forecasting." *Alexandria Engineering Journal* 50 (2): 137-44.

[3] Qamber, I. S. 2012. "Peak Load Modeling for Kingdom of Bahrain." *Journal of Software Engineering and Applications* 5 (12B): 46-9.

[4] Tawalbeh, N., and El-Khazali, R. 2012. "Peak Load Evaluation Based on the Accumulated Annual Energy." In *Proceedings of the 16th IEEE Mediterranean Electro-technical Conference on MELECON (Mediterranean Electro-technical Conference) 2012*, 544-7.

[5] Qamber, I. S. 2013. "Estimation of the Maximum Annual Loads Modeling for Kingdom of Bahrain." *Journal of Energy and Power Engineering* 7 (October): 2006-11.

[6] Ryu, J. H., Hong, W. H., and Seo, Y. K. 2014. "A Study of the Analysis on the Properties of Electricity Peak Load of Large Hotel Building in Consideration of Energy Efficiency." *Advanced Science and Technology Letters* 47 (2): 6-10.

[7] Koo, B., Lee, S., Kim, W., and Park, J. 2014. "Comparative Study of Short-Term Electric Load Forecasting." In *Proceedings of the Fifth IEEE International Conference on Intelligent Systems, Modelling and Simulation*, 463-7.

[8] Upshaw, C. R., Rhodes, J. D., and Webber, M. E. 2015. "Modeling Peak Load Reduction and Energy Consumption Enabled by an Integrated Thermal Energy and Water Storage System for Residential Air Conditioning Systems in Austin." *Energy and Buildings* 97 (15): 21-32.

[9] Kot, R., Rolak, M., and Malinowski, M. 2013. "Comparison of Maximum Peak Power Tracking Algorithms for a Small Wind Turbine." *Mathematics and Computers in Simulation* 91 (May): 29-40.

[10] Barzin, R., Chen, J., Yourng, B. R., and Farid, M. M. 2015. "Peak Load Shifting with Energy Sorage and Price-Based Control System." *Energy* (article in press): 1-10.

[11] Afua, M., and Mohamed, T. K. 2009. "A Review of Electrical Energy Management Techniques: Supply and Consumer Side (Industries)." *Journal of Energy in Southern Africa* 20 (3): 14-21.

[12] Gupta, M. M., and Rao, D. H. 1994. "On the Principles of Fuzzy Neural Networks." *Fuzzy Sets and Systems* 61 (1): 1-18.

Journal of Energy and Power Engineering 9 (2015) 886-895
doi: 10.17265/1934-8975/2015.010.007

Modified Nitrogen-Doped Graphene Electrocatalyst for Oxygen Reduction Reaction in Alkaline Fuel Cells

Dureid Qazzazie[1, 2], Michaela Beckert[3], Rolf Mülhaupt[3], Olena Yurchenko[1, 2] and Gerald Urban[2]

1. Freiburg Materials Research Center, University of Freiburg, Freiburg D-79104, Germany

2. Laboratory for Sensors, Department of Microsystems Engineering, University of Freiburg, Freiburg D-79110, Germany

3. Institute for Macromolecular Chemistry, University of Freiburg, Freiburg D-79104, Germany

Received: June 08, 2015 / Accepted: July 08, 2015 / Published: October 31, 2015.

Abstract: We report modified nitrogen-doped graphene (CN) as electrocatalyst for ORR (oxygen reduction reaction) in alkaline medium. CN was synthesized by a novel procedure based on graphite oxide thermally treated with cyanamide suitable for facile N-doping and large-scale production, whereas cyanamide was used as N-precursor. The structure of the material was characterized by TEM (transmission electron microscopy), SEM (scanning electron microscopy), Raman spectroscopy and XPS (X-ray photoelectron spectroscopy). Structural and electrochemical properties of CN were compared with those of non-modified graphene (TRGO (thermally reduced graphite oxide)). The electrochemical characterization of TRGO and CN in alkaline solution demonstrates enhanced electrocatalytic ORR activity and improved long-term stability for N-doped CN. Voltammetric studies confirmed that, oxygen reduction on CN rather follows four-electron pathway. Compared with commercial 20% PtC catalyst, CN is characterized by exceptional methanol crossover resistance and superb long-term operation stability. Owing to these factors, nitrogen-doped graphene has a great potential to be used as metal-free electrocatalyst in cathodes of alkaline fuel cells.

Key words: Nitrogen-doped graphene, metal-free catalysis, oxygen reduction reaction, alkaline fuel cells.

1. Introduction

Fuel cells generate electric power through the conversion of chemical energy into electrical energy. Within the framework of an electrochemical process, the fuel such as hydrogen or methanol, oxidizes at the anode and the oxidizing agent, usually oxygen, is reduced to water at the cathode. In general, catalysts at the respective electrode are used to increase the fuel cells' efficiency.

Due to the sluggish ORR (oxygen reduction reaction) kinetics, platinum-based catalyst materials are widely investigated as cathodes for fuel cells to catalyse ORR in lab-scale applications. A fundamental drawback for the development of commercial fuel cells containing platinum-based electrodes is derived from high costs as well as limited reserves of platinum in nature. Further problems arise from the vulnerability of platinum-based materials to time-dependent drift and poisoning effects, such as CO and alcohol "poisoning" leading to the catalyst deactivation [1, 2]. Therefore, the development of novel metal-free materials has become the focus of research to substitute platinum-based catalysts. The performance requirements for alternative metal-free electrocatalysts in cathodes for the oxygen reduction reaction with regard to their electrocatalytic activity and stability were already reviewed many times [2, 3]. It becomes obvious that, the development of alternative lower cost electrocatalysts for the oxygen reduction reaction is of high significance for the further development of fuel cells and consequently, further progress towards clean energy generation.

According to their excellent properties, carbon-based materials, especially graphene have been

Corresponding author: Dureid Qazzazie, Ph.D. student, research fields: catalytic nanomaterials and fuel cells. E-mail: dureid.qazzazie@fmf.uni-freiburg.de.

moved into the focus of material research for electrochemical applications. Graphite and activated carbon already represent lower-cost alternative catalysts as cathodes for fuel cells in industrial applications. Compared with graphite and activated carbon, graphene is characterized by improved electrocatalytic ORR performance. Zhu, et al. [4] present in their review recent advancements in the development of different graphene-based electrocatalysts for ORR, highlighting specific graphene-based nanomaterials for electrochemical energy applications. Various modifications of graphene are of particular interest due to easy processability, low costs, large surface area and high porosity [5, 6], outstanding thermodynamic [7], electrical [8] and mechanical properties [9, 10]. All these exceptional properties also make graphene-based materials particularly feasible for use in micro energy harvesting applications. The electronic and optical properties of graphene can even be modified by doping with heteroatoms, such as nitrogen or boron [11, 12]. Hence, there is a growing trend towards doping graphene with heteroatoms to increase the electrocatalytic ORR performance, thus, producing modified Pt-free graphene-based electrocatalysts for ORR.

The focus of this paper is centered on nitrogen-doped graphene. The electrocatalytic ORR activity of nitrogen-containing carbon nanomaterials was originally reported in Refs. [11, 13, 14]. In their review, Wang, et al. [15] have summarized different synthesis and characterization methods of nitrogen-doped graphene. Based on experimental and theoretical studies, they also have presented recent applications of nitrogen-doped graphene. In particular, nitrogen-doped carbon-based materials represent promising metal-free electrocatalysts due to their enhanced electrocatalytic activity, long-term stability and environmental sustainability [16]. Compared with Pt and commercial PtC catalysts, nitrogen-doped graphene is characterized by notably better stability [17, 18]. Besides, it is also demonstrated that, the activity of nitrogen-doped graphene is not influenced by adding carbon monoxide or methanol [11, 18].

In this context, it should be pointed out that, various techniques exist for graphene synthesis and modification. Micromechanical exfoliation has marked the breakthrough for the preparation of highly qualitative and pure graphene but the drawback here is low yield [19]. A further common method for the production of ultra-thin graphene with relatively high quality is the epitaxial growth which in turn suffers from high synthesis temperatures [20]. CVD (chemical vapor deposition) provides another common technique for the production of graphene capable for industrial applications [21]. However, prepared graphene by CVD suffers from impurity and the transfer of graphene to substrate can become complicated depending on the target substrate. Recently, Tölle, et al. [22] have developed a versatile method for a facile, low-cost, environmentally friendly and large-scale production of graphene-based materials offering a promising alternative to conventional techniques. The printing-based process features special opportunities for the integration of graphene-based materials in both macro-scale applications and, especially microsystems engineering as well as electronics applications.

Here, we report nitrogen-doped graphene as metal-free electrocatalyst for oxygen reduction reaction at alkaline conditions prepared by a novel synthesis procedure. The procedure is suited for facile production of nitrogen-doped graphene and based on graphite oxide thermally treated with cyanamide which is used as nitrogen-precursor. The structure of the prepared graphene-based materials was mainly characterized by Raman spectroscopy and XPS (X-ray photoelectron spectroscopy). Besides, graphene and nitrogen-doped graphene were electrochemically characterized by CV (cyclic voltammetry) and LSV (linear sweep voltammetry). Further electrochemical tests were conducted to investigate methanol crossover effect and long-term operation stability of prepared

materials. The electrochemical properties and electrocatalytic activity of prepared graphene and nitrogen-doped graphene towards ORR are demonstrated and compared to those of commercial 20% Pt/C catalyst. The use of nitrogen-doped graphene as alternative Pt-free electrocatalyst in alkaline fuel cells opens up opportunities for achieving clean and low-cost power generation.

2. Experimental Details

2.1 Materials

The graphene-based materials were synthesized by a process based on the thermal treatment of graphite oxide. A detailed report about the synthesis procedure is presented by Tschoppe, et al. [23]. Shortly, TRGO (thermally reduced graphite oxide) was synthesized by oxidation of graphite oxide and subsequent thermal reduction. Prepared graphene (TRGO) contains different oxygenated functional groups, mostly carboxylic and sulfonic acids. The nitrogen-doped derivative (CN) was prepared by a similar procedure involving oxidation of graphite and subsequent thermal reduction in the presence of liquid cyanamide as a nitrogen-containing precursor, hence, enabling the incorporation of nitrogen atoms into carbon lattice. Both materials were prepared under identical thermal conditions.

2.2 Surface Analysis

TEM (transmission electron microscopy), SEM (scanning electron microscopy) and Raman spectroscopy were proceeded to evaluate the nanostructure and its morphology. The TEM-measurements were performed on a Leo 912-Omega transmission electron microscope of the company Zeiss (Oberkochen, Germany), with an acceleration voltage of 120 kV. The SEM images were taken using a Quanta (field emission gun) 250. The Raman measurements were performed at room temperature using Raman spectrometer (Confocal Raman MicrocopeLabram 800, JobinYvon Horiba) with a 632.8 nm-wavelength laser (HeNe 20 MW laser polarized 500:1). XPS was used to determine the elemental compositions of TRGO and CN and performed by XPS Perkin Elmer Phi 5600 System instrument with a Mg-standard-anode as an excitation source (energy: 1,253.6 eV).

2.3 Electrochemical Measurements

The electrochemical characterization of TRGO and CN was performed via CV and LSV. The electrochemical measurements were carried out in a three electrode cell at a potential scan rate of 5 $mV \cdot s^{-1}$ in alkaline 0.1 M aqueous potassium hydroxide solution (KOH). In order to prepare the electrode, 5 mg of prepared TRGO-, CN powder or commercially available Pt/C (20% wt. Pt) catalyst were dispersed in 5 mL isopropanol and sonicated for 30 min forming a homogeneous sample ink. The working electrode, a GC (glassy carbon) electrode of 3 mm in diameter, was subsequently coated with 20 μL of the respective sample ink and dried in air for at least 24 h. It may be pointed out that, neither Nafion nor any other solvent were added on top of electrode. A platinum sheet was used as counter electrode and Ag/AgCl as reference electrode (3 M KCl; double junction; Metrohm 6.0733.100). Before each measurement, the electrolyte either was degassed with nitrogen or oxygen gas for 20 min, in order to saturate the solution. During the measurement, the gas flowing was maintained over the solution providing a continuous saturation of the electrolyte. All measurements were controlled using the potentiostat Autolab PGSTAT126N and the software GPES (general purpose electrochemical system) and were performed at room temperature (approximately 22 °C).

3. Results and Discussions

3.1 Surface Characterization of TRGO and CN

The surface morphology of prepared graphene-based materials was first investigated by TEM and SEM, both TEM and SEM images are exemplarily displayed

in Fig. 1. The TEM image (Fig. 1a) confirms characteristic two dimensional (2D) structure of obtained few layer carbon nanosheets. The SEM image (Fig. 1b) illustrates the microporous structure of a typical nitrogen-doped graphene (CN) sample. The prepared materials typically feature two-dimensional (2D) carbon nanosheets with tangly wrinkled morphology.

Raman spectroscopy was applied to investigate the defect level in carbon lattice of the prepared materials. Fig. 2a displays the Raman spectra of CN compared with TRGO and graphite. The Raman spectrum of graphite mainly shows a typical G peak at 1,576 cm^{-1} corresponding to ideal single-crystal graphite [24]. The Raman spectra of TRGO and CN display G bands shifted to 1,595 cm^{-1} and 1,588 cm^{-1}, respectively. The position of G band is quite sensitive to strains in the crystalline structure of carbon-based materials. The downshifted position of G band in graphite points to the relaxed graphitic structure of carbon lattice in graphite. Compared with TRGO the G peaks' position of CN shifts down closer to the G bands' position of graphite which we ascribe to the restoration of the graphitic structure in CN after the incorporation of nitrogen atoms and thermal treatment of the material [25].

Another predominant characteristic in the Raman spectra of prepared graphene- based materials is derived from the D band, usually represented by peaks at around 1,320-1,370 cm^{-1}. In graphite, the D band is typically very weak as shown in Fig. 2a, while in contrast, clearly rised D bands appear at 1,344 cm^{-1} for TRGO and at 1,365 cm^{-1} for CN. The D bands relate to the disorder-induced feature and their presence can be attributed to a modest defective structure of the graphene-based materials [26]. Besides, the I_D/I_G ratio is taken into account to explore the density of defects in the samples. For graphite, the I_D/I_G ratio is approximately 0.15, I_D/I_G increases to 1 for TRGO and 1.11 for CN. The increase of I I_D/I_G can be ascribed to the presence of a substantial amount of defects in TRGO and CN. XPS was further used to characterize

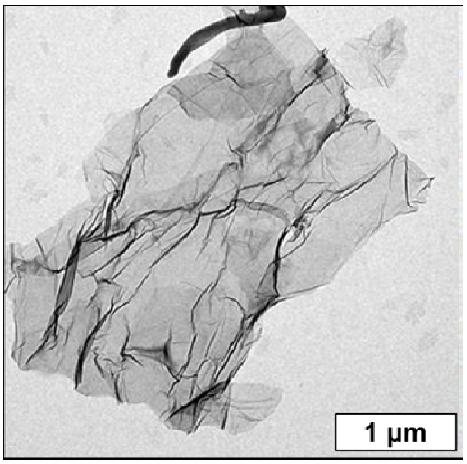

(a)

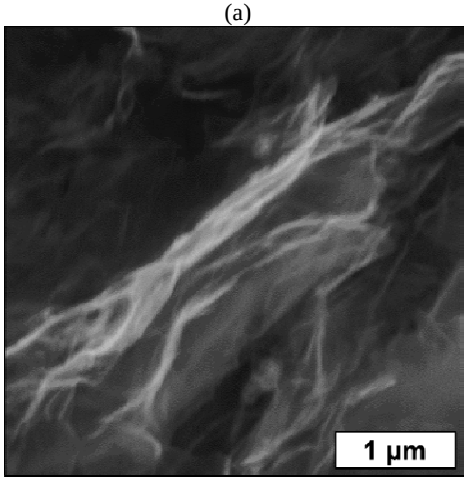

(b)

Fig. 1 (a) TEM image and (b) SEM image of typical nitrogen-doped graphene (CN) samples showing, the characteristic surface morphology of prepared materials.

the chemical composition of the prepared samples, thus, to verify the nitrogen-doping in carbon lattice. The XPS spectra of TRGO and CN, depicted in Fig. 2b, noticeably show major graphitic C1s peaks at about 285 eV. Oxygen functionalities are present in both TRGO and CN. Unlike TRGO, specific N1s peak occurs in the survey spectrum of CN at approximately 400 eV. The N1s peak corresponds to nitrogen and clearly confirms the successful incorporation of nitrogen atoms into carbon lattice of CN. The peak intensity ratio of N1s, O1s and C1s is used to identify the content of nitrogen in CN, i.e., 11%. The N1s spectrum were further deconvoluted to individual peaks, in order to determine the specific nitrogen configurations in CN. The graphical illustration of high-resolution N1s XPS

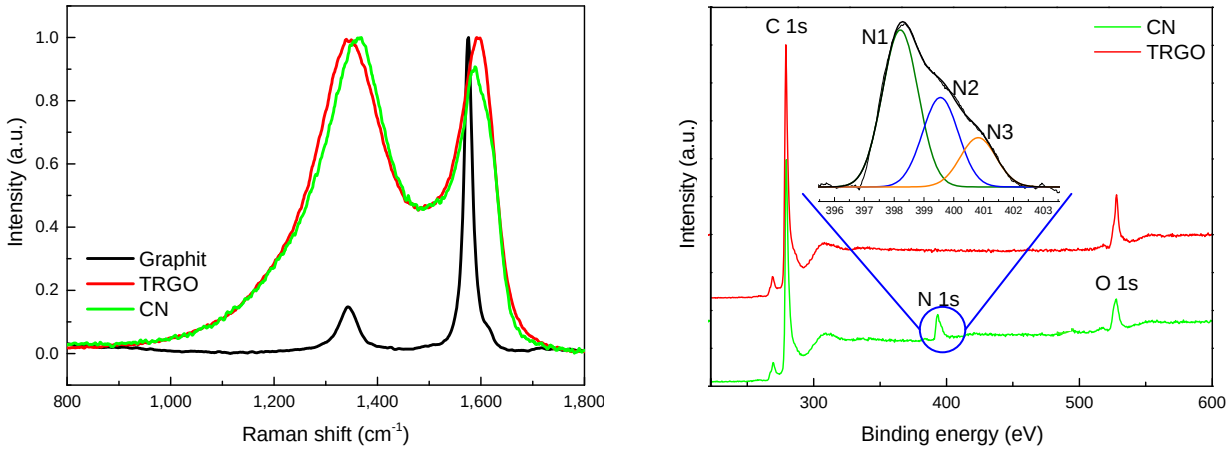

(a) (b)

Fig. 2 Raman spectra of graphite, graphene (TRGO) and nitrogen-doped graphene (CN): (a) XPS spectra of grapheme (TRGO) andnitrogen-doped graphene (CN); (b) the inset in (b) shows high resolution N1s XPS spectra of CN and deconvolution into specific peaks corresponding to several nitrogen functionalities, N1 refers to pyridinic N, N2 to pyrrolic N and N3 to graphitic N, respectively.

spectra is presented in the inset in Fig. 2b. The high-resolution N1s peaks can be ascribed to pyridinic (N1), pyrrolic (N2) and graphitic (N3) nitrogen functionalities, determined at 398.2 eV, 399.6 eV and 400.8 eV, respectively. Hence, the certain amount of specific nitrogen functionality in total N atoms of CN for pyridinic N1, pyrrolic N2 and graphitic N3 was 54%, 30% and 16%, respectively. The role of respective nitrogen functionalities in ORR process has been subject of controversial discussions about the active catalytic site in N-doped carbon materials. Theoretical and experimental studies have been carried out to examine the ORR mechanism in N-doped carbon materials proposing pyridinic-N and graphitic-N as main catalytic active sites for ORR [11, 13, 27, 28].

3.2 Electrochemical Characterization of TRGO and CN

The electrochemical properties of TRGO and CN were characterized via CV and LSV.

3.2.1 Electrocatalytic Reduction of Oxygen in Alkaline Solution

In order to confirm the electrocatalytic activity towards ORR, cyclic voltammetry and linear sweep voltammetry measurements were carried out in nitrogen- and oxygen-saturated alkaline electrolyte solution. CV measurements were first performed in nitrogen-saturated aqueous 0.1 M KOH solution. As shown in Fig. 3a, clear capacitive current background is identified within the CV. Afterwards, oxygen was introduced to the solution. The measured cyclic voltammograms, presented in Fig. 3b feature specific cathodic current peaks, thus, demonstrating the ORR performance of all samples in oxygen-saturated 0.1 M KOH solution. The highest value of current density among carbon-based materials is obtained for CN (-0.256 mA·cm^{-2}), followed by TRGO (0.175 mA·cm^{-2}) and GC (0.150 mA·cm^{-2}). Compared with GC (-250 mV), the onset potentials of TRGO (-175 mV) and CN (-160 mV) shift positively confirming better electrocatalytic activity towards ORR. Commercial PtC features positively shifted onset (-20 mV) potential and higher current density (0.285 mA·cm^{-2}) than CN.

In addition, LSV measurements were performed on a RDE (rotating-disk electrode) in oxygen-saturated 0.1 M KOH solution at a rotation rate of 1,600 rpm. The recorded linear sweep voltammograms, displayed in Fig. 3c, show that, CN has the most positive onset potential and highest current density among the carbon-based materials. The LSV observations accord

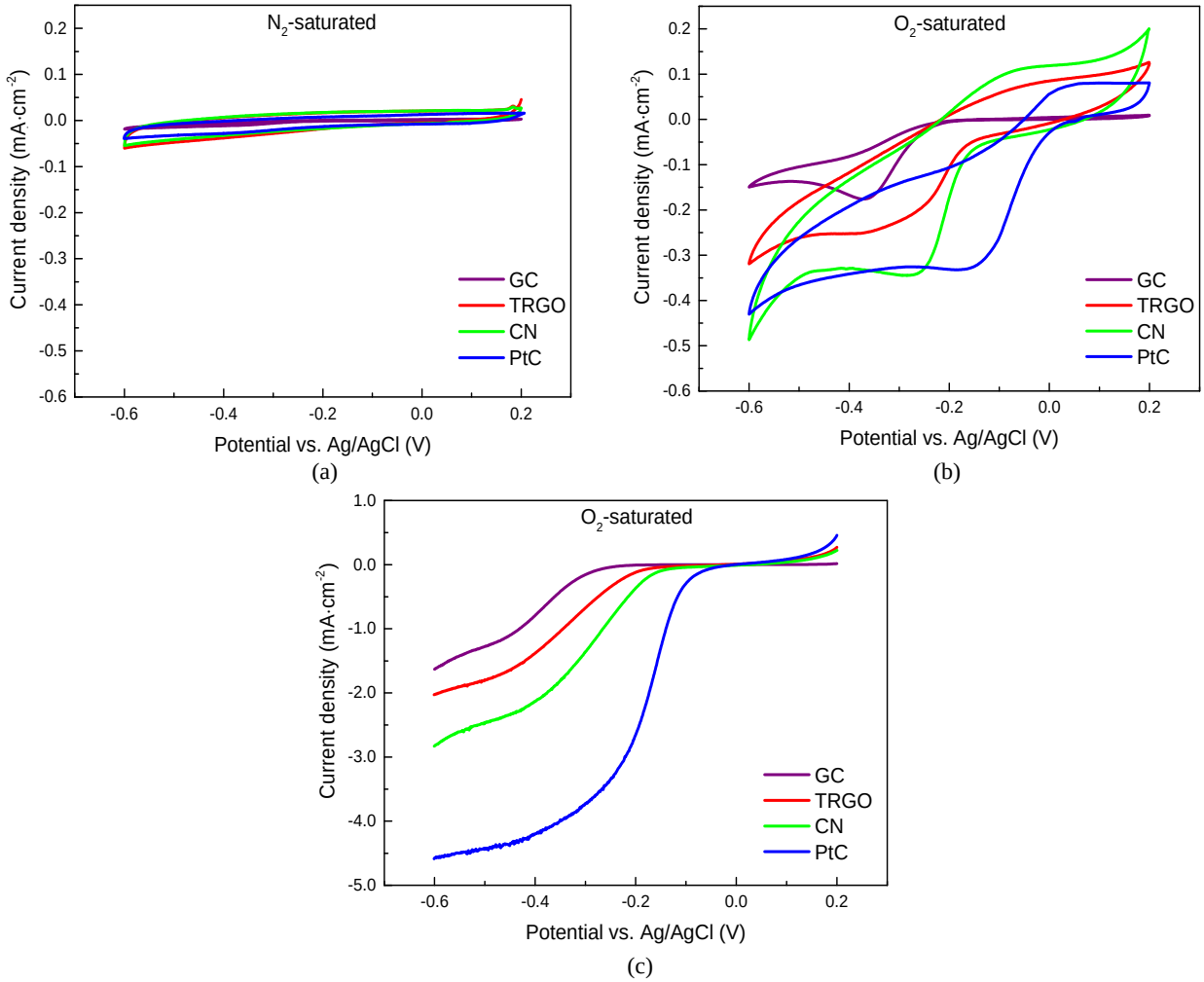

Fig. 3 CV-measurement of GC, TRGO, CN and commercial 20% PtC in aqueous 0.1 M KOH solution in (a) N_2-saturatedambience, and in (b) O_2-saturated ambience demonstrating electrocatalytic activity towards ORR. LSV measurements of GC, TRGO, CN and PtC in O_2—(c) saturated 0.1 M KOH solution at rotation speed of 1,600 rpm.

with the CV results and demonstrate that, the electrocatalytic activity of graphene towards ORR is enhanced by doping with nitrogen. It should be noted that, TRGO contains different oxygenated functional groups, mostly carboxylic and sulfonic acids. Remaining oxygenated functional groups at TRGO do not contribute to better ORR performance, as shown by performed comparative ORR measurements for different TRGO samples prepared at identical treatment temperature, i.e., 600 °C.

3.2.2 Mechanism of Oxygen Reduction on Nitrogen-Doped Graphene

The electron transfer mechanism of an electrocatalyst has to be investigated, to gain insight into the ORR kinetics. There are two possible oxygen reduction pathways in alkaline and acidic aqueous solutions, i.e., the direct four-electron pathway and the two-electron pathway, whereas hydrogen peroxide is produced as intermediate [29]. With regard to fuel cell applications, the efficient direct four-electron pathway proves to be the most beneficial due to the direct production of water. The investigation of the number of transferred electrons within oxygen reduction processes is also carried out at alkaline conditions. RDE measurements were performed at different rotation speeds from 400 rpm to 2,025 rpm in oxygen-saturated 0.1 M KOH solution. The K-L (Koutecky-Levich) equation and K-L plots were applied to determine the number of the

transferred electrons [30].

LSV curves of PtC and CN, shown in Figs. 4a and 4c, demonstrate increasing current density with higher rotation speeds which is caused by shorter diffusion distances at higher speeds. Figs. 4b and 4d present the K-L plots, applied to evaluate the electron transfer process at N-doped graphene and PtC. The relationship between j^{-1} and $w^{-1/2}$ is clearly linear from -0.4 V to -0.8 V. Hence, the number of transferred electrons (n) at certain potentials was determined from the slope of the K-L plots. As expected, the oxygen reduction on PtC is dominated by the direct four-electron pathway, since n was calculated to be constantly 4.0 for the whole region between -0.4 V and -0.8 V (Fig. 4b). For CN1000, n was calculated to be 3.1 at -0.4 V and 3.9 at -0.8 V (Fig. 4d). It can therefore be concluded that, the oxygen reduction on N-doped graphene at alkaline conditions involves both the two-electron pathway and the four-electron pathway. With increasing voltage the four-electron pathway is gaining in significance. The results imply that, the reduction process of oxygen on N-doped graphene rather follows the four-electron transfer mechanism defined for alkaline conditions producing four OH^- groups and not the transfer mechanism typical for acidic conditions where H^+ participates in ORR [29].

3.2.3 Sensitivity towards Methanol Oxidation and Long-Term Operation Stability

Long-term stability and crossover effects play a crucial role in terms of fuel cell applications. In view of

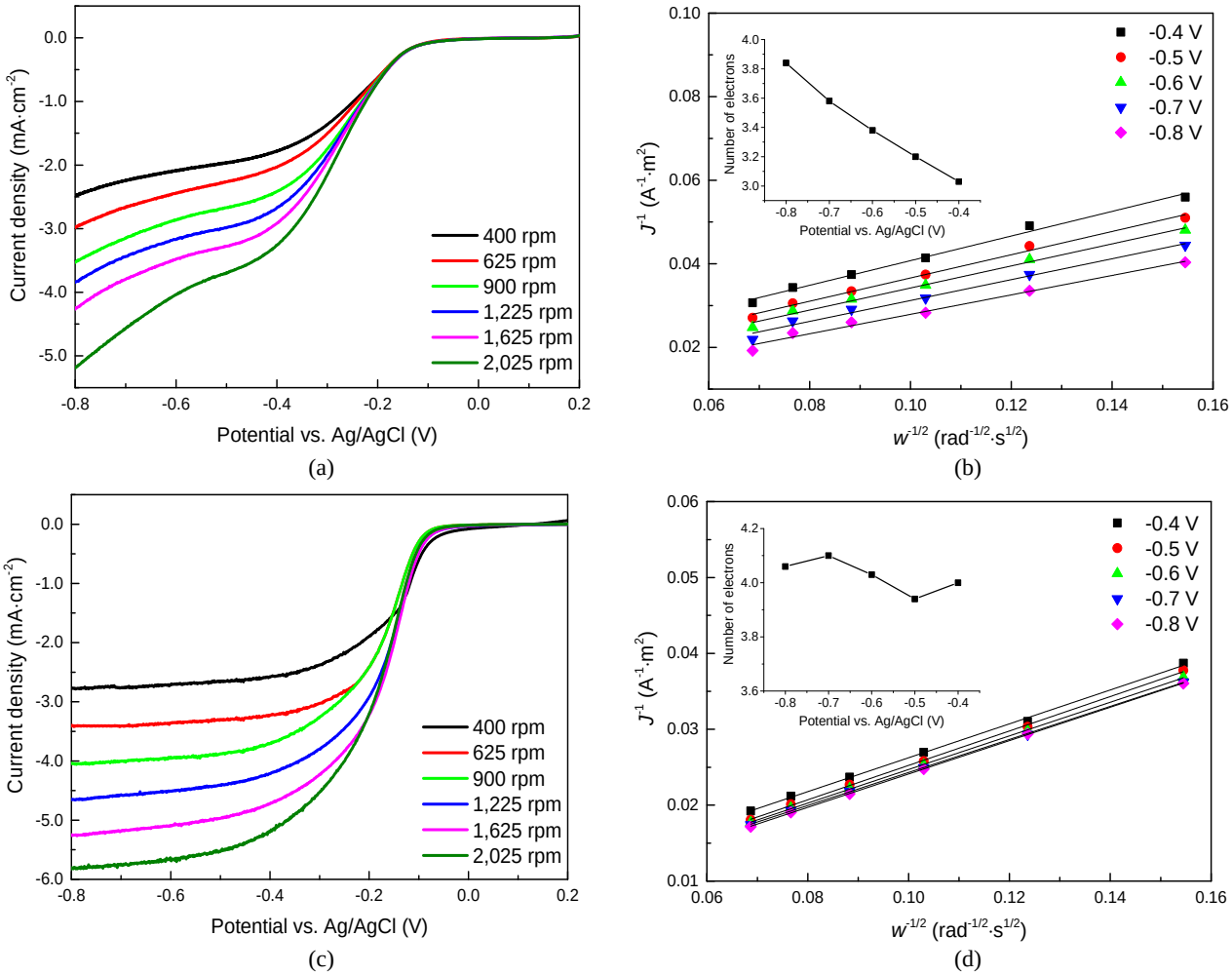

Fig. 4 Set of LSV curves for (a) CN and (c) 20% PtC recorded at alkaline conditions, i.e., in O_2-saturated 0.1 M KOH solution at various rotation velocities with a scan rate of 5 mV·s^{-1}. K-L plots for (b) CN1000 and (d) 20% PtC at different cathodic potentials. The numbers of transferred electrons at the respective potentials are shown in the insets in (b) and (d).

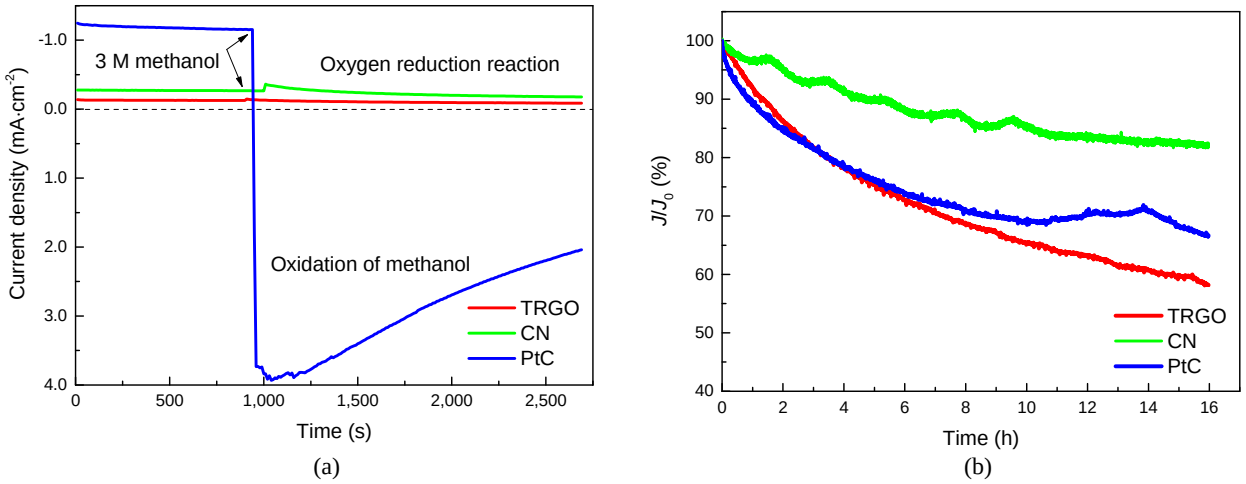

Fig. 5 ORR current-time responses at (a) TRGO, CN and PtC electrodes in O_2-saturated 0.1 M KOH solution, before and after the addition of 3 M methanol indicated by arrows. Long-term operation stability test, relative current-time responses for 16 h at (b) TRGO, CN and PtC electrodes in air-saturated 0.1 M KOH solution. All measurements are performed at rotation speed of 1,600 rpm.

a potential application in direct methanol alkaline fuel cells, prepared graphene and nitrogen-doped graphene were electrochemically characterized in presence of methanol as fuel molecule, in order to investigate a possible crossover effect. Moreover, the long-term stability of prepared materials in alkaline media was investigated. The long-term stability of TRGO and CN was preliminarily characterized by repetitive potential cycling, whereat 2,500 CV cycles were performed consecutively between -1.0 V and 0 V in 0.1 M KOH, saturated with oxygen. After the repetitive potential cycling, the CVs have not shown any significant decrease in current and shape.

The electrocatalytic selectivity of TRGO and CN against the oxidation of methanol was characterized via chronoamperometry in oxygen-saturated 0.1 M KOH solution at -0.25 V with the rotation rate of 1,600 rpm. The same procedure was applied for PtC catalyst due to comparison matters. The current-time chronoamperometric responses of TRGO, CN and PtC are displayed in Fig. 5a. After adding 3 M methanol to the alkaline electrolyte solution, PtC suffers a keen positive shift of current density which can be attributed to the oxidation of methanol by PtC as shown in Fig. 5a. In contrast, the chronoamperometric responses of TRGO and CN change slightly upon the addition of 3 M methanol and the oxygen reduction reaction at the respective graphene-based electrode remains stable. Thus, prepared TRGO and CN are characterized by excellent immunity against methanol crossover effect.

The long-term operation stability of prepared graphene-based materials and PtC was further characterized by the same chronoamperometric test over a longer period of time, whereas current-time response of each sample was recorded over 16 h. The corresponding chronoamperometric responses of TRGO, CN and PtC are shown in Fig. 5b. A comparison of the current-time responses shows that, CN is characterized by best durability among investigated materials. After 16 h, the relative current density of CN was still about 85%, while, the relative current density of TRGO decreased to approximately 58% and the relative current density of PtC continuously decreased to about 66%. These results suggest that, the incorporation of nitrogen atoms into carbon lattice enhances the long-term stability of graphene. The remaining oxygenated functional groups should be the cause for the operation instability of TRGO and CN in the long term. For CN, the operation instability effect is still less remarkable, since mentioned functional groups barely contribute to ORR performance. Besides, the current density of CN was

stabilized over time, while the current density of TRGO was gradually decreasing. It was already reported that, removing surface functional groups and oxygenated groups from the carbon surface improves stability of carbon-based electric double-layer capacitors [30]. Furthermore, the results indicate the insufficient long-term stability of PtC which is generally known for platinum-based materials.

Summing up, the addition of methanol has a negative impact on the performance of PtC shifting the negative cathodic peak related to ORR to positive current ascribed to electrooxidation of methanol. In contrast, TRGO and CN are remarkably immune against methanol crossover effect as compared to PtC in alkaline medium. Hence, methanol does not interfere with the oxygen reduction reaction at a potential graphene-based cathode. In terms of durability in alkaline medium, prepared CN clearly possesses better long-term operation stability than prepared TRGO and commercial PtC electrocatalyst. Again, the electrocatalytic ORR activity of CN is enhanced by nitrogen doping. Owing to these outstanding characteristics, prepared nitrogen-doped graphene by mentioned novel synthesis procedure is perfectly suitable for application as cathode material in direct methanol alkaline fuel cells.

4. Conclusions

In this paper, nitrogen-doped graphene was successfully prepared by novel synthesis procedure based on thermal reduction of graphite oxide and subsequent treatment with cyanamide. Specifically, the novel aspect of this work consists in the use of liquid cyanamide as nitrogen-precursor offering an easily manageable synthesis approach. We have determined by Raman spectroscopy a comparable defect density for both graphene and nitrogen-doped graphene. The distinct D bands in graphene and nitrogen-doped graphene indicate the high level of defects in prepared materials. The successful doping process of nitrogen in carbon lattice is evidenced by X-ray photoelectron spectroscopy. In particular, pyridinic, pyrollic and graphitic nitrogen functionalities were identified in carbon lattice of prepared nitrogen-doped graphene.

As shown by experimental results, prepared graphene and nitrogen-doped graphene have proven their electrocatalytic activity towards oxygen reduction reaction. Considered together with the results of structural characterization, we estimate a major importance of nitrogen doping for enhancing the ORR performance. Both graphene and nitrogen-doped graphene are highly resistant to methanol crossover. Nitrogen-doped graphene particularly exceeds commercial 20% PtC catalyst in immunity against methanol crossover and long-term operation stability, thus, representing a promising metal-free electrocatalyst as cathode in alkaline fuel cell applications or micro fuel cells. The existing printing-based fabrication techniques of graphene materials provide favorable alternatives to conventional methods enabling clean, low-cost and facile large-scale production of nitrogen-doped graphene for electrochemical energy conversion.

Acknowledgments

We gratefully acknowledge the German Research Association (Deutsche Forschungsgesellschaft) for supporting this work within the framework of the Research Training Group “Micro Energy Harvesting” (Graduiertenkolleg 1322).

References

[1] Winter, M., and Brodd, R. J. 2004. “What Are Batteries, Fuel Cells and Supercapacitors?” *Chem. Rev.* 104 (10): 4245-70.

[2] Gasteiger, H. A., Kocha, S. S., Sompalli, B., and Wagner, F. T. 2005. “Activity Benchmarks and Requirements for Pt, Pt-Alloy, and Non-Pt Oxygen Reduction Catalysts for PEMFCs.” *Applied Catalysis B: Environmental* 56 (1-2): 9-35.

[3] Wang, B. 2005. “Recent Development of Non-platinum Catalysts for Oxygen Reduction Reaction.” *Journal of Power Sources* 152 (1): 1-15.

[4] Zhu, C., and Dong, S. 2013. “Recent Progress in Graphene-Based Nanomaterials as Advanced

Electrocatalysts towards Oxygen Reduction Reaction." *Nanoscale* 5 (5): 1753-67.

[5] Dreyer, D. R., Park, S., Bielawski, C. W., and Ruoff, R. S. 2010. "The Chemistry of Graphene Oxide." *Chemical Society Reviews* 39 (1): 228-40.

[6] Li, Y., and Wu, Y. 2009. "Coassembly of Graphene Oxide and Nanowires for Large-Area Nanowire Alignment." *J. Am. Chem. Soc.* 131 (16): 5851-7.

[7] Balandin, A. A., Ghosh, S., Bao, W., Calizo, I., Teweldebrhan, D., Miao, F., and Lau, C. N. 2008. "Superior Thermal Conductivity of Single-Layer Graphene." *Nano Lett.* 8 (3): 902-7.

[8] Novoselov, K. S., Geim, A. K., Morozov, S. V., Jiang, D., Katsnelson, M. I., Grigorieva, I. V., Dubonos, S. V., and Firsov, A. A. 2005. "Two-Dimensional Gas of Massless Dirac Fermions in Graphene." *Nature* 438 (7065): 197-200.

[9] Meyer, J. C., Geim, A. K., Katsnelson, M. I., Novoselov, K. S., Booth, T. J., and Roth, S. 2007. "The Structure of Suspended Graphene Sheets." *Nature* 446 (7131): 60-3.

[10] Stankovich, S., Dikin, D. A., Dommett, G. H. B., Kohlhaas, K. M., Zimney, E. J., Stach, E. A., Piner, R. D., Nguyen, S. T., and Ruoff, R. S. 2006. "Graphene-Based Composite Materials." *Nature* 442 (7100): 282-6.

[11] Qu, L., Liu, Y., Baek, J. B., and Dai, L. 2010. "Nitrogen-Doped Graphene as Efficient Metal-Free Electrocatalyst for Oxygen Reduction in Fuel Cells." *ACS Nano* 4 (3): 1321-6.

[12] Liang, J., Jiao, Y., Jaroniec, M., and Qiao, S. Z. 2012. "Sulfur and Nitrogen Dual-Doped Mesoporous Graphene Electrocatalyst for Oxygen Reduction with Synergistically Enhanced Performance." *Angewandte Chemie* 51 (46): 11496-500.

[13] Gong, K., Du, F., Xia, Z., Durstock, M., and Dai, L. 2009. "Nitrogen-Doped Carbon Nanotube Arrays with High Electrocatalytic Activity for Oxygen Reduction." *Science* 323 (5915): 760-4.

[14] Tang, Y., Allen, B. L., Kauffman, D. R., and Star, A. 2009. "Electrocatalytic Activity of Nitrogen-Doped Carbon Nanotube Cups." *J. Am. Chem. Soc.* 131 (37): 13200-1.

[15] Wang, H., Maiyalagan, T., and Wang, X. 2012. "Review on Recent Progress in Nitrogen-Doped Graphene: Synthesis, Characterization, and Its Potential Applications." *ACS Catal.* 2 (5): 781-94.

[16] Geng, D., Chen, Y., Chen, Y., Li, Y., Li, R., Sun, X., Ye, S., and Knights, S. 2011. "High Oxygen-Reduction Activity and Durability of Nitrogen-Doped Graphene." *Energy Environ. Sci.* 4 (3): 760.

[17] Pan, F., Jin, J., Fu, X., Liu, Q., and Zhang, J. 2013. "Advanced Oxygen Reduction Electrocatalyst Based on Nitrogen-Doped Graphene Derived from Edible Sugar and Urea." *ACS Applied Materials & Interfaces* 5 (21): 11108-14.

[18] Shao, Y., Zhang, S., Engelhard, M. H., Li, G., Shao, G., Wang, Y., Liu, J., Aksay, I. A., and Lin, Y. 2010. "Nitrogen-Doped Graphene and Its Electrochemical Applications." *J. Mater. Chem.* 20 (35): 7491.

[19] Novoselov, K. S., Geim, A. K., Morozov, S. V., Jiang, D., Zhang, Y., Dubonos, S. V., Grigorieva, I. V., and Firsov, A. A. 2004. "Electric Field Effect in Atomically Thin Carbon Films." *Science* 306 (5696): 666-9.

[20] Berger, C., Song, Z., Li, T., Li, X., Ogbazghi, A. Y., Feng, R., Dai, Z., Marchenkov, A. N., Conrad, E. H., First, P. N., and de Heer, W. A. 2004. "Ultrathin Epitaxial Graphite: 2D Electron Gas Properties and a Route toward Graphene-Based Nanoelectronics." *J. Phys. Chem. B* 108 (52): 19912-6.

[21] Kim, K. S., Zhao, Y., Jang, H., Lee, S. Y., Kim, J. M., Kim, K. S., Ahn, J. H., Kim, P., Choi, J. Y., and Hong, B. H. 2009. "Large-Scale Pattern Growth of Graphene Films for Stretchable Transparent Electrodes." *Nature* 457 (7230): 706-10.

[22] Tölle, F. J., Fabritius, M., and Mülhaupt, R. 2012. "Emulsifier-Free Graphene Dispersions with High Graphene Content for Printed Electronics and Freestanding Graphene Films." *Adv. Funct. Mater.* 22 (6): 1136-44.

[23] Tschoppe, K., Beckert, F., Beckert, M., and Mülhaupt, R. 2014. "Thermally Reduced Graphite Oxide and Mechanochemically Functionalized Graphene as Functional Fillers for Epoxy Nanocomposites." *Macromol. Mater. Eng.* 2 (300): 140-52.

[24] Tuinstra, F. 1970. "Raman Spectrum of Graphite." *J. Chem. Phys.* 53 (3): 1126.

[25] Kudin, K. N., Ozbas, B., Schniepp, H. C., Prud'homme, R. K., Aksay, I. A., and Car, R. 2008. "Raman Spectra of Graphite Oxide and Functionalized Graphene Sheets." *Nano Lett.* 8 (1): 36-41.

[26] Dresselhaus, M. S., Jorio, A., Hofmann, M., Dresselhaus, G., and Saito, R. 2010. "Perspectives on Carbon Nanotubes and Graphene Raman Spectroscopy." *Nano Lett.* 10 (3): 751-8.

[27] Kurak, K. A., and Anderson, A. B. 2009. "Nitrogen-Treated Graphite and Oxygen Electroreduction on Pyridinic Edge Sites." *J. Phys. Chem. C* 113 (16): 6730-4.

[28] Ikeda, T., Boero, M., Huang, S. F., Terakura, K., Oshima, M., and Ozaki, J. 2008. "Carbon Alloy Catalysts: Active Sites for Oxygen Reduction Reaction." *J. Phys. Chem. C* 112 (38): 14706-9.

[29] Zhang, J. 2008. *PEM Fuel Cell Electrocatalysts and Catalyst Layers.* London: Springer London.

[30] Bard, A. J., and Faulkner, L. R. 2001. *Electrochemical Methods: Fundamentals and Applications.* New York: Wiley.

Journal of Energy and Power Engineering 9 (2015) 896-904
doi: 10.17265/1934-8975/2015.010.008

Transient Stability Analysis of Power System with Photovoltaic Systems Installed

Masaki Yagami[1], Seiichiro Ishikawa[1], Yoshihiro Ichinohe[1], Kenji Misawa[1] and Junji Tamura[2]

1. Department of Electrical and Electronic Engineering, Hokkaido University of Science, Sapporo 006-8585, Japan

2. Department of Electrical and Electronic Engineering, Kitami Institute of Technology, Kitami 090-8507, Japan

Received: August 27, 2015 / Accepted: September 14, 2015 / Published: October 31, 2015.

Abstract: The impact of large-scale grid-connected PV (photovoltaics) on power system transient stability is discussed in this paper. In response to an increase of PV capacity, the capacity of conventional synchronous generator needs to be reduced relatively. This leads to the lower system inertia and the higher generator reactance, and hence, the power system transient stability may negatively be affected. In particular, the impact on the transient stability may become more serious when the considerable amounts of PV systems are disconnected simultaneously during voltage sag. In this work, the potential impact of significant PV penetration on the transient stability is assessed by a numerical simulation using PSCAD/EMTDC.

Key words: Photovoltaic, LVRT (low-voltage ride-through), synchronous generator, infinite bus, transient stability.

1. Introduction

With the increasing concerns about global warming, the amount of solar PV (photovoltaic) installations is growing worldwide. In particular, in Japan, the investment in the field of PV power generation has been increasing after the Fukushima nuclear power plant accident. During 2013, a total of 6.9 GW of PV was installed in Japan, 400% increase beyond the installation in the previous year (1.7 GW). Cumulative installed capacity of PV systems in 2013 reached 13.6 GW [1]. Japan introduced a feed-in tariff scheme for renewable energy in July, 2012. The PV market, therefore, is expected to continue growing significantly. However, the expanding installation of PV has a significant impact on the power system behavior.

With the increasing of PV capacity in the power system, several thermal power plants need to be closed down or at least the output power of thermal unit must be decreased in order to maintain power supply-demand balance. However, as the generator operation with low output leads to an increase in operating costs, reduction of the generator capacity would mainly be taken. As a result, the transient stability would negatively be affected due to the lower system inertia and the higher generator reactance. On the other hand, when a fault occurs in the power system, some parts of PV systems may be disconnected from the grid due to the voltage sag. The disconnection causes a drop in PV generation, and hence a further voltage drop in the grid system may be induced. Eventually, the considerable amounts of PV systems may be disconnected from the grid. In this case, not only the transient stability would be affected, but also the frequency stability would significantly be affected due to the large power imbalance and the fewer frequency control generators. In order to prevent the frequency drop, power system operators would require PV systems to be equipped with LVRT (low-voltage ride through) capability. LVRT requirements stipulate that PV needs to stay connected during a temporary fault to provide post-fault voltage support [2].

Corresponding author: Masaki Yagami, Ph.D., associate professor, research fields: power system stability and FACTS (flexible AC transmission system). E-mail: yagami@hus.ac.jp.

In this paper, the impact of large-scale grid-connected PV with or without LVRT capability on the power system transient stability is discussed based on the numerical simulation analysis using PSCAD/EMTDC software. The salient feature of this work is that, the transient stability analysis is carried out for two power system models with and without infinite bus respectively. Namely, PV systems connected with a large power system with an infinite bus or a comparatively small system without an infinite bus are considered in the transient stability simulation. In the near future, the disconnection of GW-scale PV system will be occurred. In large power system, the influence of loss of active power from PV on the transient stability may be small due to the sufficient power supply from other power source including infinite bus. On the other hand, in small power system, the synchronous generator may be subjected to large decelerating power when PV is disconnected, and hence, in extreme cases, the generators may go to out-of-step in decelerating direction.

Although there are some studies relating to the stability analysis using the power system model with infinite bus and PV system [3-5], few studies has focused on the influence of infinite bus on the transient stability. As the transient stability is mainly an instantaneous energy balance problem, it is important to consider the influence of the existence of LVRT capability and infinite bus on the transient stability.

The paper is organized as follows: Section 2 describes the simulation model; Section 3 presents the simulation results and discussions; Section 4 gives conclusions.

2. Simulation Model

2.1 Power System Model

Fig. 1 shows 9-bus power system model [6] used in the simulation analysis, which is composed of three power sources, one synchronous generator of 500 MVA (SG1), an infinite bus or another synchronous generator of 500 MVA (SG2), and a large-scale PV plant of 500 MW (PV) or a third synchronous

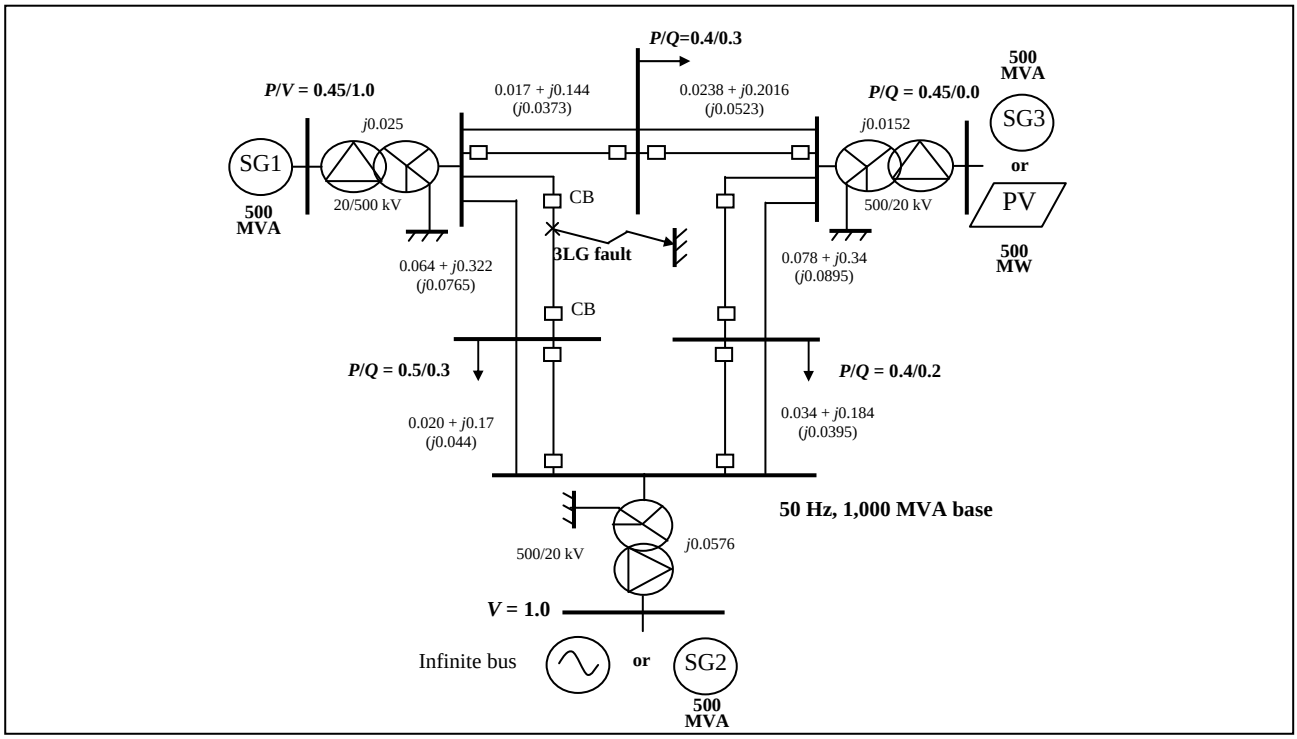

Fig. 1 Power system model.

Table 1 Synchronous generator parameters.

Generator parameters					
	SG1	SG2 SG3		SG1	SG2 SG3
R_a (pu)	0.003	0.004	X_q" (pu)	0.171	0.134
X_l (pu)	0.102	0.078	T_{do}' (s)	5.9	8.97
X_d (pu)	1.651	1.22	T_{qo}' (s)	0.535	1.5
X_q (pu)	1.59	1.16	T_{do}" (s)	0.033	0.033
X_d' (pu)	0.232	0.174	T_{qo}" (s)	0.078	0.141
X_q' (pu)	0.38	0.25	H (s)	3.0	3.0
X_d" (pu)	0.171	0.134			

generator of 500 MVA (SG3). Each power source is connected through step up transformer to 500 kV bus and double circuit transmission lines. The impedances and the initial power flows are shown in per unit values on the power system base of 1,000 MVA in Fig. 1. In the case with PV installed, the existence of LVRT capability is considered for PV inverter. LVRT characteristic considered in this work is simple. The PV inverter with LVRT capability maintains the connection to the grid even if its terminal voltage is dropped. On the other hand, the PV inverter without LVRT capability is disconnected from the grid when its terminal voltage drops below 70% of the nominal voltage [7], and the disconnection is maintained for remaining period of the simulation.

The parameters used for each synchronous generator are shown in Table 1. AVR (automatic voltage regulator) [8] and governor control systems shown in Fig. 2 have also been included in each generator model.

In the power system model, symmetrical 3LG (three-line-to-ground) fault is assumed as network disturbance. The fault occurs near SG1 at 0.1 s, the CBs (circuit breakers) on the faulted lines are opened at 0.17 s, and at 1.17 s, they are reclosed. For 500 kV transmission lines in Japan, reclosing with a fixed time interval of 50 cycles (i.e., 1.0 s for 50 Hz system) has been adopted.

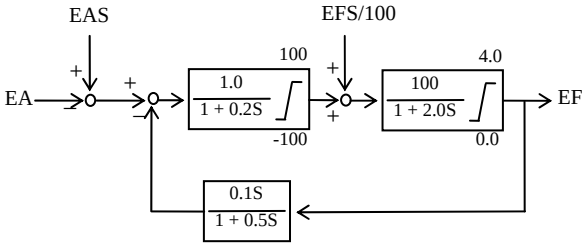

EA: terminal voltage; EAS: terminal voltage reference;
EF: field voltage; EFS: field voltage reference

(a) AVR

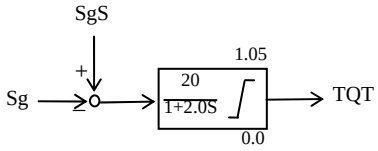

Sg: generator speed SgS: generator speed reference
TQT: turbine torque

(b) Governor

Fig. 2 AVR and governor models.

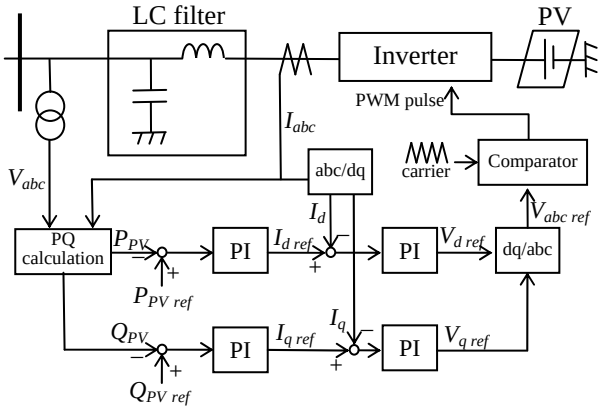

Fig. 3 Control block diagram of PV inverter.

2.2 PV System Model

The PV system model is shown in Fig. 3. It consists of PV module, inverter and LC (low-pass) filter. The PV module is represented with a voltage source, and hence the PV output is constant under the steady state. This means irradiation and PV cell temperature are

constant during the simulation period. In general, transient stability is analyzed in a time window of a few seconds to several tens of seconds. The assumption, therefore, may be valid for the transient stability analyses. The genetic PWM (pulse-width modulation) voltage source converter is used as PV inverter. The carrier frequency is 10 kHz. The inverter controls the active and reactive power injected from the PV module to the system. To maintain the active and reactive power at the reference set points, the currents of the inverter are controlled by using vector control technique. The current limitation for over current is not considered in this model. Currently, most of the PV inverters are designed to operate at unity power factor [7], and therefore the reference value of the reactive power is set to zero in each case.

3. Simulation Results

3.1 Stability of Power System with Infinite Bus

First, the transient stability of the power system with infinite bus is discussed. Fig. 4 shows the phase angle responses of SG1. To compare the effects of the conventional synchronous generator and PV system on transient stability, we have considered three simulation conditions in terms of the power sources as follows: (1) connecting SG3 instead of PV, (2) connecting PV without LVRT capability, and (3) connecting PV with LVRT capability. As can be seen, the first peak of the phase angle swing is decreased in the case of PV without LVRT. In other words, risk of out-of-step of the synchronous generator becomes low in the power system installed with PV without LVRT.

Fig. 5 shows the kinetic energy responses of SG1. As can be seen, in the case with PV without LVRT implemented, the kinetic energy stored in the rotor of SG1 can be released quickly compared with other cases. PV without LVRT is disconnected from the grid due to the voltage sag when the fault occurs. The disconnection of PV increases the power load of SG1, and hence the output power of SG1 is enlarged. On the other hand, as the prime-mover mechanical power

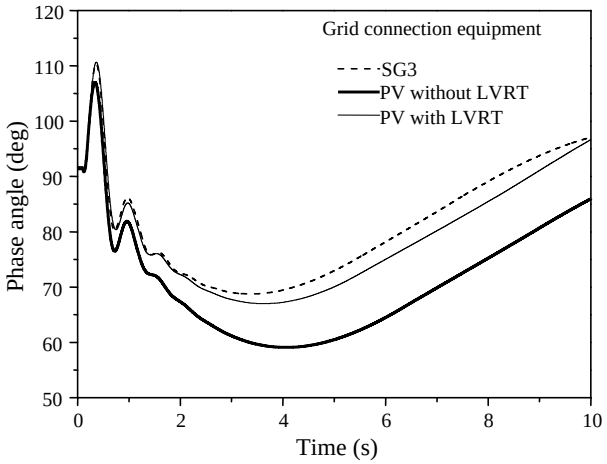

Fig. 4 Phase angle of SG1 (with infinite bus).

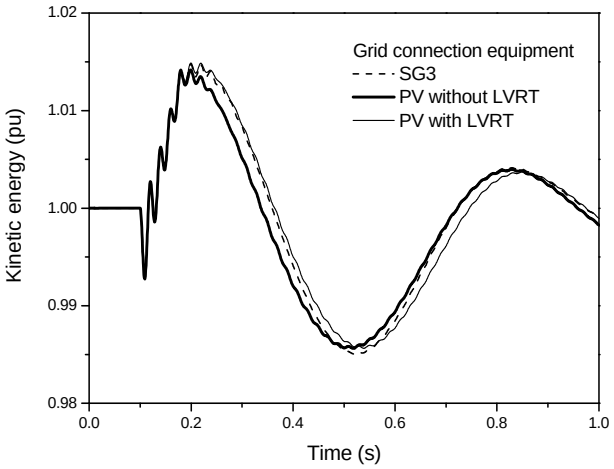

Fig. 5 Kinetic energy of SG1 (with infinite bus).

of SG1 cannot be increased quickly, the output power of SG1 is supplied from the kinetic energy which is stored during the period of acceleration. The kinetic energy stored in the rotor is released quickly, and hence the swings of the phase angle and the kinetic energy are restrained in the case of PV without LVRT.

Fig. 6 shows the active power of each power source in the case with PV installed with or without LVRT implemented. In both cases, when the fault occurs, active powers of SG1 and PV decrease due to the voltage sag. On the other hand, the active power from infinite bus increases during the period of fault because the bus voltage is a constant. After the fault clearing, the active power of SG1 increases because the terminal voltage of SG1 is recovered. In the case with PV with LVRT implemented, the active power of

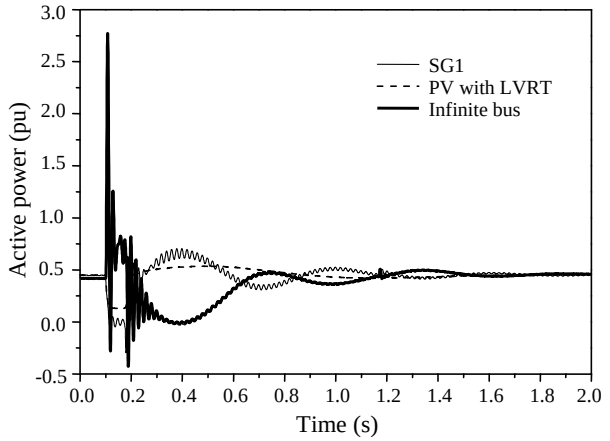

(a) PV with LVRT

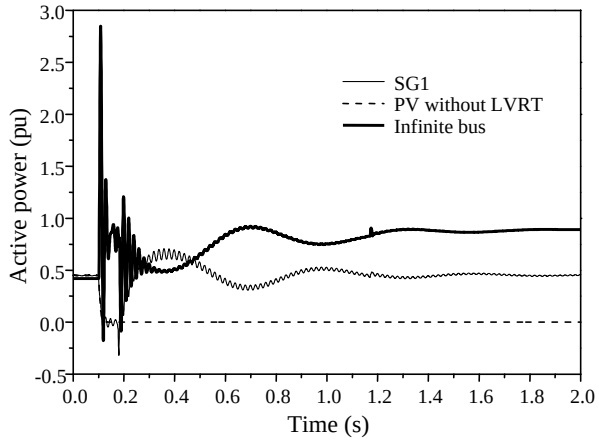

(b) PV without LVRT

Fig. 6 Active powers from SG1, PV and infinite bus in the case with PV with/without LVRT implemented (with infinite bus).

PV is also increased. To maintain power supply-demand balance, therefore, the active power from the infinite bus does not increase so much. The active power of each power source converges so as to approach to the value in steady state. On the other hand, in the case with PV without LVRT implemented, the active power of PV is maintained at 0 pu because PV without LVRT is disconnected from the grid due to the voltage sag. The power shortage caused by the disconnection of PV is covered by active powers of SG1 and infinite bus. However, as maximum value of output power of SG1 is restricted by a turbine load limiter, the active power from infinite bus gets extremely large. In small power system, the power shortage must only be covered by the active powers of power sources in the local network.

3.2 Stability of Power System without Infinite Bus

Next, the transient stability of the power system without infinite bus is discussed. The synchronous generator SG2 is connected with the grid instead of infinite bus. The initial power flow is the same with that of the case with infinite bus connected.

Fig. 7 shows the phase angle responses of SG1 and SG2. The phase angles shown are displacement angle with respect to the phase angle of the swing generator SG2. As can be seen, the first peak of the phase angle swing of SG1 in the case with PV with LVRT implemented is decreased more than those in other cases. On the other hand, the phase angle in the case with PV without LVRT implemented increases significantly, and then decreases toward 0 degrees. Fig. 8 shows the kinetic energy responses of each synchronous generator. As can be seen, in the case with PV without LVRT implemented, the kinetic energies of SG1 and SG2 decrease toward 0 pu. Namely, SG1 and SG2 go to out-of-step in the decelerating direction.

Figs. 9-11 show the responses of the active power, the reactive power, and the terminal voltage of each power source respectively. As can be seen in Figs. 9a and 9b, in the case with PV without LVRT implemented, the active powers of SG1 and SG2 rise up significantly after the fault clearing at 0.17 s. This is because to maintain the power supply-demand

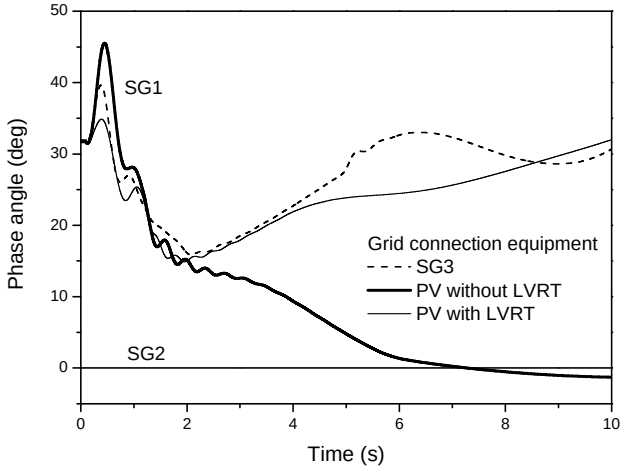

Fig. 7 Phase angles of SG1 and SG2 (without infinite bus).

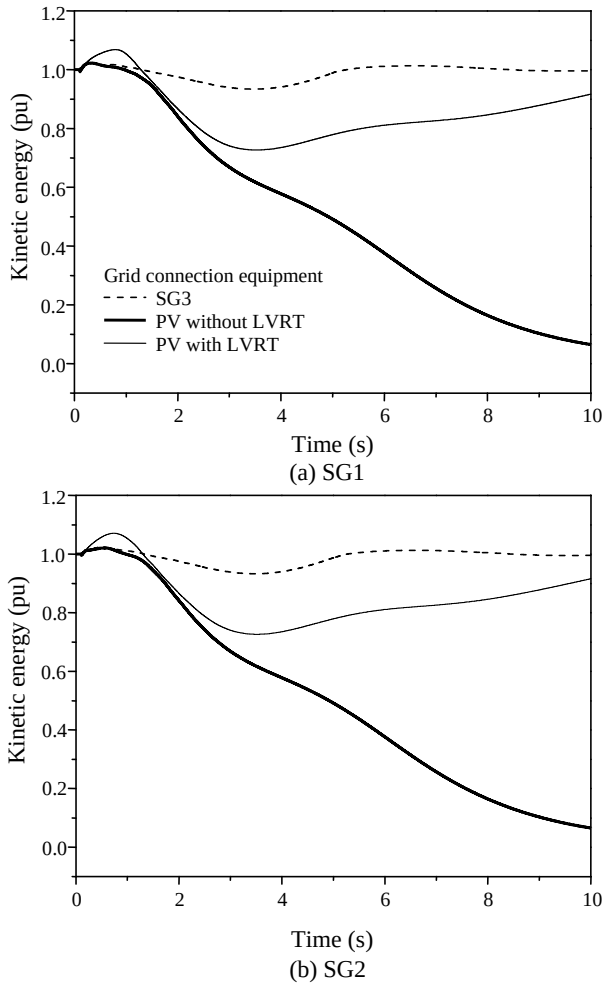

Fig. 8 Kinetic energies of SG1 and SG2 (without infinite bus).

balance after the disconnection of PV. However, as the prime-mover mechanical power of synchronous generator is restricted by the turbine load limiter, the rotor is subjected to a large decelerating power due to unbalance between the mechanical input power and the electrical output power. As a result, the kinetic energy stored in the rotor is extremely released, and hence the generator goes to out-of-step in the decelerating direction.

In the case of PV with LVRT, the active powers of SG1 and SG2 also rise up significantly after the fault clearing because the active power of PV is temporarily decreased at around 1.5 s. However, SG1 and SG2 do not go out-of-step because the power supply from PV is maintained after the fault.

PV inverter is controlled to maintain both active and reactive power at the reference set points. As a result, the large current flows from PV to the grid when the terminal voltage drops due to the fault. Therefore, as seen in Fig. 9c, the active power from PV becomes very large when the terminal voltage of PV is recovered by clearing the fault. In addition, as the reactive power from PV with LVRT increases around 1.0 s as seen in Fig 10c, the terminal voltage of PV also increases as seen in Fig. 11c. As a result, the active power from PV increases significantly around this time. To maintain the power supply-demand balance, the active powers of SG1 and SG2 after the fault clearing is maintained at low values until about 1.0 s. As a result, a large amount of kinetic energy is stored in the rotor, and hence the synchronous generators of SG1 and SG2 accelerate more than those of the case with SG3 installed.

As can be seen in Fig. 8, in the case of PV with LVRT implemented, the kinetic energies of SG1 and SG2 rise up significantly after the fault. As mentioned earlier, this is because the generator output after the fault clearing cannot be enlarged due to the active power from PV with LVRT. As seen in Fig. 7, the phase angle swing of SG1 in the case with PV with LVRT implemented is restrained significantly. Namely, the risk of out-of-step of the synchronous generator becomes low in the power system with PV with LVRT implemented. However, acceleration or deceleration of the rotor causes severe mechanical stresses. Therefore, in order to release quickly the kinetic energy stored in the rotor, it might be worth changing the control mode of PV inverter to constant voltage control. If PV supplies a sufficient reactive power after the fault, the terminal voltage and the active power of the synchronous generator increase. Therefore, the synchronous generator may be subjected to the decelerating power due to unbalance between the mechanical input power and the electrical output power, and the kinetic energy deviation may be restrained.

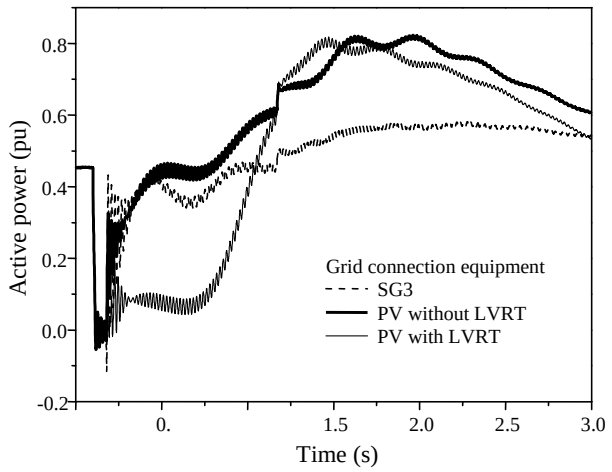

(a) SG1

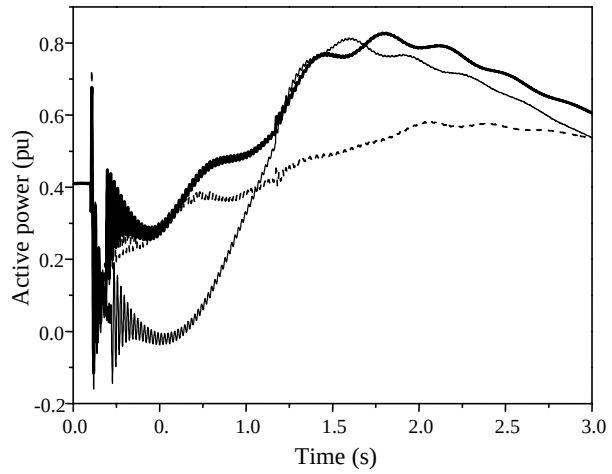

(b) SG2

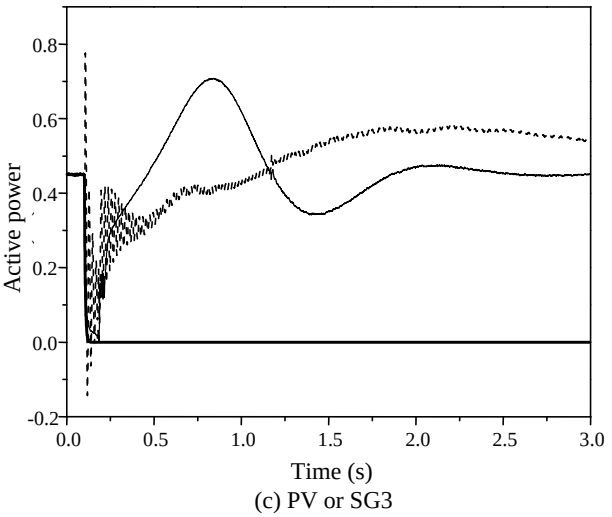

(c) PV or SG3

Fig. 9 Active powers from SG1, SG2 and PV or SG3 (without infinite bus).

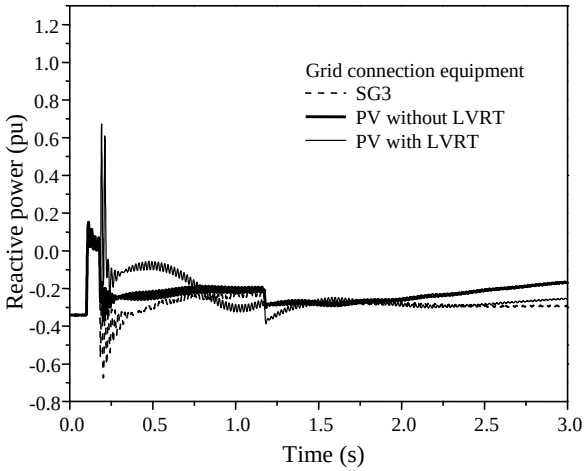

(a) SG1

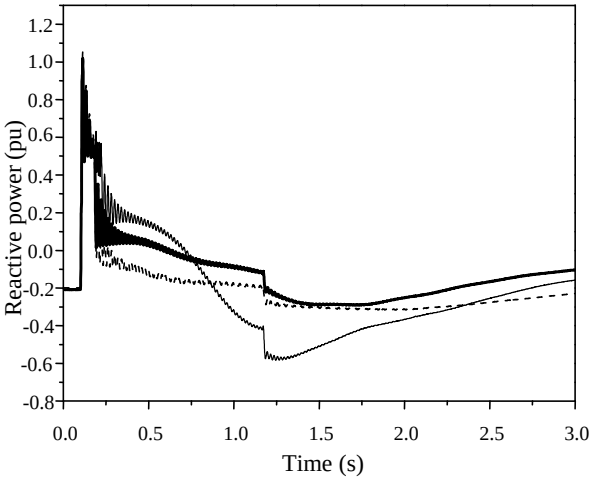

(b) SG2

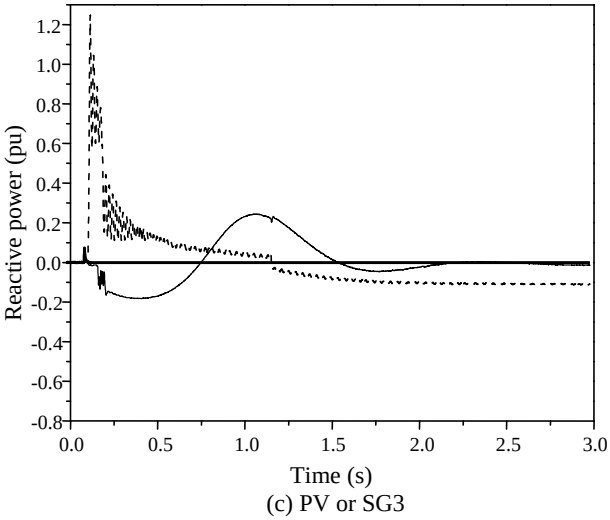

(c) PV or SG3

Fig. 10 Reactive powers of SG1, SG2 and PV or SG3 (without infinite bus).

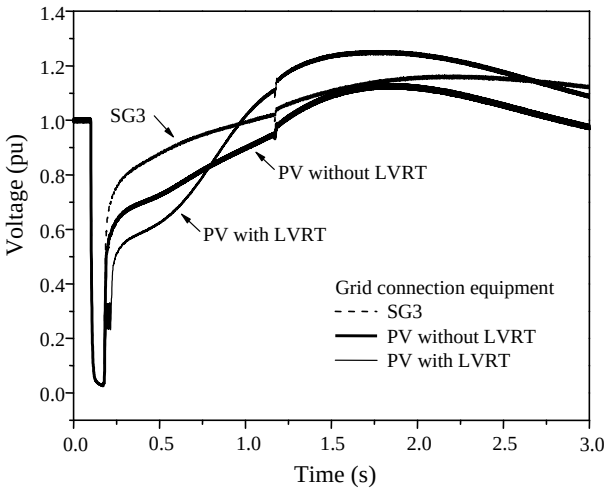

(a) SG1

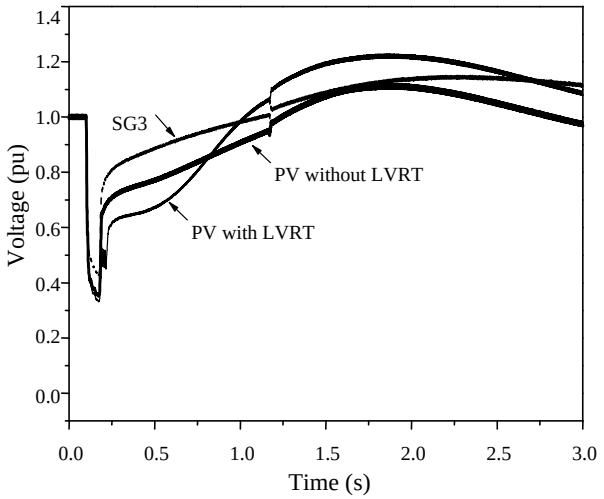

(b) SG2

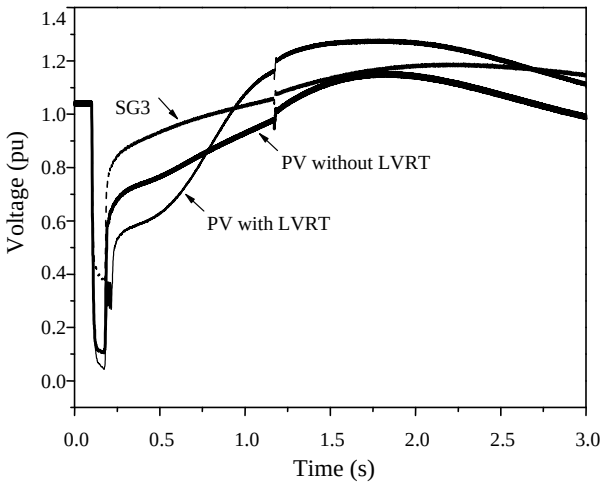

(c) PV or SG3

Fig. 11 Terminal voltages of SG1, SG2 and PV or SG3 (without infinite bus).

4. Conclusions

This paper presents a case study assessing the impact of high-penetration PV on the transient stability of power system. Simulation analyses have been carried out considering existence of LVRT capability of PV inverter and infinite bus in the power system model. Obtained results are summarized as follows:

(1) power system with infinite bus

PV system connected with a relatively large power system or small PV system compared to the power system capacity is assumed. Through the simulation results, it is concluded that the risk of out-of-step of the synchronous generator becomes low in the case that PV without LVRT capability is installed, because the disconnection of PV after the network disturbance increases the power load of the synchronous generator;

(2) power system without infinite bus

PV system connected with a relatively small power system or large PV system compared to the power system capacity is assumed. Through the simulation results, it is concluded that the risk of out-of-step of the synchronous generator becomes high in the case that PV without LVRT capability is installed. This is contrary conclusion with regard to (1). The disconnection of PV due to the voltage sag may lead to out-of-step of synchronous generators in decelerating direction.

Though PV with LVRT capability is installed in the grid system, it can be disconnected from the grid dependent on the condition of the voltage sag and grid fault. It is needless to say that, there is no infinite bus in real power systems. Therefore, it is very important to think about the transient stability and its enhancement for power systems with a huge amount of PV systems installed, for which the results in this paper can be the base.

Acknowledgments

This work was supported by research grant from

JSPS (Japan society for the promotion of science) KAKENHI Grant Number 24656179, 15H03956.

References

[1] Photovoltaic Power Systems Programme. 2014. *Trends 2014 in Photovoltaic Applications.* Report IEA-PVPS (International Energy Agency-Photovoltaic Power Systems Programme) T1-25.

[2] Keller, J., and Kroposki, B. 2010. *Understanding Fault Characteristics of Inverter-Based Distributed Energy Resources.* NREL (National Renewable Energy Laboratory) Technical report, NREL/TP-550-46698.

[3] Du, W., Wang, H. F., and Dunn, R. 2009. "Power System Small-Signal Oscillation Stability as Affected by Large-Scale PV Penetration." Presented at the International Conference on Sustainable Power Generation and Supply, Nanjing, China.

[4] Sakamoto, N., Taniguchi, H., Ota, Y., Nakajima, T., and Chinuki, T. 2012. "Transient Stability Study of One-Machine-to Infinite-Bus Power System under Large Penetration of PV Generation." *IEEJ Trans. PE* 132 (1): 9-15.

[5] Yagami, M., Hasegawa, T., and Tamura, J. 2012. "Transient Stability Assessment of Synchronous Generator in Power System with High-Penetration Photovoltaics." *Journal of Mechanics Engineering and Automation* 2 (12): 762-8.

[6] Anderson, P. M., and Fouad, A. A. 2003. *Power System Control and Stability.* Piscataway: A John Wiley & Sons, Inc., 38.

[7] Kobayashi, H., and Suzuki, A. 2010. *Stable Operation Technique for PCS of PV Power Generation at Grid Recovery after Voltage Sag.* System Engineering Research Laboratory, R09015.

[8] IEEJ Technical Committee. 1999. *Standard Models of Power System.* IEEJ Technical report 754.

0

Journal of Energy and Power Engineering 9 (2015) 905-911
doi: 10.17265/1934-8975/2015.010.009

Smart Meters and Under-Frequency Load Shedding

Krzysztof Billewicz

Department of Electrical Power Engineering, Wroclaw University of Technology, Wrocław PL-50-370, Poland

Received: August 24, 2015 / Accepted: September 14, 2015 / Published: October 31, 2015.

Abstract: In some countries, there exists a risk of power deficit in the EPS (electrical power system). This is a very serious problem and there are various solutions to deal with it. A power deficit in the EPS leads to frequency decrease in the power system. A dedicated automation to load shedding is used to maintain proper EPS operation. For some time, it has applied a mechanism called demand-side response, which in case of an emergency situation allows for a "more civilized" rationing of electricity to customers, with their consent. Such programs require that the utilities pay the customers for their agreement. The author proposes a new solution, intermediate between strict ALS (acting relieving automation) and demand-side response programs, where the companies have to send information about the price of energy or control signals to households.

Key words: Smart meter, smart grid, under-frequency, load shedding, electric power system.

Nomenclature

ALS	automatic load shedding
AMI	advanced metering infrastructure
AMR	automated meters reading
CPP	critical peak pricing
DLC	direct load control
DSO	distribution system operator
DSR	demand-side response
EPS	electric power system
HAN	home area network
ICR	interruptible/curtailable rates
ICT	information and communications technology
IHD	in-home display
LFC	load frequency control
RTP	real-time pricing
ToU	time-of-use pricing
TSO	transmission system operator
WAN	wide area network
$< f$	under-frequency
f_N	nominal frequency

1. Introduction

In some countries, there is a risk of power deficit in the EPS (electric power system). This is a very serious problem and there are various solutions that deal with this problem. A power deficit in the system leads to frequency decrease. Many years ago, preventive ALS (automatic load shedding) was developed. If the measurements indicate a frequency drop it automatically executes load decreasing. An automatic load shedding is categorized as one of the protection systems applied to the EPS.

Such automation is however a bad solution. Firstly, it usually completely shuts off the power to certain recipients, without their knowledge or consent. Secondly, it does not allow recipients to make selection which appliances could be shut off of power and those, that should still be supplied. Therefore, they have begun to use more civilized methods of energy rationing, in case of power deficit in the EPS. This is how demand-side response was developed, which, among others enables to perform certain rationing actions of energy supplies, with the consent of the end-users.

2. Power Balance and the Frequency

A balance between production and consumption of power at any given moment of time is indicated by the

Corresponding author: Krzysztof Billewicz, assistant professor, research fields: demand response, energy consumption, power market, demand side management, energy efficiency projects, data processing in metering, billing systems, cyber security and AMR/smart metering technology. E-mail: krzysztof.billewicz@pwr.edu.pl.

frequency of the power grid. In the steady state, power generated in power plants is equal to the power consumed by the end-users, plus transmission losses. In this situation, generator rotors rotate at a constant angular speed ω. If there is no power deficit in the power system, the frequency of the network in steady state is equal to the nominal frequency f_N, which is equal in Poland to $f_N = 50$ Hz.

Today, there is utilized a central frequency regulation in the power system. One common secondary frequency regulator is installed at the system operator plant. In case of a drop in grid frequency, the information about the drop is redirected to the central frequency regulator and this regulator takes actions to restore the nominal frequency of the power grid.

The increase in total active power demand causes grid frequency drop (generators speed), while the decrease in power consumption causes increase in the frequency. In the event of a change in power consumption, in order to maintain the system frequency within certain limits, a change in the amount of energy produced by generators or the amount of energy delivered to the power grid has to be made. In case of reduction of the power consumption by the customers, one can easily reduce the power supplied to the network through power stations. A problem may occur in situations of increased power demand. In such cases, it is necessary to start-up additional generators, which have a finite maximum power and cannot give more power into the power system. If there is no possibility of mobilizing additional generation capacity to maintain system stability and maintaining the frequency within certain limits, then load reduction is carried out.

If there will occur an increase in power demand and the power generation unit reaches its maximum power at the primary control, then it ceases to participate in the further adjustment of the frequency. In this case, its droop regulation becomes infinitely large, while the inclination of the frequency is equal to zero. In the event, when all power units will reach their maximum power capacity, the only possible response of the power system to the frequency reduction is to reduce the power load, depending on its frequency characteristic. To avoid such situation the power systems are using the spinning reserve, whose task is to ensure a proper operation of the primary frequency control.

It is worth noting that, the frequency drop is not a good indicator of a situation in the EPS. The frequency decreases when the system is overloaded or when adverse situations are already taking place. Dedicated automation does not affect the cause of the failure and it does not inform about the risk of its occurrence. Therefore, scientists and power engineers are looking for other indicators, which would determine the condition of the power system.

3. DSR (Demand-Side Response) Programs and Overload Protection

An implementation of many new DSR programs will be possible after the implementation of smart metering.

Such DSR programs, which are based on price signals, i.e., tariffs: ToU (time-of-use) and RTP (real-time pricing) cannot be used in real-time for security power system protection. These mechanisms are rather tools for shaping demand for energy in the long term. Thanks to them, some part of the energy consumption in residential sector is shifted to later periods (or reduced) from peak to off-peak hours [1-4].

Only the stimulus programs DSR, such as: ICR (interruptible/curtailable rates) and DLC (direct load control), whose use is associated with real possibility of partial reduction of energy consumption and load control by the network operator can contribute, in a real-time, to protect the power system from overloading.

A smart meter can directly control the household appliances. You can also find solutions, which assume sending of control signals through the smart meter into the HAN (home area network) controller. This

controller controls the work of intelligent home appliances, based on the received information about the current time zone or based on the current energy prices [5]. A control signal could be sent by:

- the TSO (transmission system operator), in an emergency situation or in case of an power system overload;
- the supplier of energy, in case of high energy prices on the wholesale market.

Disadvantages of this solution are as follows:

- Sending price signals, e.g., to a smart meter or HAN controller, on a continuous basis, is inefficient, because a typical person sleeps 8 h a night, works 8 h a day, spends 2 h on his way to and from work in addition to leaving the house (shopping, meetings, walking) or is focused on performing certain actions: watching TV, reading a book, working on the computer;
- Price, control or shut off signals may not arrive to the destination or may be accidentally or intentionally misrepresented;
- There is room left for abuse, energy supplier may send a signal to shut down loads in a situation where the price of electricity on the wholesale market is high, but when there is no need to relieve the power system. However, if the energy supplier has reserved such a right in the agreement so that it can proceeded, it may seem to be a legitimate action;
- Processing of large amounts of data, supervision of distribution and transmission systems, sending price or control signals in real time, translates into significant additional power consumption by the communication and control systems.

Devices and functionality that can be used to optimize energy consumption:

- a smart energy meter with functionalities: reduction of maximum power in “emergency” state, the ability to remotely shut off the end-customer’s power, the possibility of tariff changes;
- a HAN controller: to control the household electric appliances, depending on the control signals or price signals transmitted by energy companies.

4. Currently Utilized Power System Protection

Currently, in case of emergency, the power system can use different energy rationing. It is necessary to protect power system against overload and break-up:

- When there occurs large faults that manifest themselves with large power deficit, it is necessary to automatically counteract by reducing the power consumption in EPS. An ALS (automatic load shedding) is doing exactly that. Under-frequency relays which load-off certain consumer groups are ALS actuators. ALS automation prevents the frequency avalanche in the system. The protective relays are used for automatic and gradual under-frequency load shedding;
- Deliberately taken preventive measures e.g., load rotation or rolling blackout, which are implemented without the knowledge and consent of the end customers. Rolling blackouts are used even today in developing countries or even in developed countries. For example, they have been used in Japan after the earthquake and tsunami in 2011, due to power deficit in their EPS;
- The introduction of power levels and administrative calling customers from relevant groups to introduce power consumption reduction. The fact that, a reduction had been done can be seen in the measured data. Therefore, this is the administrative action and due to reasons beyond the control of the energy company, customer is not entitled to any bonus for this action and for an obligation to reduce power consumption. Levels of power restriction were introduced, e.g., in Poland in August, 2015;
- The DSR, where is it assumed that, actions are carried out with the consent of the customers and with the approval of their specific activities. The recipients receive some gratification, usually financial. In this case, the DSR uses such solutions, which are not intended to deprive the specific audiences total

electricity supply, only temporarily restricts their power demand, e.g., lowering the threshold of maximum power in smart energy meters, use of very high energy prices CPP, etc. An applicable solution is also a complete customer switch off of energy delivery, but consumers receive appropriate gratification for the use of such DSR programs. There can be mentioned: interruptible/curtailable rates and direct load control, tariffs, reasonable discount for incidental shutdown. The aim is to ensure that, such activities were experienced as minimal as possible by the end customers. In order to relieve the power system, customers have to make a reduction in their power demand.

Activities undertaken to reduce the demand for power are preventive measures. If a power system overload is taking place and the frequency falls, then the ALS automation takes action.

This solution has the advantage that, the decision of the load shedding based on measuring the grid frequency is taken in distributed devices, without sending any control signals. The final result can not be predicted by the central frequency regulator because it can not control such action of home appliances.

This solution is a development of the concept described by the author in two other publications [6, 7], see also Ref. [5, 8].

5. Smart Energy Meter Will Control Home Devices Based on the Measured Grid Frequency

A smart meter will be measuring the frequency of the power grid. The meter will control home devices based on the measured grid frequency (Fig. 1).

In case when the measured value falls below the specified frequency threshold, the smart meter will turn off some home appliances. There is also a possible variant where the smart meter measures the frequency and sends a signal to the HAN controller, which controls home appliances [6].

The new approach to power grid security against overload is by automatic control of the household appliances in the HAN through smart energy meter or HAN controller based on measurements of grid frequency. If the mains frequency falls enough to exceed the under-frequency threshold defined in the smart meter, the meter will send control signals to some devices and disable them or force them to restrict significantly the power consumption. This way the power system would be protected from the effects of overload (Fig. 2).

If the household uses HAN, in the event of sending control signals limiting demand for power and signals based on frequency drop they would have the priority in relation to price signals. First of all, energy demanding devices would be controlled.

After switching off multiple devices, the grid frequency reaches the rated value. In such situation, there is a risk of re-activation of the appliances, if only the frequency again reaches the nominal value. Such action on multiple devices would be very detrimental to the devices themselves, as well as for control of the frequency in the electrical power system. Therefore, there has to be applied a time delay from fixing the frequency at nominal value to reclosing of the devices.

Advantages of this solution are as follows:

(1) for the customer

- One smart meter could control work of many household appliances;
- Control of household appliances by the energy meters would not increase the purchase price of household appliances, in opposite as if the under-frequency sensors would be installed in each home appliance;
- A client itself could make the choice in the HAN network which of the loads would be turned off in case of system overload, in the lack of load reduction, e.g., to the required power level, the meter would automatically completely turn off the power at the end customer location;
- Operation of this type of security is almost

imperceptible to the owner of electrical appliances, while disabling of the entire line at the substation will automatically shut off the power for large groups of consumers;

(2) for the national power dispatch

• Theoretically, it would allow the national power dispatch to lower the spinning reserve. This would reduce the unnecessary power generation. With this solution, fuel would be spared and this would have an impact on the environment by contributing to reduction of greenhouse gases emission;

• Under-frequency threshold of relay would be higher than the threshold in the substation that is why the energy meter would be more sensitive to frequency drops than the substation automation. That is why, at least theoretically, it would prevent a failure of the line, because the first detection and reaction to frequency drop would occur even before action is taken at the station. There will be the under-frequency relays installed;

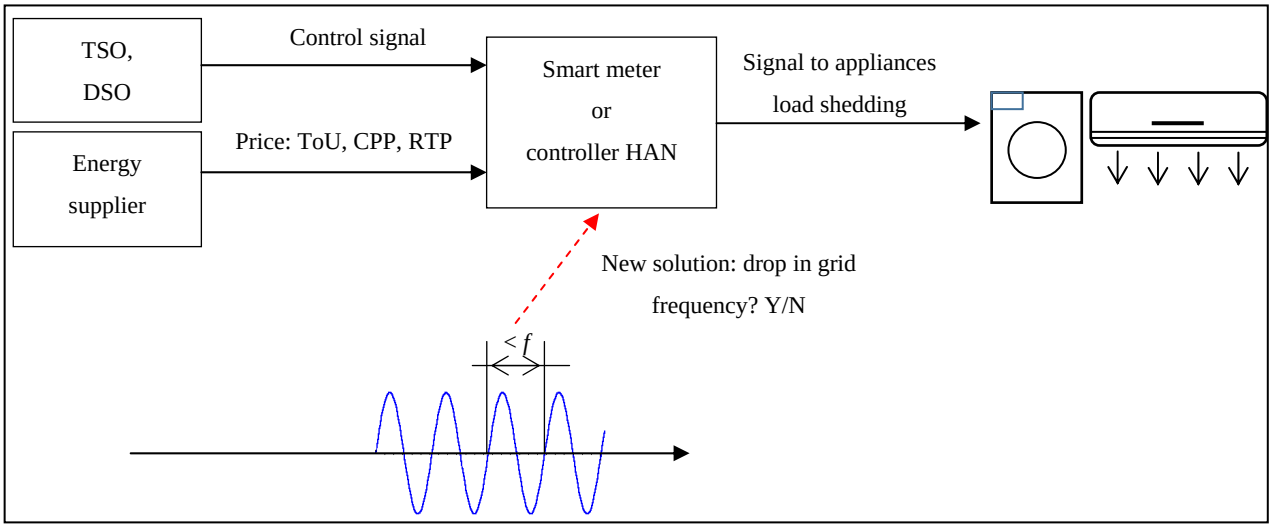

Fig. 1 Smart energy meter controls home devices based on the measured grid frequency.

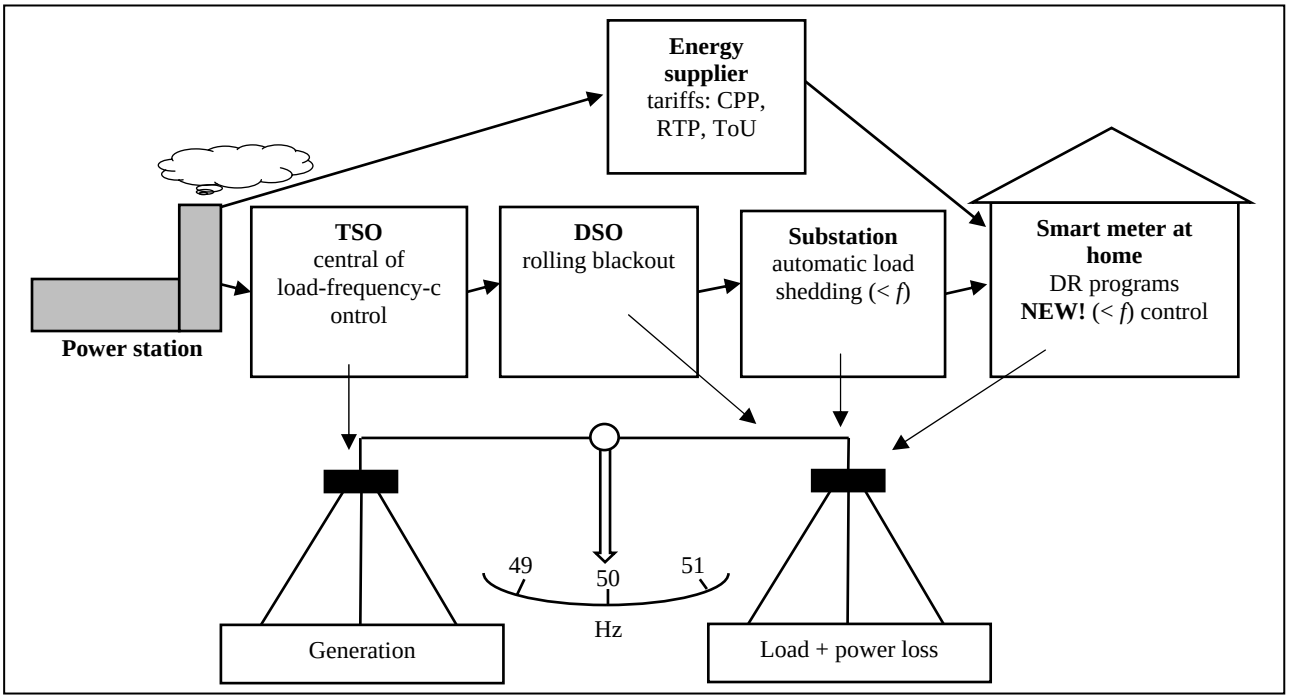

Fig. 2 Tools of utilities of load and frequency control.

• Under-frequency relay activation time is the moment of the overload of the power system, when the expensive time zone takes place in the multi-zone ToU tariffs or critical prices in CPP. Of course, the relationship that if energy prices are high, the frequency drops not always occurs simultaneously. High prices on the wholesale energy market occur when there is a peak load in the power system. In order to cover this demand, there is a need to run expensive, no green power peak generators, which often work irregularly, only a few hours a day, while many costs of their operation are fixed (e.g., the cost of maintenance and staff). They can cover the current demand for energy in the network and then there is no frequency drop, but high energy prices apply on the wholesale market;

• The proposed solution can facilitate the stabilization of labor in the autonomous power supply system or microgrids, which are working in an isolated mode of the grid and they are powered by spinning generators with regulation of frequency;

(3) unnecessary ICT network

• Each smart meter, which controls devices in case of frequency drop, would operate completely independently. This meter does not need a large AMI (advanced metering infrastructure) to know when to control household appliances. It does not need a central system of supervision and control, or receiving or sending signals using communication technologies;

• A smart energy meter, which should detect frequency drop, would be installed by DSO (distribution system operator). In the event of its malfunction, the operator could easily replace it with another one;

• Grid operator could, in specific cases, enable or disable functions of control devices via a smart meter, based on the detected frequency drop;

• The DSO would receive limited amount of data processed and transmitted in AMI. It would also save energy. It allows relieving of the power system in situations of communication problems on the line server-concentrator-smart meter;

• Control of devices, via a smart meter based on proven frequency drop of the power system would allow to relief the system in pre-emergency states, also in case of failure of the wide area network, communication technology used or the surveillance system of the DSO, etc. Thanks to this, the proper functioning of the whole critical infrastructure (power grid) would not be dependent on the proper functioning of other non-critical infrastructure (e.g., telecommunication networks, wide area network);

• Such a solution would be completely protected against interference by cybercriminals—it is easier to modify control signal than the frequency of power grid;

• Response effectiveness of security which is based on consumption data from smart meters in individual households or entire subnet referenced to measure of the frequency would be easily verifiable;

• An energy meter at any time would be able to determine the current power consumption of the household. In this case, it would also have information on whether there is actual ample opportunity to make a reduction in demand for power; in the case of sending control signals, energy meter will also have feedback about whether the actual required reduction in demand occurred.

Disadvantages of the solution are follows:

• In the event of a mass use of smart meters, which would control household appliances based on the detected declines in frequency and mutually uncoordinated work of such meters could result in too big disburden to the system, because the smart meters may shut off too many devices;

• There is a possibility of too much relief to the EPS, in this case, the frequency increase could occur and the appliances start again, causing overloading the power system. Such action would result in frequency fluctuations and would be detrimental to the consumers. Therefore, there is a need for even a slight variation in under-frequency threshold in different

devices. In addition, it is necessary to differentiate the delay in reclosing devices in situations where mains frequency reaches the nominal value;

- Lack of coordination between the different devices performing the load reduction;
- Must utilize well-coordinated operation (tripping thresholds) of such devices with variable frequency control in the EPS. There is a risk of tripping in the event of normal operation of the power system. Currently, if there is a decrease in frequency (activation of the primary control) then the information about this fact is being pushed to the central frequency controller and specific measures are taken to increase the level of generated power (secondary control). In such case, if the device would no longer work, the frequency would slowly reach the nominal value, however, the load would be deprived of electricity power, but in the power system, there would exist some unused power capacities;
- Some customers may not accept such mode of operation of its appliances, assuming they paid for the devices, so the appliances have to work when clients expects and needs them; in this case, it is the issue of adequate customers motivation, willing to commit a possibility of using such functionality;
- Controlled by smart meters based on frequency measurements do not differentiate between customers. Therefore, the order of load reduction at certain customers may be purely coincidental. It also shows the necessity of differentiating thresholds;
- The grid frequency is a global parameter, in the steady state of the EPS, the frequency has the same value anywhere, as a matter of some discussion is the problem of frequency drop in the case of synchronous connection for many national electricity systems, each of which is reinforced by other systems, a noticeable frequency drop occurs only once if the power systems continental level will be significantly overloaded;
- In the case, if there are DC EPS or the AC EPS in which frequency control is carried out in a different way than by the rotating generators e.g., with power electronics, there has to exist detection of an overload of the power system in another way, than on the basis of frequency. Power electronic systems overload does not reduce the grid frequency.

6. Conclusions

The described ability to control devices (utilizing the load shedding) via smart energy meters in the event of the frequency drop of the nominal value allows stabilization of the power grid operation.

The proposed solution changes the current thinking about balancing the EPC and controlling the grid frequency. It seems that, there exists a relatively cheap solution, bringing a lot of benefits. With the introduction of these solutions on a massive scale, it would be necessary to change the methods of adjusting the frequency in the power system.

References

[1] Jabłońska, M. R. 2011. “Actual Trends in Demand Response Researches and Possibilities of Its Implementation under National Circumstances.” *Energy Market ISSN:·1425-5960* 3 (June): 81-6.

[2] Jabłońska, M. R. 2012. “The Analysis of Local Renewable Energy Resources’ Deployment in a Smart Grid Implementation.” *Energy Market ISSN: 1425-5960* 2 (April): 143-7.

[3] Jabłońska, M. R. 2012. “Renewable Energy System Management Processes in Smart Grids Operation.” *Economics and Management* 4 (2): 121-30.

[4] Malko, J. 2014. “Efficiency as a Priority of EU Energy Policy.” *Acta Energetica* 2 (April): 104-8.

[5] U.S. Department of Energy. 2007. “Pacific Northwest GridWise™ Testbed Demonstration Projects, Part II. Grid Friendly™ Appliance Project.” U.S. Department of Energy.

[6] Billewicz, K. 2012. “Smart Metering and Overload Protection.” *Electrical Review* 1b (January): 217-8.

[7] Billewicz, K. 2014. “Proposals for Two New Features for Smart Meters.” *International Journal on Information Technology (IREIT)* 2 (1): 8-15.

[8] Gawlicki, S. M. 2009. “Smart Energy Networks in Practice—Pilot Projects.” *Electrical Power—Present and Development* 1 (January): 23-30.

Call for Papers

Dear author,

This is *Journal of Energy and Power Engineering* (ISSN1934-8975), created in Dec. 2007. We are interested in various kinds of professional papers about energy and power. The *Journal of Energy and Power Engineering*, a monthly professional academic journal, is striving to provide the best platform for researchers and scholars worldwide to exchange their latest findings and results.

Current Columns Involve

Thermal Science; Fluid Mechanics; Energy and Environment; Power System and Automation; Power Electronic; High Voltage and Pulse Power; Sustainable Energy.

Information for Authors

1. The manuscript should be original, and has not been published previously. Please don't submit material that is currently being considered by another journal.
2. Manuscripts may be 3000-8000 words or longer if approved by the editor, including abstract, text, tables, footnotes, appendixes, and references. The title should not be exceeding 15 words, and abstract should not be exceeding 150 words. 3-8 keywords required.
3. The manuscript should be in MS Word format, submitted as an email attachment to our email address.

Editorial Procedures

All papers considered appropriate for this journal are reviewed anonymously by at least two outside reviewers. The review process usually takes 4-5 weeks. Papers are accepted for publication subject to no substantive, stylistic editing. The Editor reserves the right to make any necessary changes in the papers, or request the author to do so, or reject the paper submitted. A copy of the edited paper along with the first proofs will be sent to the author for proofreading. They should be corrected and returned to the Editor within seven days. Once the final version of the paper has been accepted, authors are requested not to make further changes to the text.

Submitting of Manuscripts

All manuscripts submitted will be considered for publication. Please visit our website at www.davidpublisher.com for our automatic paper submission systems or as an email attachment to energy@davidpublishing.org, energy@davidpublishing.com, energy-power@hotmail.com and energy@davidpublishing.net.

Journal of Energy and Power Engineering
David Publishing Company
Tel: 001-323-984-7526, 001-323-410-1082; Fax: 001-323-984-7374

Journal of Energy and Power Engineering
Volume 9, Number 10, October 2015

David Publishing Company
1840 Industrial Drive, Suite 160, Libertyville, IL 60048, USA
Tel: 1-323-984-7526, 323-410-1082; Fax: 1-323-984-7374, 323-908-0457
http://www.davidpublisher.com, www.davidpublisher.org
energy@davidpublishing.com, energy@davidpublishing.org, energy-power@hotmail.com

ISSN 1934-8975